UNIVERSIDADE DE BRASÍLIA
INSTITUTO DE GEOCIÊNCIAS
PROGRAMA DE PÓS-GRADUAÇÃO EM GEOLOGIA

PAULO CASTELLAN MEDEIROS

MECANISMOS DE DEFORMAÇÃO NA ZONA DE CISALHAMENTO PERNAMBUCO LESTE, PROVÍNCIA BORBOREMA, NE BRASIL

BRASÍLIA – DF
2020

UNIVERSIDADE DE BRASÍLIA
INSTITUTO DE GEOCIÊNCIAS
PROGRAMA DE PÓS-GRADUAÇÃO EM GEOLOGIA

**MECANISMOS DE DEFORMAÇÃO NA ZONA DE CISALHAMENTO
PERNAMBUCO LESTE, PROVÍNCIA BORBOREMA, NE BRASIL**

DISSERTAÇÃO DE MESTRADO N: 465

Autor: Paulo Castellan Medeiros
Orientador: Prof. Dr. Luís Gustavo Ferreira Viegas

BRASÍLIA – DF
2020

i

UNIVERSIDADE DE BRASÍLIA
INSTITUTO DE GEOCIÊNCIAS
PROGRAMA DE PÓS-GRADUAÇÃO EM GEOLOGIA

MECANISMOS DE DEFORMAÇÃO NA ZONA DE CISALHAMENTO PERNAMBUCO LESTE, PROVÍNCIA BORBOREMA, NE BRASIL

Autor: Paulo Castellan Medeiros

Banca examinadora:

Prof. Dr. Luís Gustavo Ferreira Viegas (Orientador; IG-UnB)

Profa. Dra. Carolina Gonçalves Cavalcante

Profa. Dra. Catarina Labouré Benfica Toledo

Brasília, 05 de agosto de 2020

AGRADECIMENTOS

Agradeço primeiro a minha mãe, Rita, pelo incentivo a ciência e a educação. Meu pai, Inaldo, por me passar valores tão importante que carrego comigo para toda a vida e a minha namorada, Camila, que mesmo estando a pouco tempo do meu lado já me faz desejar que esse tempo nunca termine.

Agradeço muito Gustavo Viegas, meu orientador, com quem sempre pude contar ao longo de todo o processo de crescimento pessoal e científico. Que SEMPRE esteve disponível para revisar meus textos, mesmo em finais de semana ou feriados.

Meus agradecimentos a Frederico Faleiros, professor da USP que me recebeu durante uma semana em sua sala em São Paulo para a construção das pseudoseções e que, além disso, sempre esteve aberto a ajudar e que em muito ajudou na construção do artigo.

Aos companheiros do TeamViegas e do Laboratório de Geocronologia, Rhander Altoé, Tiago Jalowitski, Eduardo Novais, Raylline Ferreira e Carolina Peixoto que sempre foram grandes aliados na construção da minha pesquisa.

Agradecimentos especiais a João Pedro e Rafaela França da GeoLab pela confecção das lâminas polidas que ficaram prontas em pouco dias. A Charles Henrique e ao NEG-LABISE – UFPE que acelerou a produção das análises de rocha total e que estava disposto a participar do campo, apesar dos contratempos.

Agradeço também a todos aqueles que tornaram minha pesquisa possível com contribuições diárias, como os vários porteiros, faxineiras, técnicos de laboratórios...

MUITO OBRIGADO!!

RESUMO

A Zona de Cisalhamento Pernambuco Leste (ZCPE) consiste em uma estrutura regional nucleada na borda do batólito Caruaru-Arcoverde e em outros granitos sin-cinemáticos neoproterozoicos da Província Borborema (NE do Brasil). A análise estrutural de campo permitiu individualizar a falha em dois domínios principais, os quais registram condições metamórficas e deformacionais distintas. O domínio Caruaru, localizado na porção oeste da ZCPE e associado à borda sul do batólito Caruaru-Arcoverde, é caracterizado por granitos miloníticos com porfiroclastos de feldspato invariavelmente fraturados. O quartzo é encontrado em fitas recristalizadas por rotação de subgrãos e apresenta simetria monoclínica com deslizamento prismático <a>. A química mineral apresenta diferenciação entre porfiroclastos e grãos recristalizados de plagioclásio e K-feldspato. O modelamento termodinâmico do domínio Caruaru restringiu as condições de deformação em 4,75 ± 0,25 kbar e 526 ± 9°C. O domínio Gravatá consiste no segmento oriental da ZCPE e é composto por ultramilonitos bandados que exibem porfiroclastos de feldspato intensamente fraturados e apresentam acomodação de deformação por meio de dissolução e precipitação. O quartzo apresenta raros porfiroclastos alongados e muitos grãos recristalizados por rotação de subgrãos. Os grãos recristalizados são equigranulares, com ativação do sistema de deslizamento basal <a>. O K-feldspato não apresenta contraste de composição entre grãos recristalizados e porfiroclastos, porém os grãos recristalizados de plagioclásio revelam uma tendência de aumento na componente albítica em relação aos porfiroclastos. O modelamento termodinâmico do domínio Gravatá delimita as condições de deformação em 5,9 ± 1 kbar e 437 ± 17°C. As diferenças entre as condições de deformação na Zona de Cisalhamento Pernambuco Leste registram uma evolução tectono-termal distinta, com picos metamórficos em condição de fácies xisto verde alto e baixo simultaneamente. Além disso, a associação entre os mecanismos de rotação de subgrãos e dissolução-precipitação indicam que a deformação foi assistida por fluidos em ambos os domínios. O presente banco de dados sugere que a Zona de cisalhamento Pernambuco Leste é uma estrutura descontínua e de evolução heterogênea, com história deformacional em profundidades associadas à transição rúptil-dúctil e possivelmente em um ambiente intracontinental.

Palavras-chave: zona de cisalhamento Pernambuco Leste, microestruturas, modelamento termodinâmico, mecanismos de deformação

ABSTRACT

The East Pernambuco Shear Zone (EPSZ) consists in a major structure nucleated at the border of the Caruaru-Arcoverde batholith in the Neoproterozoic Borborema Province (NE Brazil). Field structural analysis allowed for the individualization of two domains along the fault. At the western limit and nucleated at the Caruaru-Arcoverde batholith, the Caruaru domain is composed of coarse grained mylonites with invariably fractured feldspar porphyroclasts. Quartzo ribbons are recrystallized by subgrain rotation displaying monoclinic asymmetry with activation of prism <a> slip system. Mineral chemistry of plagioclase and K-feldspar exhibits a contrast between porphyroclasts and recrystallized grains. Thermodynamic modelling in the Caruaru domain constrains the conditions of deformation at 4.75 ± 0.25 kbar and 526 ± 9°C. The Gravatá domain, located in the eastern portion of the EPSZ, is composed of fine-grained banded ultramylonites exhibiting highly fractured feldspar porphyroclasts that also display accommodation of deformation through dissolution-precipitation processes. Quartz is recrystallized mostly by subgrain rotation but also displays rare elongated porphyroclasts. Recrystallized grains are equigranular and exhibit evidence for slip along the basal <a> slip system. K-feldspar grains do not show composition contrasts between recrystallized grains and porphyroclasts, although recrystallized plagioclase grains display an enrichment in albite in relation to porphyroclasts. Thermodynamic modelling in the Gravatá domain constrains conditions of deformation at 5.9 ± 1 kbar and 437 ± 17°C. The differences in deformation conditions along the lateral continuity of the East Pernambuco shear zone reveal an heterogeneous tectono-thermal evolution, with simultaneously high- and low-greenschist facies metamorphic conditions recorded along the structure. Furthermore, the coeval activity of dissolution-precipitation processes and subgrain rotation recrystallization mechanisms indicate that both domains were deformed in the presence of fluids. These evidences suggest that the East Pernambuco shear zone is a discontinuous strike-slip shear zone mainly marked by brittle-ductile strain localization during an heterogeneous exhumation path along the middle- to upper continental crust.

Keywords: East Pernambuco shear zone, microstructures, thermodynamic modelling, deformation mechanisms

SUMÁRIO

LISTA DE FIGURAS

LISTA DE TABELAS

LISTA DE FIGURES DO CAPÍTULO 4

Formatação da Dissertação

Essa dissertação de mestrado é organizada em forma de artigo, contando com o manuscrito submetido para revisão e possuindo formatação própria. O primeiro capítulo, Introdução, consiste na contextualização da pesquisa dentro do contexto da geologia estrutural de zonas de cisalhamento litosféricas e indicando a relevância para a área de estudo. No segundo capítulo é apresentado o contexto regional onde está inserida á área de estudo, levando em consideração alguns novos dados levantados por essa pesquisa. O capítulo três apresenta a fundamentação teórica das técnicas analíticas utilizadas no trabalho. O quarto capítulo consiste na compilação dos principais resultados obtidos nesta pesquisa, os quais foram reunidos em um artigo científico submetido ao periódico *Journal of the Geological Society*. O quinto capítulo contém as conclusões, onde são abordadas de maneira compreensiva as implicações deste estudo para a evolução tectônica da zona de cisalhamento Pernambuco Leste. O sexto capítulo é composto pelas referências bibliográficas e, por fim, o sétimo capítulo contém os anexos com informações complementares sobre dados de campo e análises laboratoriais.

1.   INTRODUÇÃO

Zonas de cisalhamento são estruturas planares que acomodam taxas deformacionais significativamente altas em relação às rochas adjacentes (Alsop e Holdsworth, 2004). Elas ocorrem em toda a interface crustal, apresentando diferentes características de acordo com as condições em que são submetidas. Sua identificação tipicamente envolve relações geométricas, arcabouço cinemático e taxas de deformação no interior da zona.

A investigação da geometria das zonas de cisalhamento tem importância fundamental no estudo dos processos de localização da deformação em contextos geológicos diversos. De maneira geral, rochas deformadas em níveis crustais superiores ou rasos acomodam a deformação a partir de mecanismos rúpteis, comumente na forma de planos de espessura limitada onde a deformação é observada por meio de uma transição abrupta com a rocha encaixante. Com o aumento da pressão e temperatura, é esperado que a espessura da zona de cisalhamento também aumente, e que sua geometria passe de fraturas retilíneas (deformação localizada) para sistemas dúcteis anastomosados (deformação distribuída) (Mitra, 1979).

Na transição rúptil-dúctil, considerada entre 10 e 15 km ao longo do perfil crustal ideal, a resistência mecânica à deformação é máxima (Scholz, 2002). Nesse nível crustal, a acomodação da deformação é heterogênea e cíclica. Sua heterogeneidade é representada pela combinação entre plasticidade intracristalina e fraturamento, enquanto que a ciclicidade se dá por um período de tempo onde as tensões são acumuladas pelas rochas, até que o limite de acúmulo de tensões é rompido, i.e. a resistência elástica do material é ultrapassada resultando em dissipação instantânea de energia na forma de estruturas associadas a eventos sísmicos (Handy et al., 2007). Após o evento sísmico, o processo de acumulação de deformação volta a acontecer por uma combinação das componentes rúpteis e dúcteis, típicas do ambiente de transição.

A combinação entre mecanismos rúpteis e dúcteis comumente é observada através da ocorrência simultânea de fraturamento de fases minerais reologicamente resistentes (e.g. feldspatos, granadas e anfibólios) e recristalização dinâmica de fases minerais menos resistentes (e.g. quartzo, filossilicatos) (Platt, 2015). Esses dois mecanismos combinados resultam na redução do tamanho do grão e geração de uma matriz fina, típica de cataclasitos e milonitos. Estudos experimentais indicam que, se a matriz fina atingir tamanhos de grão menores do que 10 µm, a reologia da rocha sofre uma inversão e a deformação é eficientemente acomodada por meio de fluência difusiva no estado sólido (Karato, 2008; Platt, 2015).

Na Província Borborema, a zona de cisalhamento Pernambuco Leste (ZCPE) possui uma intrínseca relação espacial com granitoides, sendo estes deformados após a sua completa cristalização (Neves et al., 1996). A ZCPE é composta por milonitos e ultramilonitos graníticos onde a relação coeva entre recristalização dinâmica e fraturas sempre é observada mesmo em amostra de mão (Neves e Mariano, 1999). Para além de apresentar características relevantes à transição rúptil-dúctil, a ZCPE é uma estrutura considerada relevante nos modelos geotectônicos da Província Borborema (Brito Neves, 2000; Neves, 2003, 2011), favorecendo trabalhos que tenham como foco sua caracterização detalhada.

Esse trabalho tem como objetivo a caracterização da deformação ao longo da ZCPE. Para tal, foi realizado um trabalho integrado de caracterização da deformação em macro e micro escala, que compreendeu: mapeamento estrutural de campo, análise microestrutural quantitativa e modelamento termodinâmico. Esse processo integrado de técnicas qualitativas e quantitativas permitiu a identificação dos mecanismos de

deformação, das condições de pressão e temperatura e do nível crustal relativo a história deformacional da zona de cisalhamento Pernambuco Leste. Os resultados deste trabalho contribuem para um melhor entendimento do papel da zona de cisalhamento Pernambuco Leste no contexto da evolução neoproterozoica da Província Borborema.

2.   GEOLOGIA REGIONAL

A Província Borborema, Nordeste brasileiro, abrange cerca de 400.000 km² sendo limitada pelas bacias costeiras do Atlântico a leste e a norte, pela Bacia do Parnaíba a oeste e pelo Cráton São Francisco a sul (Almeida, 1981). Esta unidade geotectônica é composta por um embasamento gnáissico-migmatítico paleoproterozoico com alguns núcleos arqueanos, cobertos por sequências metavulcanosedimentares de idade meso- a neoproterozoica, além de ser intrudida por plútons graníticos neoproterozoicos (Brito Neves, 2000).

A orogênese brasiliana, de idade neoproterozoica, está associada com o desenvolvimento de um sistema geometricamente consistente de zonas de cisalhamento que ocorrem por ~ 200.000 km^2 ao longo de toda a província (Vauchez et al., 1995). As zonas de cisalhamento regionais ocorrem como limites de terrenos ou domínios litoestratigráficos/geocronológicos, os quais individualizam assembleias litológicas e idades distintas (Van Schmus et al., 2008; Figura 1).

Entre as principais zonas de cisalhamentos que segmentam a Província Borborema está o Lineamento Pernambuco. Essa falha tem forma sinuosa com ~700 km de extensão e direção principal E-W separando o domínio central do domínio sul (Melo, 1977). Porém, investigações detalhadas do Lineamento Pernambuco permitiram a identificação de dois segmentos distintos. A Zona de Cisalhamento Pernambuco Oeste (ZCPW) foi individualizada por ser caracterizada como uma estrutura com ~14 km de espessura com deformação em alta-T associada à fusão parcial sin-cinemática com a formação de inflexões para NE no seu extremo leste (Vauchez e Egydio-Silva, 1992). Na porção leste do Lineamento Pernambuco, a ZCPE exibe espessura de até 4 km e está intrinsicamente relacionada à deformação de plútons graníticos neoproterozoicos alojados em suas adjacências (Figura 2; Neves e Mariano, 1999).
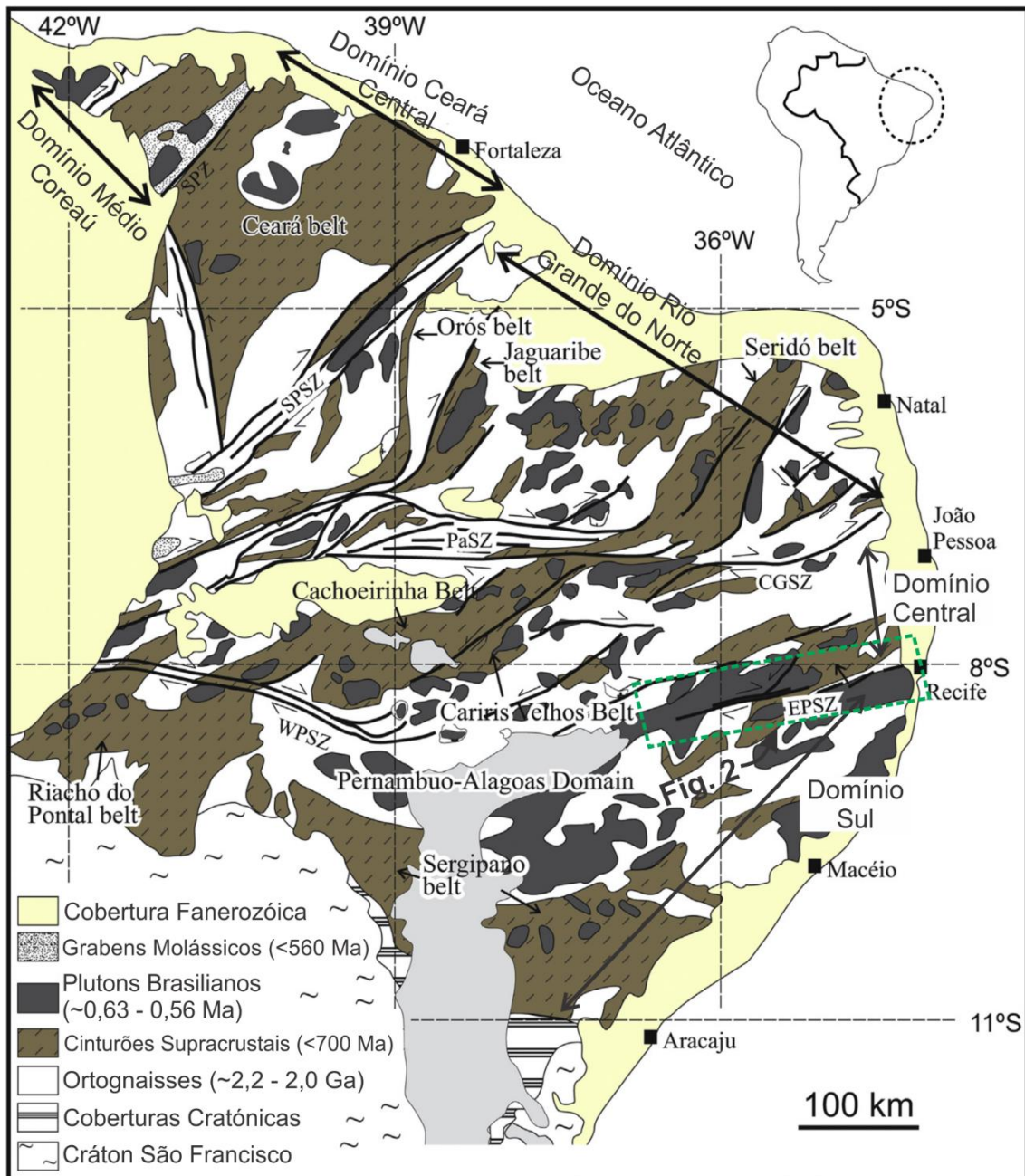
Figura 1. Mapa da Província Borborema com as principais zonas de cisalhamento brasilianas: SPZ – Zona de Cisalhamento Sobral; SPSZ – Zona de Cisalhamento Senador Pompeu; PaSZ – Zona de Cisalhamento Patos; CGSZ – Zona de Cisalhamento Campina Grande; WPSZ – Zona de Cisalhamento Pernambuco Oeste; ZCPE – Zona de Cisalhamento Pernambuco Leste. Modificado de Neves (2015).

A ZCPE é composta por milonitos grossos com porfiroclastos de K-feldspato cercados por uma matriz fina composta principalmente por biotita + epidoto. Nessa trama os milonitos apresentam trama anastomosada formando foliações S-C e porfiroclastos rotacionados indicando cinemática destral. Na porção leste a ZCPE é caracterizada por cinturões ultramiloníticos descontínuos de baixa temperatura, caracterizados por uma segregação de bandas máficas composta por biotita + epidoto e félsicas compostas de

quartzo + K-feldspato + plagioclásio. Protomilonitos, milonitos e ultramilonitos apresentam transições abruptas ao longo desses cinturões (Neves e Mariano, 1999).

A ZCPE está nucleada principalmente em batólitos graníticos neoproterozoicos entre eles, o Batólito Caruaru-Arcoverde, datado em 591-583 Ma (Guimarães et al., 2004) e na suíte intrusiva Itaporanga, datado por U-Pb em 584 ± 2 Ma (Brito Neves et al., 2003). O início da deformação da ZCPE foi datado pelo grão mais jovem de monazita em 591 ± 4 Ma no ortognaisse Bezerros (França et al., 2019).
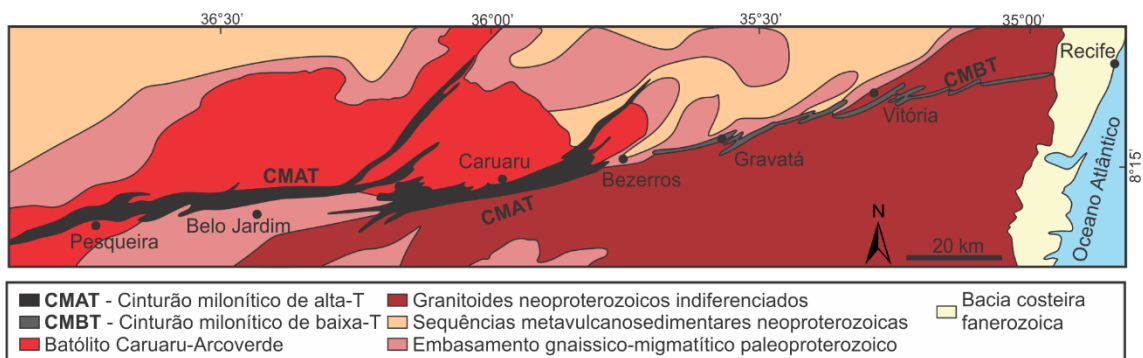
Figura 2. Mapa geológico esquemático dos cinturões de alta-T e baixa-T que compõem a Zona de Cisalhamento Pernambuco Leste (ZCPE).

3. MATERIAIS E MÉTODOS

O desenvolvimento dessa pesquisa foi realizado por meio de uma abordagem integrada de métodos qualitativos e quantitativos em geologia estrutural. Os métodos e atividades realizados podem ser divididos em dois grupos principais: (i) Trabalho de campo, com foco em descrição das estruturas deformacionais de granitos miloníticos aflorantes ao longo da ZCPE; e (ii) técnicas analíticas, compreendendo (a) microscopia ótica e eletrônica; (b) espectroscopia de energia dispersiva (*Energy Dispersive Spectroscopy*, EDS), para determinação da composição modal da rocha e composição química semi-quantitativa dos minerais; (c) uso da técnica de difração de elétrons retro-espalhados (*electron backscattered diffraction*, EBSD), para determinação da orientação preferencial cristalográfica (OPC); (d) análise da química de rocha total por fluorescência de raios-X (FRX); e (e) análise da química mineral com microssonda eletrônica por meio da Espectroscopia dispersiva de comprimento de onda (*Wavelength Dispersive Spectroscopy*, WDS).

3.1. Trabalho de campo

O trabalho de campo foi realizado ao longo de toda a extensão da Zona de Cisalhamento Pernambuco Leste (Figura 2), com o objetivo de cartografar e identificar as principais estruturas, relações geométricas e critérios cinemáticos presentes ao longo da falha. Em todos os afloramentos, amostras representativas da deformação local foram coletadas e orientadas em relação à sua foliação e lineação.

Durante o trabalho de campo, feições estruturais dos afloramentos são investigadas, tais como: (i) intensidade da deformação, considerando a classificação da rocha em protomilonito, milonito e ultramilonito; (ii) textura dos minerais, com identificação e caracterização mesoscópica dos clastos (objetos rígidos) e da matriz fina; e (iii) gradiente metamórfico, com o intuito de estabelecer uma relação entre o grau metamórfico e intensidade deformacional das rochas.

3.2. Técnicas Analíticas

3.2.1 Descrição petrográfica e microestrutural

Um total de 56 amostras selecionadas foram cortadas paralelas ao plano XZ para confecção das lâminas polidas destinadas a estudos petrográficos. A descrição petrográfica e o registro fotográfico ocorreram no Laboratório de Raio-X do Instituto de Geociências – UnB e por meio de um MEV modelo FEI QUANTA 450, disponível no Laboratório de Geocronologia do Instituto de Geociências – UnB.

A investigação microestrutural foi concentrada na caracterização da geometria entre as fases minerais, distribuição e tamanho dos grãos, morfologia e frequência de ocorrência de estruturas rúpteis, evidências de recristalização e características diagnósticas de processos de mistura de fases. Este estudo permitiu identificar e definir domínios microestruturais que foram adotados com o objetivo de simplificar a organização das informações estruturais.

3.2.2 Determinação da Orientação Preferencial Cristalográfica (OPC)

O feixe de elétrons produzido pelo MEV pode ser utilizado para obtenção das OPCs, por meio da técnica de difração de elétrons retroespalhados (*Electron Backscatter*

Diffraction, EBSD). Ao incidir o feixe na amostra, os elétrons são espalhados em diversas direções; aqueles que difratarem obedecendo a lei de Bragg (1) descrevem uma trajetória cônica, definida pelos cones de Kossel, e são interceptados em uma tela de fósforo formando faixas ou linhas denominadas bandas de Kikuchi (Prior et al., 1999; Figura 3). A lei de Bragg pode ser definida como:

$$2d_{hkl} \, \mathrm{sen}\theta = n \, \lambda \quad (1)$$

Onde:

d_{hkl} = distância reticular (hkl),

θ = ângulo de Bragg,

n = ordem de reflexão,

λ = comprimento de onda relacionado a tensão de aceleração dos elétrons.

As bandas de Kikuchi possuem padrão paralelo e são caracterizadas por linhas que possuem um espaçamento distal de 2θ. Este ângulo distal é correlacionado aos ângulos entre os planos reticulares e a interseção entre as bandas caracteriza uma direção cristalográfica. Dessa forma, a orientação da interseção entre diversos conjuntos de bandas de Kikuchi pode ser usada para determinar a orientação preferencial cristalográfica dos minerais (Morales et al., 2007).
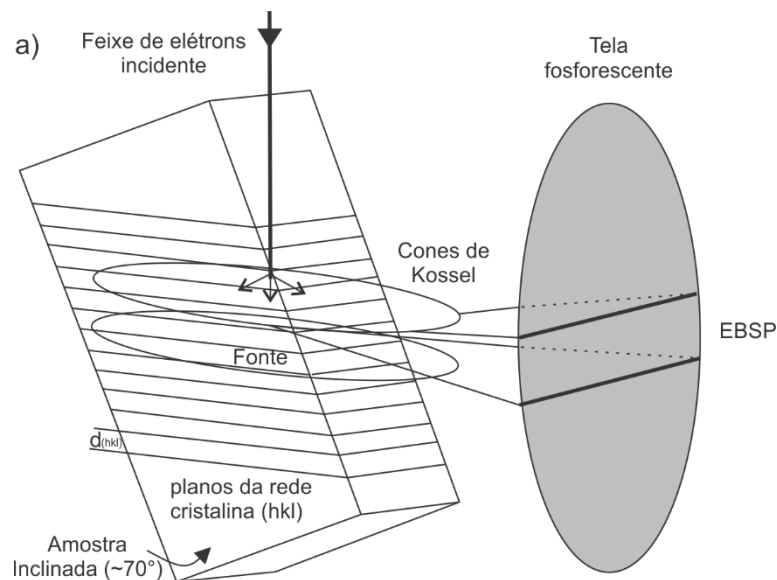
Figura 3. Esquema da trajetória entre o feixe de elétrons e a tela fosforescente. Modificado de Morales (2007).

As OPCs que são identificadas durante o método de EBSD são normalmente exibidas na forma de figuras de polo que são uma forma de representação em duas dimensões dos eixos tridimensionais dos minerais (Randle e Caul, 1996). Figuras de polo são plotadas em estereogramas orientados de acordo com foliação e a lineação da rocha onde são apresentando os polos dos planos da rede cristalográfica de um determinado mineral. Com as OPCs dos minerais é possível extrair informações em relação às condições de deformação, como: deformação coaxial ou não-coaxial, mecanismos de deformação e estimativa de temperatura de deformação. Essas informações são de grande auxílio na investigação das condições de deformação, porém devem ser analisadas em conjunto com outras análises porque, a depender das condições, os resultados podem apresentar ambiguidades (Wenk e Christie, 1991).

Nas análises realizadas nesse trabalho a amostra foi posicionada em um ângulo de ~70° em relação ao feixe do MEV. Além disso, o MEV operou com tensão de aceleração igual a 20 keV, a intensidade de corrente de 15 µA e uma distância de trabalho de ~20 mm.

3.2.3 Fluorescência de raios-X

A fluorescência de raios-X (FRX) é uma técnica que permite identificar e quantificar os elementos através da medição do comprimento de onda de uma emissão de raios-X. O teor de um dado elemento é relacionado à intensidade da emissão do comprimento de onda emitido por ele (Beckhoff et al., 2006).

Em modelos de FRX que geram resultados quantitativos, os mesmos utilizam espetroscopia de comprimento de onda dispersivo (WDS). Nesse método, uma fonte de raios-X é emitida sobre a amostra que reage gerando raios-X secundários em todas as direções (Figura 4). Aqueles que obedecerem à lei de Bragg (1) são alinhados por um colimador e direcionados ao cristal analisador. Os cristais analisadores apenas refletem para os detectores o comprimento de onda específico do elemento a ser analisado. O detector compara esse comprimento de onda e a sua intensidade a um padrão para determinar o elemento e seu teor (Jenkins, 1999).

Para que seja otimizada a velocidade e qualidade da análise de FRX, equipamentos modernos realizam uma rotação θ no cristal analisador enquanto o detector rotaciona em uma velocidade 2θ. Essa rotação é realizada para que todos os planos cristalográficos

tenham a possibilidade de satisfazer a lei de Bragg, e a análise possua melhores resultados.
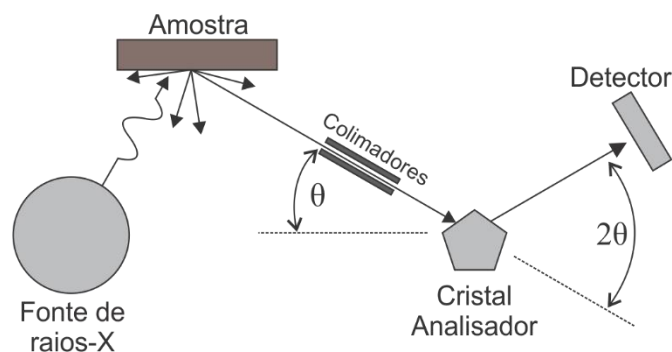
Figura 4. Ilustração esquemática do processo de análise da fluorescência de raios-X. Modificado de Beckhoff et al. (2006).

O procedimento de análises químicas de rocha total por meio de fluorescência de Raios-X foi realizado no NEG-LABISE – UFPE. As amostras selecionadas para análise foram pulverizadas e enviadas ao laboratório que seguiu os procedimentos descritos em Buhrke et al. (1997), para obtenção dos resultados:

1. Uma porção de cada amostra foi colocada em estufa para secar a 110°C por 12 horas e então levada a uma mufla, a 1000°C, por 2 horas, para determinação de perda ao fogo.
2. Pérolas fundidas foram confeccionadas usando tetraborato de lítio como fundente na proporção 1/5 (Amotra/TBL).
3. As pérolas foram analisadas em espectrômetro de fluorescência de raios X Rigaku modelo ZSX Primus II, equipado com tudo de Rh e sete cristais analisadores, pelo método de curvas de calibração que foram construídas com materiais de referências internacionais.

3.2.4   Microssonda eletrônica

A análise por microssonda eletrônica assim como a FRX, permite a quantificação da composição química, porém a microssonda eletrônica possui feixe com menor diâmetro e maior capacidade de geração de sinal, permitindo análise individual de minerais. A microssonda eletrônica possui um feixe de elétrons que é colimado por uma sequência de lentes condensadoras para que sua incidência na amostra tenha diâmetro controlado,

variando entre 1 e 1000 µm. Com a interação feixe-amostra são gerados raios-X secundários que, ao atingirem os cristais analisadores, são refletidos para o detector apenas os raios-X que possuem comprimento de onda igual ao do elemento a ser analisado (Figura 5). A partir do comprimento de onda e da intensidade da onda são determinados os elementos e seus teores (Goldstein et al., 2003).
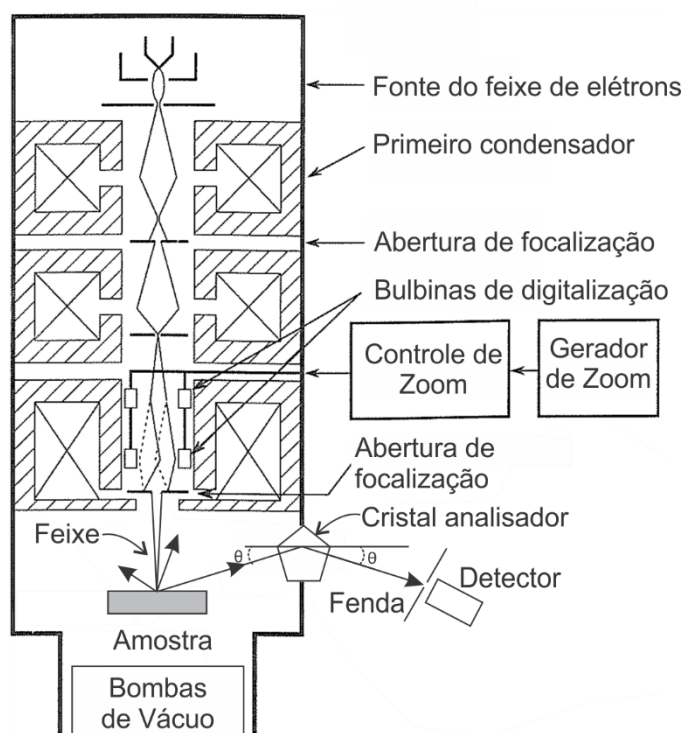
Figura 5. Ilustração esquemática de uma microssonda eletrônica, modificado de Goldstein et al. (2003).

Nessa pesquisa as análises de microssonda eletrônica foram realizadas no Laboratório de Microssonda Eletrônica do IG – UnB com um equipamento do modelo JEOL JXA-8230. Durante as análises o equipamento funcionou com uma voltagem entre 15 e 20 kV, corrente de 5nA e feixe com diâmetro de 1 µm e 5 µm. Foi determinada a composição química dos elementos maiores em forma de óxido que compõem os feldspatos deformados em diferentes domínios estruturais ao longo da ZCPE.

3.3. Modelamento Termodinâmico

Com o modelamento termodinâmico é possível estabelecer todas as assembleias minerais possíveis em um dado intervalo de pressão e temperatura para uma dada composição química de rocha total. Com o objetivo de se determinar as condições

metamórficas durante a deformação, são selecionadas rochas representativas da deformação e são confeccionadas pseudoseções (Holland e Powell, 1998).

A realização do modelamento termodinâmico ocorreu por meio do programa Perple_X 6.7.5 (Conolly, 2005). As pseudoseções foram construídas no sistema NCKMASHTO e utilizaram um banco de dados atualizado por Holland e Powell (2011), e consideraram um sistema saturado em água abaixo da linha do solidus (White et al., 2001). Foi utilizado o modelo de solução de White et al. (2014) para: clorita, biotita, granada, mica branca, estaurolita e para a fusão parcial. Para feldspato foi utilizado o modelo de Fuhrman e Lindsley (1988), para ilmenita o modelo de White et al. (2000), para epidoto, Holland e Powell (2011), e Green et al. (2016) foi utilizado como referência para anfibólio. O aprimoramento por meio de isopletas ocorreu com a determinação da composição modal por meio da técnica de contagem de pontos e composições químicas determinadas pela microssonda eletrônica.

4. **Brittle-ductile fabrics and P-T conditions of deformation in the East Pernambuco shear zone (Borborema Province, NE Brazil)**

Paulo Castellan[1*], Gustavo Viegas[1] & Frederico M. Faleiros[2]

[1]Instituto de Geociências, Universidade de Brasília, Brasília, Brazil
[2]Instituto de Geociências, Universidade de São Paulo, São Paulo, Brazil
*Corresponding author (e-mail: paulo.castellan@gmail.com)

P.C. https://orcid.org/0000-0003-0657-6716

G.V. https://orcid.org/0000-0002-9945-6256

F.M.F. https://orcid.org/0000-0003-2199-8116

Abstract: Fabrics of the East Pernambuco shear zone (EPSZ) were studied via microstructural analysis, mineral chemistry and isochemical phase diagram modelling in order to constrain pressure and temperature conditions of deformation during shearing. Granitic mylonites show fractured feldspar porphyroclasts embedded in a fine-grained, recrystallized quartzo-feldspathic matrix. These mylonites grade laterally into banded ultramylonites characterized by stretched feldspar clasts alternated with recrystallized quartz bands. Fractures in these ultramylonites are filled by phyllosilicates. Mineral chemistry of feldspars points to systematic changes between porphyroclasts, grains within fractures and fine-grained mixtures. Quartz crystallographic fabrics in mylonites suggest activation of prism<a> slip, while the ultramylonites show the activation of both rhomb and basal slip systems. Thermodynamic modelling suggests that mylonites were formed at 4.75 ± 0.25 kbar and $526 \pm 9°C$, while ultramylonites yield conditions of 5.9 ± 1 kbar and $437 \pm 17°C$. These observations suggest that the EPSZ records an heterogenous path of strain accommodation, marked by decreasing temperature from its western sector to its eastern termination. The differences in metamorphic conditions are consistent with a transitional, brittle-ductile strain regime. Such characteristics indicate that the EPSZ is a Neoproterozoic shear belt nucleated and heterogeneously exhumed at the brittle-ductile transition, possibly in an intracontinental setting. (end of abstract)

Supplementary Material: EPMA analysis of feldspars in Caruaru and Gravatá domains, T-X(O$_2$) pseudosections, available at the end of this dissertation.

4.1.   Introduction

The rheology of the continental crust at intermediate depths is marked by the co-existence of both brittle- and ductile deformation mechanisms that occur along a transitional zone under diverse pressure and temperature conditions. Such patterns define a zone of maximum lithospheric strength that is able to accumulate significant strain rates, potentially associated with seismic slip (Sibson 1977). The combination between high differential stresses and thermally-activated solid-state flow results in heterogenous patterns of strain accommodation, which can be continuously or intermittently preserved during the geological record (Bürgmann & Dresen 2008).

Shear zones developed in the brittle-ductile transition are typically marked by a cyclic geological evolution since nucleation until exhumation in mid- to upper crustal levels (Fagereng & Toy 2011). As a consequence, strain localization in these structures is a direct result of the interplay between frictional- and viscous deformation mechanisms that operate at mid-crustal conditions. The study of brittle-ductile shear zones, therefore, aids in unraveling the mechanical behavior of the crust and the pressure and temperature conditions that dominate in the region of maximum strength of the lithosphere (Handy *et al.* 2007).

The Borborema Province is located between the Amazonian, São Francisco, West African and Central Congo cratons in the pre-drift reconstruction between South America and Africa continents (Fig.1a; Neves 2011). This structural setting, consisting of numerous crustal-scale shear zones, was stable after the Brasiliano orogeny (Fig. 1b) and occurs in close association with the emplacement of Neoproterozoic granitoid plutons (Vauchez *et al.* 1995; Weinberg *et al.* 2004). These structures form a shear zone system that extends for more than 200,000 km^2 in Northeast Brazil. Major E-W, dextral strike-slip faults such as the Patos and Pernambuco shear zones are attributed to the late stages of the Neoproterozoic Brasiliano-Pan-African orogeny that affected the South American continent (Van Schmus *et al.* 2008).

The Pernambuco Shear Zone, once thought to represent a major crustal structure that would extend for ca. 700 km^2 in lateral continuity into West Africa (Davison et al. 1995), was subsequently defined as a discontinuous system of shear zones segmented into a western and an eastern branch (Vauchez & Egydio-Silva, 1992). The West Pernambuco Shear Zone (WPSZ) is composed of an anastomosed system of dextral shear zones

deformed at high-temperature conditions while intrinsically related to migmatites. Its eastward termination bifurcates in a horsetail-like structure. The East Pernambuco Shear Zone (EPSZ) is composed by high- to low-T mylonitic granitoids (Neves & Mariano 1999). Both domains are separated by the Tucano-Jatobá basin (Fig. 1c).

Although the tectonic history of the WPSZ has been appraised in detail via field and quantitative microstructural studies (e.g. Vauchez & Egydio-Silva 1992), the structural history and the significance of the EPSZ to the overall evolution of the Borborema Province is still open to debate. Two main hypotheses are envisaged for the development of the EPSZ: i) a post-collisional, Neoproterozoic strike-slip fault nucleated after the amalgamation of Archean/Paleoproterozoic allochthonous terranes (e.g. Brito Neves *et al.* 2000); and ii) an intracontinental, large-scale shear zone developed in a pre-existing crustal anisotropy (Neves 2003, 2011). Recent petrological, geochemical and geochronological investigations have constrained the age of the EPSZ in ~ 590 Ma and argued for an intracontinental origin (França *et al.* 2019).

In this contribution we present a petrostructural investigation based on quantitative microstructural analysis and thermodynamic modelling from the mylonites that occur along the ENE-WSW trending segment of the EPSZ. Through a combination of field structural analysis, microstructural observations, mineral chemistry and thermodynamic modelling, we investigate the deformation mechanisms, P, T conditions of deformation and the brittle-ductile strain regime active during the history of deformation of the EPSZ. Our study has implications for the tectonic evolution of mid-crustal shear zones and the role of the EPSZ as a major-scale structure in the geotectonic frame of the Borborema Province.

4.2. Geological Setting

The two segments that compose the Pernambuco Shear Zone (Fig. 1c), separated by the Tucano-Jatobá Basin, have been widely characterized in terms of petrology, geochemistry and geochronology (Vauchez & Egydio-Silva 1992; Neves & Vauchez 1995; Neves & Mariano 1999; Neves *et al.* 2000; França *et al.* 2019).
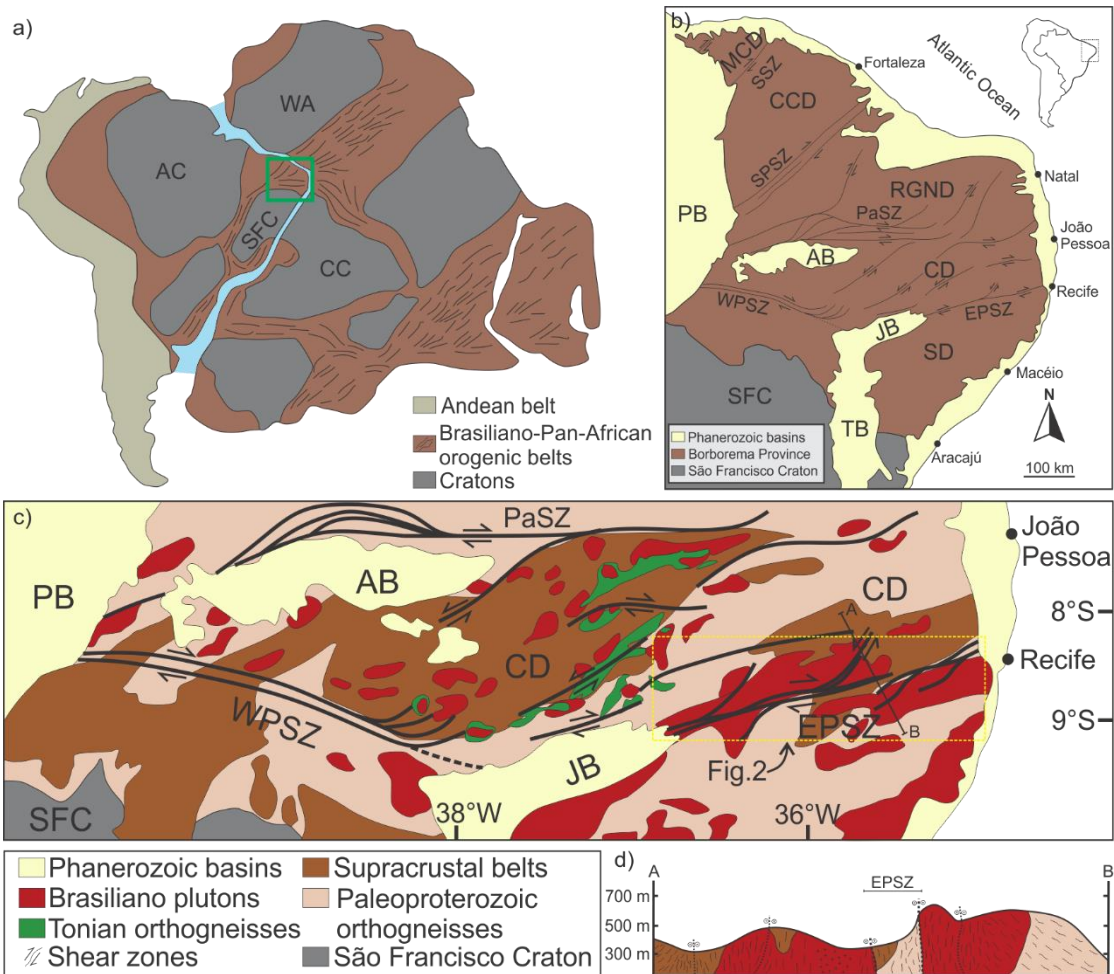
Fig. 1. (**a**) Pre-drift reconstruction of South America-Africa showing Amazonian, São Francisco, West African and Central Congo cratons, Neoproterozoic belts and the Andean belt. Borborema Province is highlighted in the green square. (**b**) Sketch displaying divisions of Borborema Province into MCD, Médio Coreaú Domain; CCD, Ceará Central Domain; RGND, Rio Grande do Norte Domain; CD, Central Domain; and SD, Southern Domain, and their respective shear zone limits: SSZ, Sobral Shear Zone; SPSZ, Senador Pompeu Shear Zone; PaSZ, Patos Shear Zone; and WPSZ, West and East Pernambuco Shear Zone; and EPSZ, East Pernambuco Shear Zone. Major Phanerozoic basins: PB, Parnaíba Basin; AB, Araripe Basin; JB, Jatobá Basin; and TB, Tucano Basin. (**c**) Simplified geological map of the Central domain with the East Pernambuco shear zone shown in the inset (modified from Neves *et al.* 2015, p. 239, fig. 1). (d) Schematic cross-section displaying the structure of the EPSZ and subsidiary shear zones.

The dextral WPSZ is mainly composed of high-grade gneisses and migmatites that extend eastward beneath Paleozoic sedimentary deposits of the Parnaíba Basin until terminating in dextral splays that bifurcate from the main shear zone (Vauchez & Egydio-Silva 1992, Fig. 1c). The EPSZ, located in the eastern termination of the Jatobá basin, has ~ 2km width and extends eastwards from ~ 250 km until the coastal line (Fig. 2a). It is associated with greenschist facies mylonites that affect mainly the Caruaru-Arcoverde batholith (França *et al.* 2019) and Brasiliano plutons that compose the Pernambuco-

28

Alagoas domain (Silva Filho *et al.* 2002). The Caruaru-Arcoverde batholith was dated at 591-583 Ma (Guimarães *et al.* 2004; Neves *et al.* 2004), while Neoproteroic plutons such as the Bezerros orthogneiss yielded monazite ages of 591±4 (França *et al.* 2019).

Fabrics in the EPSZ are mainly marked by an E-W trending, sub-vertical mylonitic foliation that presents several dextral kinematic indicators, such as parasitic folds, rotated clasts and imbricated fractures. A shallow-dip to sub-horizontal stretching lineation can be observed along the trend of the shear zone (Fig. 2a,b). The timing of nucleation of the structure is constrained via a monazite grain age of 591±4, while zircon U-Pb ages of 575 ± 17 Ma are interpreted as the age of main activity in the EPSZ (França *et al.* 2019).

4.3.   Methods

There is a marked variation in mesoscale structures and metamorphic conditions across the length of the shear zone, which tend to gradually decrease in metamorphic grade towards its eastern termination (e.g. Neves & Mariano 1999). We have conducted structural mapping throughout the length of the shear zone and collected representative samples individualized in two structural domains, according to mesoscale fabric patterns and metamorphic grade (Fig. 2a): a) the Caruaru domain, located west of the town of Caruaru and comprising the western sector of the EPSZ, and 2) the Gravatá domain, east of the town of Caruaru and extending eastwards until the coastal line.

4.3.1   Microstructures and Electron Backscatter Diffraction (EBSD) analysis

Deformation microstructures and petrographical identification of the mylonitized granitoids were studied via polarized light and electron microscopy. Oriented thin-sections were cut in the XZ section of the finite strain ellipsoid (i.e. perpendicular to the foliation, parallel to the lineation), as this is the section with the highest degree of asymmetry of deformation in the EPSZ. The distribution, phase relationships and modal proportions of both individual phases and recrystallized aggregates were investigated on grain boundary maps generated through Scanning Electron Microscopy (SEM) images.

Crystallographic preferred orientations (CPOs) of recrystallized quartz grains were investigated via EBSD mapping of representative areas in the mylonitic

microstructure. EBSD analysis was performed at the Electron Microscopy Centre, Plymouth University (UK). Mapping of deformation microstructures and recrystallized domains was acquired in rectangular grids with step sizes ranging from 0.5 to 3 µm. Samples were mechanically polished and further subjected to polishing with colloidal silica in order to ensure a damage-free surface. The polished thin-sections were carbon coated and analyzed in high-vacuum environment. Working conditions were of 20 kV accelerating voltage, 20-23 mm working distance and 70° sample tilt.

EBSD results were treated with the MTEX toolbox for MATLAB (Hielscher & Schaeben 2008) to generate pole figures, phase- and crystallographic maps and misorientation angle distributions.

4.3.2 XRF analysis of bulk-rock chemical composition

Whole rock chemical analysis of major elements was acquired via X-ray Fluorescence (XRF) analysis with a Rigaku model ZSX Primus II equipped with a rhodium tube at the Departamento de Geologia, Universidade Federal de Pernambuco. Powder samples were first submitted to 110°C for 12 h to dry and 1000°C for 2 h to define loss on ignition (LOI). Afterwards samples were diluted at 1:5 in $Li_4B_4O_7$ to be analyzed at the XRF.

4.3.3 EDS chemical element analysis

Maps of modal composition and mineral chemistry were acquired via Energy Dispersive Spectroscopy (EDS) at specific areas of ~0.5 mm^2 containing the representative mineral assemblage of deformation in both domains. The analysis was made in a Scanning Electron Microscopy (SEM) equipped with a EDX Ametek Apolo X EDS detector operating with an accelerating voltage of 15-20 kV and beam current of 90 µA at the Instituto de Geociências, Universidade de Brasília.

4.3.4 Mineral chemistry

Major element chemical compositions of feldspars (porphyroclasts and recrystallized grains) were measured using a Jeol JXA-8230 Electron Probe Micro-Analyzer (EPMA) at the Instituto de Geociências, Universidade de Brasília. The analysis

was obtained with accelerating voltage of 15-20 kV, current of 5 nA and beam diameter of 1 µm for K-feldspar and 5 µm for plagioclase.

4.3.5 Thermodynamic modelling

Two representative samples of mylonites from the EPSZ were selected for thermodynamic modelling of deformation conditions. H2O-saturated, P-T isochemical phase diagram sections were calculated using Perplex 6.7.5 (Connolly 2005). The H_2O contents were estimated to saturate the rocks below solidus with the minimal amount necessary to reproduce the conditions of deformation estimated by other methods (White *et al.* 2001). The T-X(O_2) pseudosection – available in the supplementary material - was used to define the O_2 contents for the bulk rock composition that reproduce the Fe^{3+}-bearing phases (e.g. epidote, hematite). Pseudosections were constructed considering the system SiO_2-TiO_2-Al_2O_3-FeO-MgO-CaO-Na_2O-K_2O-O_2-H_2O and an internally consistent thermodynamic dataset (Holland & Powell 2011). We used solution models of White *et al.* (2014) for chlorite, biotite, garnet, melt, white mica and staurolite, Fuhrman & Lindsley (1988) for feldspar, White *et al.* (2000) for ilmenite, Holland & Powell (2011) for epidote, Green *et al.* (2016) for amphibole and White et al. (2002) for spinel.

4.4. Results

4.4.1 Field observations

The studied mylonitic granitoids that compose the EPSZ record an heterogenous path of strain localization, being mainly characterized by coarse-grained, quartzo-feldspathic monzogranites with local *augen* structures in the Caruaru domain, while the Gravatá domain is marked by fine-grained, banded ultramylonites that show quartz ribbons alternating with fine-grained, polyphase mixtures. In both domains, quartzo-feldspathic shear bands are ubiquitous and indicate strong, brittle-ductile deformation partitioning during mylonitization.
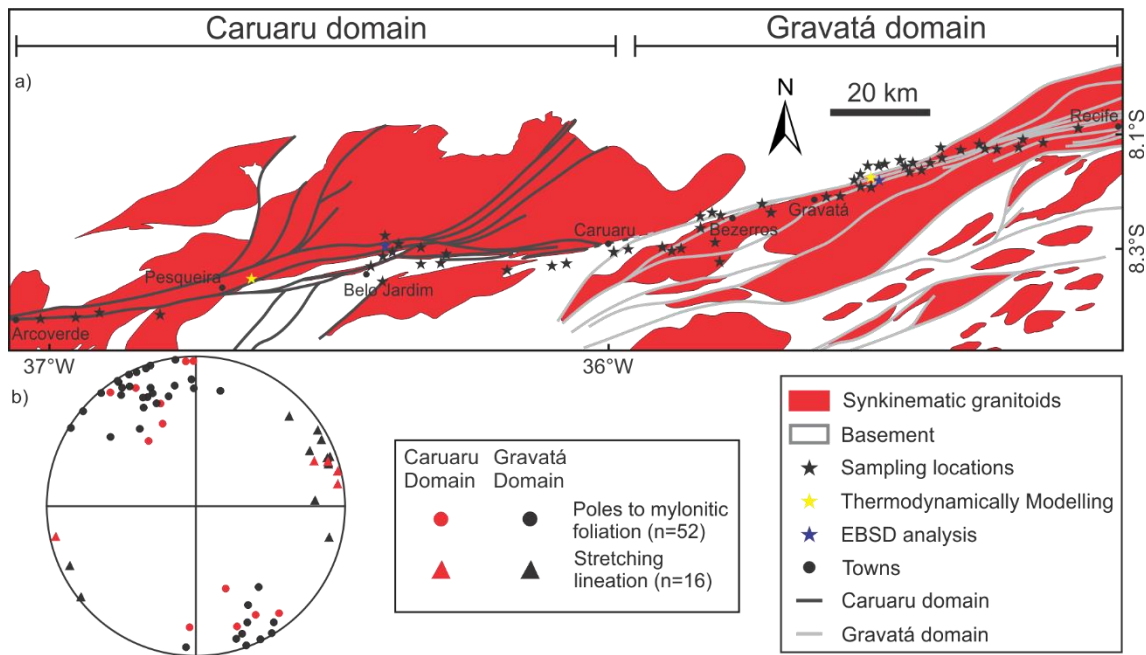
Fig. 2. Schematic structural map of the East Pernambuco Shear Zone. (**a**) Main trend of the shear zone, in-between Neoproterozoic granitoid plutons, and sample locations. (**b**) Mesoscale structural fabrics (foliation and lineation) from the EPSZ.

4.4.1.1.   Caruaru domain

This domain is located at the contact with the southern edge of the Caruaru-Arcoverde batholith and consists in the western termination of the EPSZ (Fig. 2a). The thickness along the entire domain is relatively constant at ca. 2 km, reaching a maximum of 4 km near NE splays that branch off from the main shear zone (Fig. 2a). The rocks are mylonitic granitoids composed of quartz, K-feldspar and plagioclase, with biotite and amphibole as major mafic components. The mesoscopic structure is defined by an anastomosed fabric in which elongated quartz ribbons with $\pm$ 2 cm and an aggregate of mafic minerals wrap around feldspar porphyroclasts up to 5 cm in diameter (Fig. 3a). Centimeter- to meter-scale fractures and antithetic sinistral faults – locally associated with NE splays that branch out from the EPSZ - systematically reduce the grain-size of the mylonitic fabric (Fig. 3b). A dextral shear sense is observed in S-C fabrics and σ-porphyroclasts (Fig. 3a-c).

4.4.1.2.   Gravatá domain

This domain is characterized by mylonites and ultramylonites in discrete contact with less-deformed granites that display a mylonitic foliation obliquely oriented at ~ 35°

32

counterclockwise relative to the main trend of the EPSZ, such asymmetry (Fig. 3d) indicating a dextral shear sense. The main rock types are banded ultramylonites with a sub-vertical foliation (Fig. 3e). Ultramylonites have feldspathic (~ 1 cm) and quartz rich (~ 0.2 cm) layers, which are associated with discontinuous mafic layers (~ 0.3 cm; Fig. 3e) or a fine-grained ultramylonite surrounding fragmented porphyroclasts (Fig. 3f).
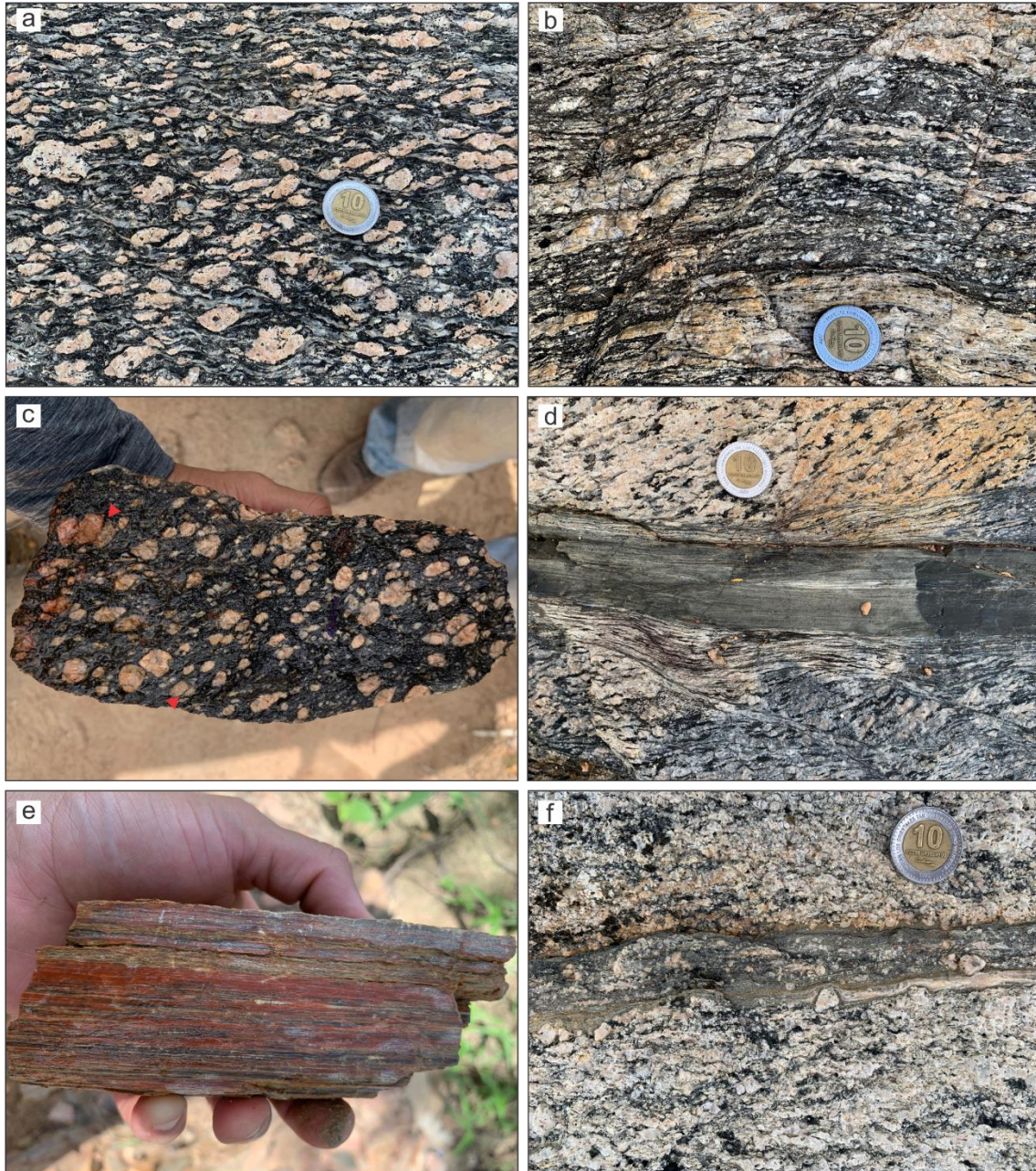
Fig. 3. Field aspects of Caruaru (a, b and c) and Gravatá (d, e and f) domains. (**a**) Anastomosed mylonitic foliation defined by σ-type K-feldspar porphyroclasts surrounded by cm- to mm-scale quartz ribbons and biotite layers. (**b**) Anastomosed mylonitic fabric crosscut by sinistral antithethic fault. Notice the reduction of grain-size within the fracture's damage zone. (**c**) Hand-sample of mylonite with fractured, subspherical and sigmoidal K-feldspar porphyroclasts. Dilatant fracutres marked with a red arrow. (**d**)

Fine-grained ultramylonite band with discrete contact with coarse-grained granite. (**e**) Ultramylonite with homogeneous feldspathic bands, discontinuous mafic layers and quartz-rich bands. (**f**) Fine-grained ultramylonite zone with fragmented and subhedral feldspar clasts.

4.4.2   Microstructures of the Caruaru domain

Porphyroclastic mylonites observed in this domain are composed of K-feldspar (36%), plagioclase (21%), quartz (20%), biotite (19%) and epidote, with accessory ilmenite, titanite, apatite, amphibole, and zircon (Fig. 4a). Although amphibole is present, this mineral is not stable during metamorphism as evidenced in the reaction of amphibole to biotite (Fig. 4b). Thus, the stable mineral assemblage during deformation is represented by:

$$Qz + Kfs + Pl + Bt + Ilm + Ttn + Ep \quad (1)$$
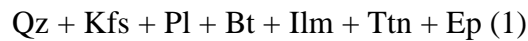
As a general feature, mylonites of this domain display (i) feldspar porphyroclasts wrapped by (ii) quartz ribbons or (iii) embedded in a fine-grained, recrystallized, feldspathic matrix. In the following, microstructures are described in regard of these aspects.

4.4.2.1.   Porphyroclasts

Porphyroclasts are mainly composed of K-feldspar and plagioclase with grain sizes between 500 µm and 5 cm (Fig. 3a, c and 4c). The clasts are rounded, display perthitic textures and mechanically induced twins. Myrmekite occurs locally in some porphyroclasts. Amphibole grains are partially altered to biotite and represent relicts of the magmatic assemblage that was not completely consumed during metamorphism, thereby acting as rigid particles that are mainly affected by brittle deformation (Fig. 4b and c).

The porphyroclasts exhibit microfractures that eventually crosscut the entire clast, originating fragments that have irregular shapes and sizes (50 – 200 µm). Fractures that terminate within the grain do not show any visible offset; transgranular fractures, on the other hand, have kinematic offsets up to 1 cm and, when systematically distributed within the porphyroclast, may result in bookshelf-like structures. Dilatant fractures have a variable offset, from few microns (~5 µm; Fig. 4d) to mm-scale (±10 mm; Fig. 3c).

4.4.2.2. Quartz ribbons

Quartz ribbons comprise polycrystalline elongated quartz grains with variable axial ratios (2:1 – 30:1; Fig. 4e). The mean grain size (~ 40 µm) and boundaries are commonly straight within the internal parts of the ribbon. In the ribbon walls, grain growth is prevented by the presence of second phases (Herwegh *et al.* 2011). The axial ratio of recrystallized quartz grains varies within the ribbon, increasing when the ribbon is bounded by porphyroclasts. Some elongated grains present small protuberances in their tips, indicating the presence of fine-grained bulges towards the neighbor grain (Fig. 4e). Less elongated grains (2:1 – 5:1 axial ratio) are typically smaller (~ 20 µm) and are mixed with biotite in the matrix. An oblique orientation of the ribbons in relation to the main foliation highlights the dextral component of shear (Fig. 4e).

4.4.2.3. Recrystallized matrix

Two types of matrix are defined, based on the mineral modal composition and microstructural characteristics:

(I) A feldspathic mixture of fine-grained plagioclase (56%) and K-feldspar (34%) with subordinate quartz (5%) and biotite (5%);

(II) Fine-grained aggregates of biotite (51%) and quartz (32%), with minor ilmenite, titanite and epidote (Fig. 4a and f).

The fine-grained feldspathic mixture (type I) displays grains with ± 15 µm in size with sub-elliptical shape and straight contacts (Fig. 4a and f). This matrix is always mixed with feldspar fragments derived from fractured porphyroclasts and does not show a visible shape-preferred orientation (SPO; Fig. 4f).

The matrix type II is parallel to quartz ribbons and the longer axis of feldspar porphyroclasts. Biotite has grain sizes between 20 and 200 µm and elongated shapes that define a SPO parallel to the direction of the mylonitic foliation. Isolated quartz grains are rounded and have grain sizes of ± 15 µm. This matrix domain typically defines abrupt contacts with the quartz ribbons (Fig. 4a).
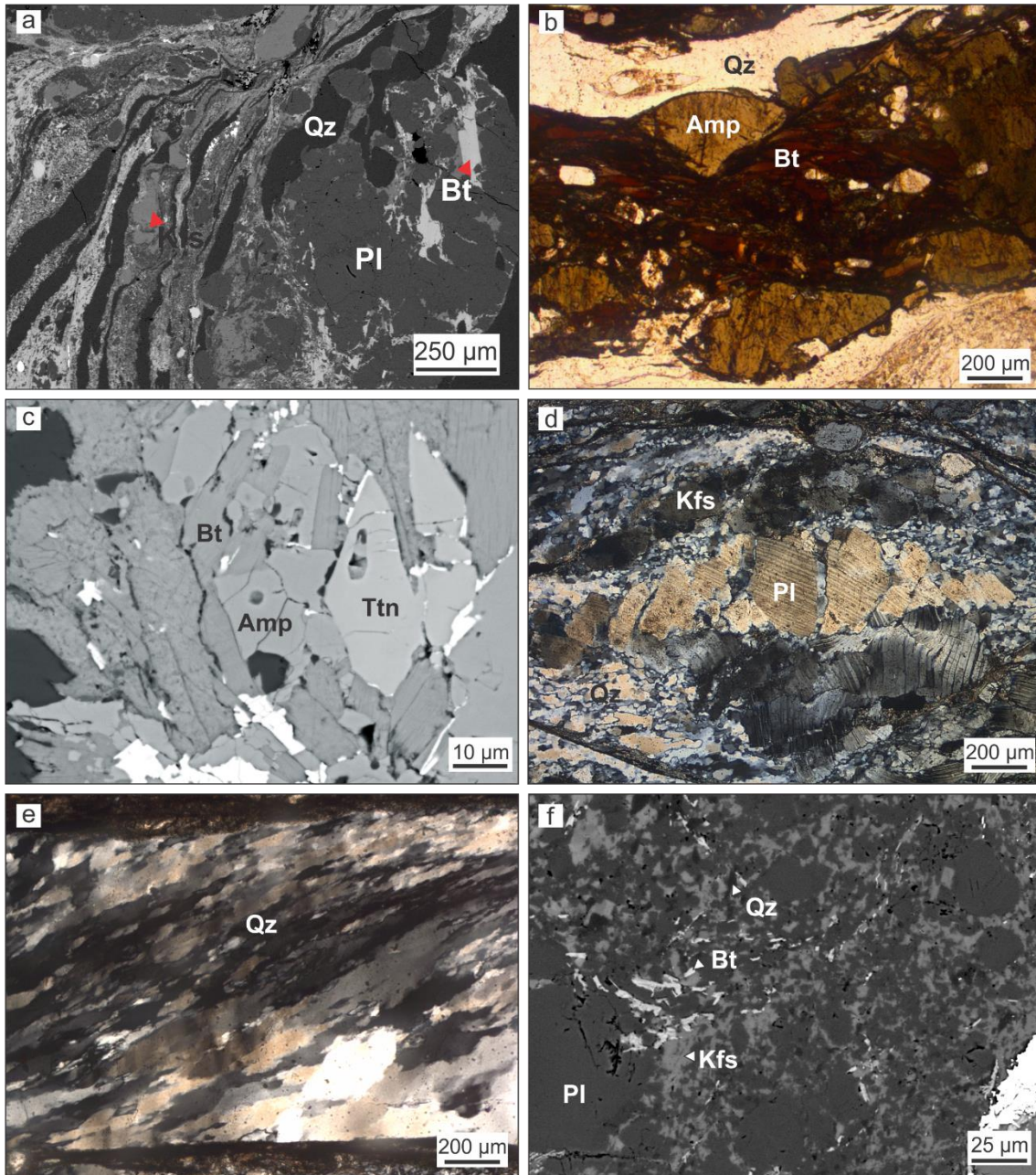
Fig. 4. Microstructures of the Caruaru domain. (**a**) Overview of typical mylonite microstructure showing quartz ribbons, fractured porphyroclasts and transition between distinct types of matrix. (**b**) Partial consumption of amphibole and generation of biotite at the edges of amphibole grains. (**c**) Coarse-grained amphibole grains wrapped by the preferred orientation of biotite laths and recrystallized quartz aggregates. Biotite partially results from the chemical replacement at the edges of amphibole grains. (**d**) Fractured plagioclase porphyroclasts showing fractures filled by matrix type I. Bent twins are observed in the lower-right clast. (**e**) Mylonitic foliation defined by the preferred orientation of recrystallized quartz aggregates, indicating dextral sense of shear. (**f**) Matrix type I displaying fine-grained (~ 10 µm) K-feldspar and plagioclase.

4.4.3 Microstructures of the Gravatá domain

The banded ultramylonites of this sector are composed of quartz (29%), K-feldspar (25%), plagioclase (22%), biotite (13%) and accessory epidote, garnet, titanite, hematite and zircon. The bands have straight boundaries and are mainly composed of alternating layers of i) Feldspars + mafic phases and ii) Quartz-rich bands (Fig. 5a).

4.4.3.1.   Feldspathic-mafic layer

These layers are composed of a combination of K-feldspar and plagioclase associated with biotite + epidote ± hematite ± titanite ± garnet. They have two recognizable domains, one dominated by biotite and mafic minerals and another dominated by a feldspathic aggregate. Both layers wrap around coarse K-feldspar, plagioclase and – locally - garnet porphyroclasts.

Porphyroclasts immersed in feldspathic-mafic layers have grain sizes between 0.01 and 3 cm and are composed of K-feldspar and plagioclase that are invariably fractured, resulting in irregular-shaped fragments of ~ 0.1 – 10 mm (Fig. 5a). The longer axis of porphyroclasts is parallel or subparallel to the mylonitic foliation. Local alteration on the edges of these clasts is present at the contacts with the mafic layer. When surrounded by layers dominated by feldspathic aggregates, the porphyroclasts are more intensively fractured, reducing the average grain-size to ± 1.5 cm (Fig. 5a). K-feldspar and plagioclase porphyroclasts display concentric extinction, bent twins and recrystallized tails showing fine-grained blob-like recrystallized quartz grains (Fig. 5b). Garnet porphyroclasts display dilatational fractures and are associated with the mafic layers, surrounded by epidote and biotite.

Fractures terminate within porphyroclasts or crosscut them entirely, displaying synthetic and antithetic asymmetry with kinematic offsets up to 200 µm. Extensional microfractures are filled by fragments and recrystallized grains of feldspar and biotite (Fig. 5a, c and d).

The mafic bands are characterized by discontinuous, ± 1 cm thick layers of biotite + epidote. Biotite has a grain size of ± 50 µm while epidote is typically ± 20 µm. Both phases are elongated parallel to the banded planar fabric and occur filling fractures and wrapping around porphyroclasts of K-feldspar, plagioclase and garnet (Fig. 5c). The

matrix and strain shadows associated with garnet pseudomorphs are mostly composed of a combination of quartz + epidote + biotite + hematite + K-feldspar (Fig. 5d).

Layers dominated by K-feldspar-plagioclase aggregates have grains with sub-elliptical, equant shapes and sizes of ± 5 µm. The feldspar mixture is interlayered with quartz bands and develops straight/abrupt contacts with secondary phases, defining the felsic component of the ultramylonite banding. The distribution between K-feldspar and plagioclase is heterogeneous along the layer (Fig. 5e); K-feldspar commonly occurs as fractured porphyroclasts that may be surrounded by the feldspathic aggregates, while plagioclase occurs as fine grains within the layer (Fig. 5e and f). These relic K-feldspar clasts are elongated and oriented alongside the compositional banding, defining the feldspathic ultramylonites at the mesoscale (Fig. 3e).

4.4.3.2. Quartz-rich bands

Quartz bands display equigranular, fine-grained (±15 µm) recrystallized grains (93%) and rare, elongated relict porphyroclasts (7%). The clasts are up to 3.6 mm in length, are parallel to the mylonitic layering and have aspect ratios ranging between 5:1 – 45:1. A sweeping undulose extinction is common in these grains (Fig. 5f). Fine-grained quartz aggregates display straight to slightly lobate contacts, are equant in size and show internal subgrains slightly smaller than the size of the recrystallized grains (~ 8 µm; Fig. 5f).
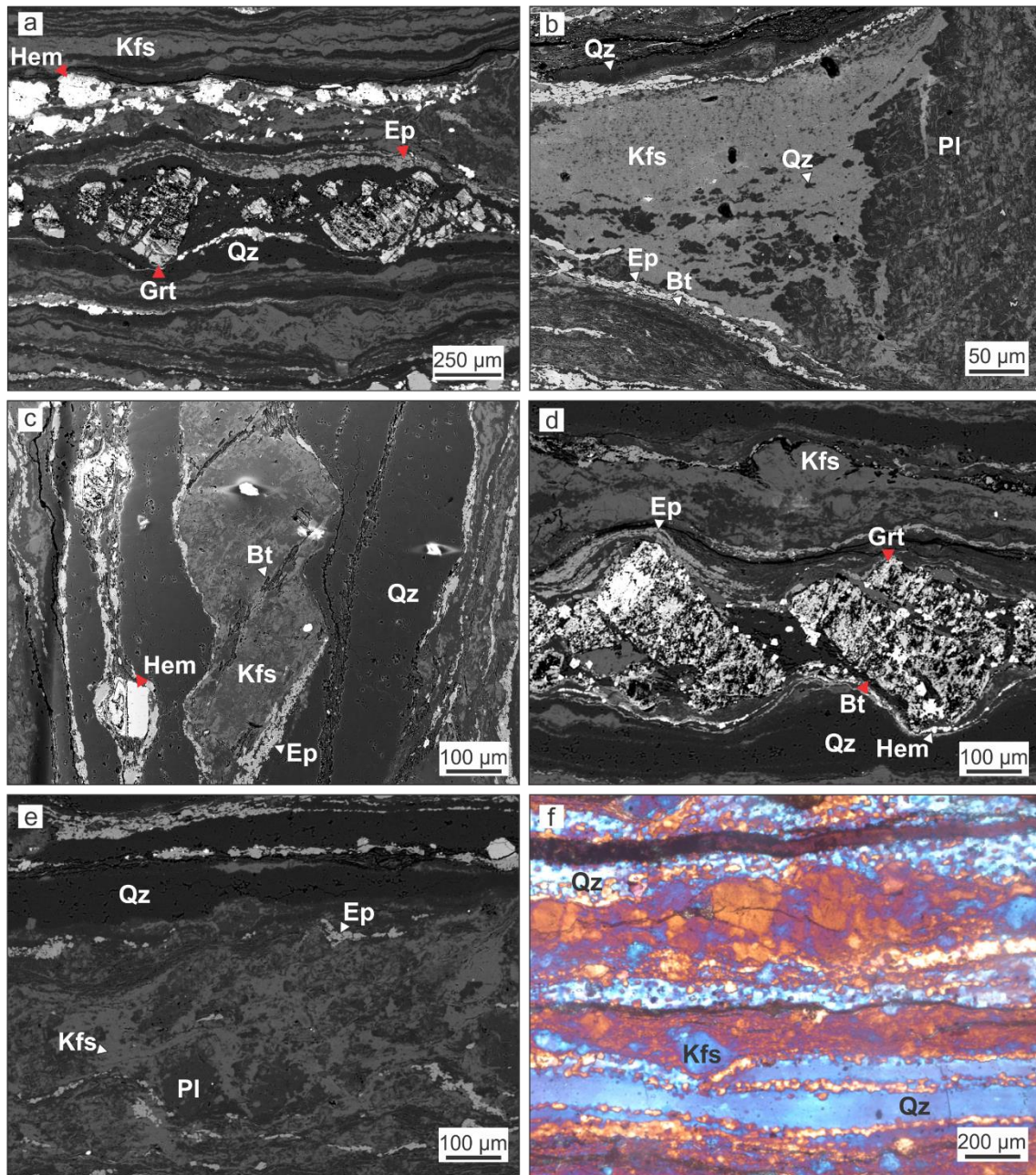
Fig. 5. Microstructures from the Gravatá domain. (**a**) Overview of typical ultramylonite displaying a banded texture with segregation of quartz rich layers and feldspathic + mafic layer and garnet pseudomorph and with pull-apart microfracture. (**b**) Strain shadow of plagioclase porphyroclast displaying anhedral quartz grains and segregation between K-feldspar in the core and epidote + biotite in the rim. (**c**) Fractured K-feldspar porphyroclast with dextral kinematic offset filled by biotite. (**d**) Fractured garnet pseudomorph in contact with polyphase mixture of Qz + Ep + Bt + Hem + Kfs and hybrid extensional/shear fracture filled with biotite (**e**) K-feldspar and plagioclase dominated matrix wrapping around feldspar fragments. Quartz ribbon at the top of the image. (**f**) Contrast of axial ratios of recrystallized quartz-rich layer (top) and elongated quartz grain (bottom).

4.4.4 EBSD Analysis of quartz CPO

4.4.4.1. Caruaru domain

Crystallographic preferred orientations in recrystallized quartz grains from the mylonites of the Caruaru domain show a monoclinic symmetry with *c*-axis maxima clustering at the Y position, with transitional maxima located between intermediary positions between Y and Z (Fig. 6a). The observed pattern resembles a scattering of orientations that suggests a transitional character between prism and rhomb slip positions. The *a*-axes cluster along peripheral positions obliquely oriented between Z and X.

The misorientation angle distributions histogram shows a peak of correlated grains between 10 to 30° which exceeds the theoretical curve and another peak between 50 and 60°, which are likely associated with Dauphiné twins (Fig. 6b).

4.4.4.2. Gravatá domain

In this domain (Figs. 6c and d), crystallographic preferred orientations of the quartz (0001) axes define a scattered distribution along Y and Z, with main clusters at 30° counterclockwise to Z and in-between Y and Z (Fig. 6c). An incipient concentration is present towards the Y-axis (Fig. 6c). The *a*-axes distributions show maxima in the periphery of the diagram, asymmetrically close to X, defining a small angle in respect to the main stretching lineation (Fig. 6c). The orientations of the *a*-axes show two maxima at the XZ plane, perpendicular to the *c*-axis orientations.

The misorientation angle distributions show a high frequency of low-angle mismatch between neighboring grains (Fig. 6d), suggesting the presence of low-angle boundaries in the recrystallized aggregates. Peaks between 50-60° are related to the presence of Dauphiné twinning and have the same frequency as predicted by the random distribution (Fig. 6d).
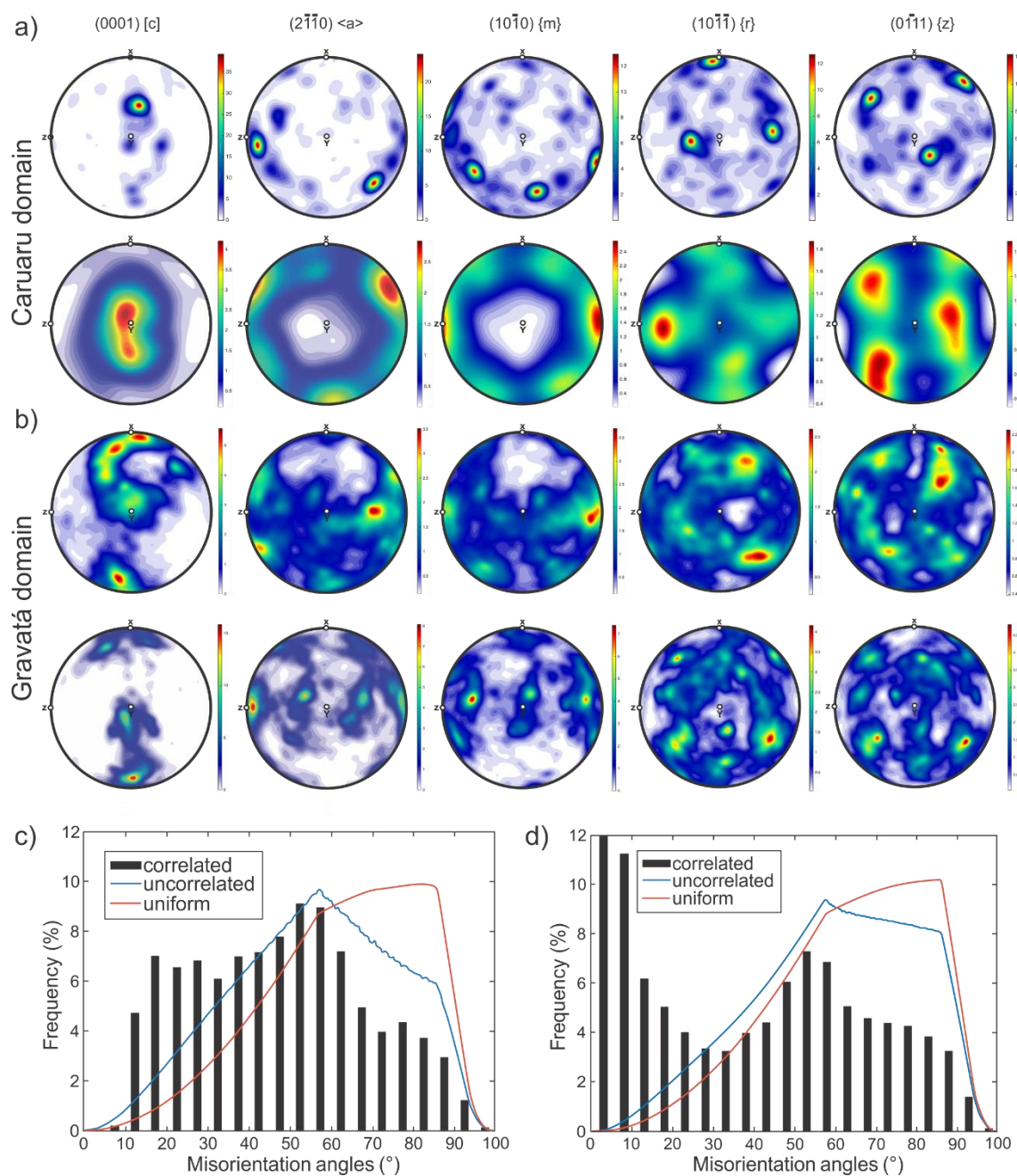
Fig. 6. EBSD results for the mylonitic fabrics of the EPSZ. (**a**) Pole figures from mylonites of the Caruaru domain. (**b**) Pole figures from the mylonites of the Gravatá domain. (**c**) Misorientation angle distributions for recrystallized quartz grains of Caruaru domain. (**d**) Misorientation angle distributions for recrystallized quartz grains of Gravatá domain. See text for discussion.

4.4.5 Mineral Chemistry

In the Caruaru domain, no systematic compositional variation is noticed in feldspar porphyroclasts, although recrystallized fractures and matrix show a decrease in Or and An contents (Fig. 7a and b). Orthoclase content (Or_{94}) in K-feldspar decreases

from porphyroclasts to the aggregates in the recrystallized matrix (Or_{72}). This decrease of orthoclase content is primarily seen in the rim of the recrystallized grains within the matrix, while the cores commonly show a minor variation trend. Grains filling fractures have Or contents overlapping that of the porphyroclasts (Fig. 7a).

Anorthite content in plagioclase is higher in porphyroclasts (An_{26}) than in the recrystallized grains of the matrix (An_{22}), classifying both as oligoclase (Fig. 8a). The fine-grained, recrystallized grains that fill fractures are almost pure albite (An_2) and show no visible trends in relation to porphyroclast-matrix compositions (Figs. 7b and 8a).

Chemical analyses of K-feldspar from the Gravatá domain point to similar compositions between porphyroclasts, recrystallized matrix and grains filling fractures (Fig. 7c, d). Orthoclase contents (Or_{80-98}) are similar in all three microstructural domains (Fig. 8b).

Plagioclase porphyroclasts have low An contents (An_{2-22}) with a cluster near An_{20} (Fig. 7d). Recrystallized grains in the matrix and within fractures have similar An contents (An_{2-10}) and a higher Ab content (Ab_{90}) when compared with porphyroclasts (Fig. 7d). Plagioclase porphyroclasts are largely classified as oligoclase while recrystallized matrix and grains within fractures are mostly albite (Fig. 8b).
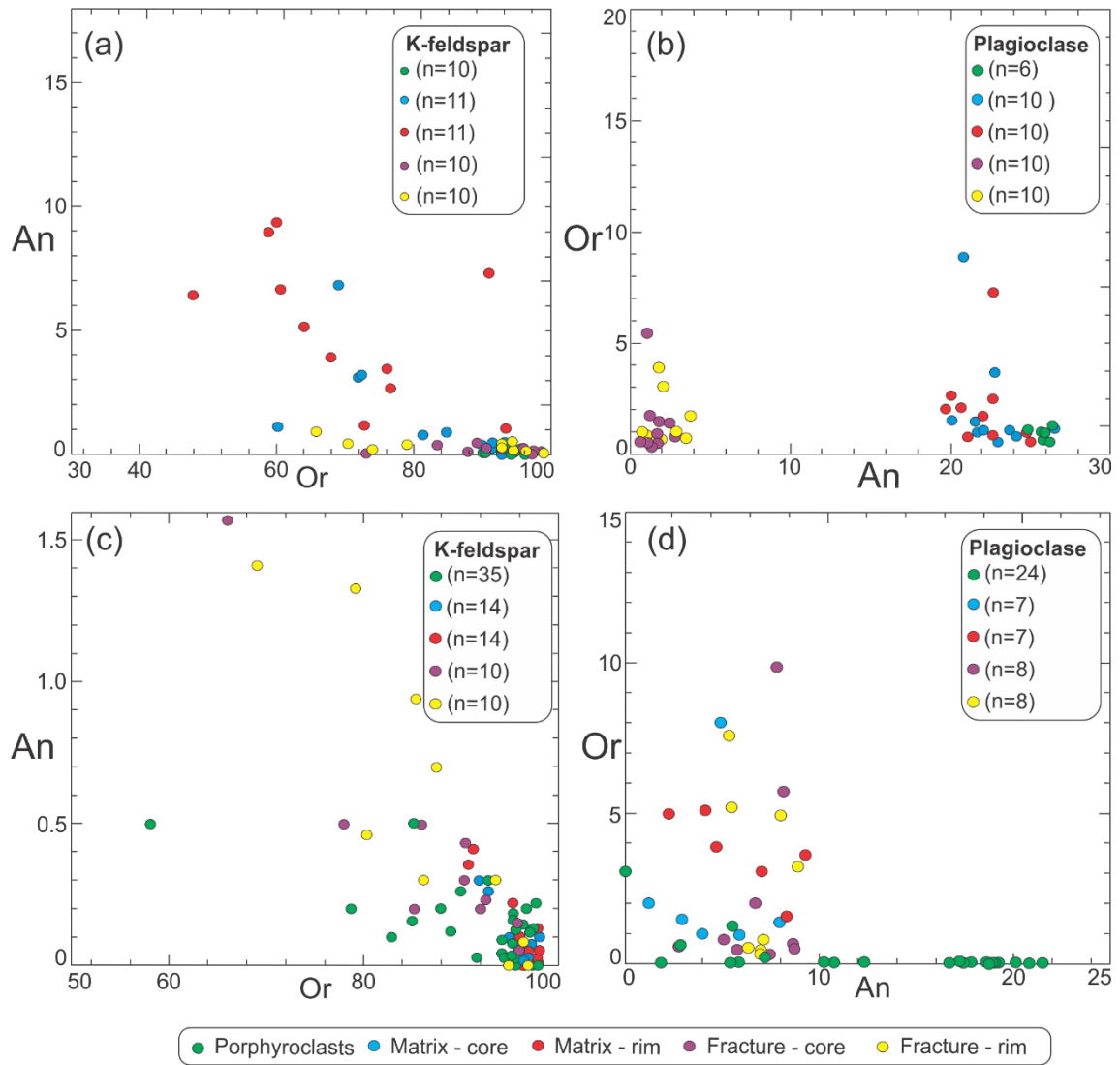
Fig. 7. Chemical composition of K-feldspar and plagioclase porphyroclasts, grains within fractures and fine-grained, recrystallized matrix: (**a**,**b**) Caruaru domain and (**c**,**d**) Gravatá domain.
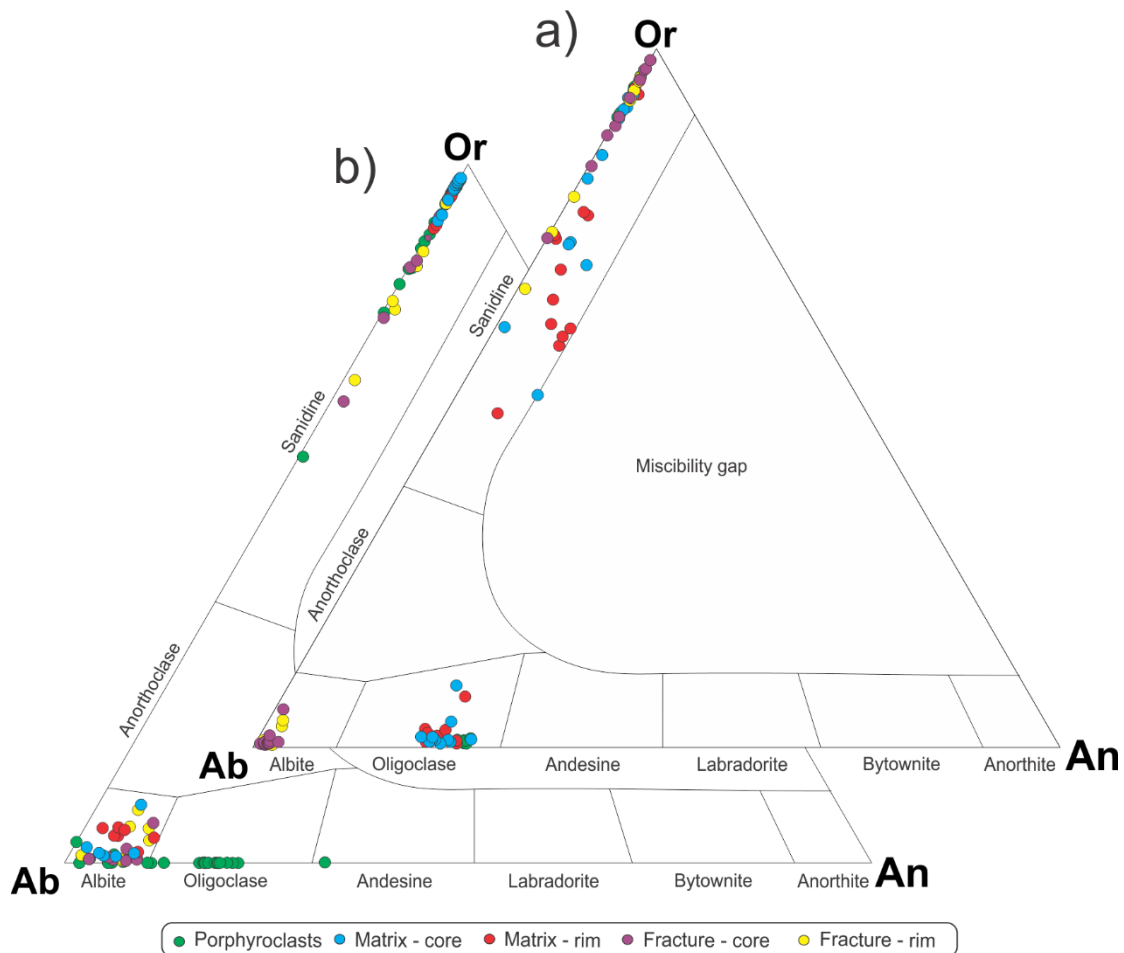
Fig. 8. Feldspar classification diagrams for (**a**) Caruaru domain and (**b**) Gravatá domain. See text for discussion.

4.4.6 Thermodynamic Modelling

Tables 1 and 2 present the bulk chemical compositions used for the modelled pseudosections and mineral chemistry used for isopleth intersection thermobarometry. Table 3 displays the estimated modal composition by point counting technique for the Caruaru and Gravatá domains and the modal composition modelled in both pseudosections.

Additional constraints on the temperature of deformation were assessed via the two-feldspars geothermometer of Barth (1951). T conditions were calculated from 1 to 10 kbar, although only representative values are plotted in the pseudosections. The calculations used for the geothermometer follow the review of Putirka (2008).

	Caruaru Domain													
	Bulk Composition (XRF)	Plagioclase					K-feldspar					Biotite	Ilmenite	Epidote
		Porphyroclast	Recrystallized		Incracrystalline fractures		Porphyroclasts	Recrystallized		Incracrystalline fractures		Recrystallized	Recrystallized	Recrystallized
			Core	Rim	Core	Rim		Core	Rim	Core	Rim			
SiO_2	63.34	61.73	60.06	61.29	67.62	67.41	64.17	62.88	63.57	64.24	64.41	34.78	0.1	38.19
TiO_2	0.89	0.05	b.d.l.	b.d.l.	0.05	b.d.l.	0.06	b.d.l.	b.d.l.	b.d.l.	b.d.l.	4.01	52.89	b.d.l.
Al_2O_3	14.92	23.90	23.63	23.18	18.58	18.56	18.08	18.67	18.10	17.48	17.45	13.45	b.d.l.	26.57
$Cr2O3$	b.d.l.	b.d.l.	b.d.l.	0.07	b.d.l.	0.02	b.d.l.	0.07	b.d.l.	b.d.l.	0.04	b.d.l.	0.05	b.d.l.
FeO	5.39	0.20	0.23	0.23	0.01	0.08	0.05	b.d.l.	b.d.l.	0.03	0.11	23.23	41.59	8.82
MnO	b.d.l.	0.02	b.d.l.	0.05	b.d.l.	b.d.l.	b.d.l.	b.d.l.	0.01	0.02	0.07	0.39	4.27	b.d.l.
MgO	1.83	b.d.l.	b.d.l.	0.03	b.d.l.	b.d.l.	b.d.l.	b.d.l.	b.d.l.	b.d.l.	b.d.l.	7.97	0.02	0.42
CaO	1.52	5.23	5.53	5.02	0.13	0.40	0.03	0.67	0.15	0.04	0.05	0.02	0.02	24.97
Na_2O	2.30	8.16	8.35	8.33	11.02	10.99	0.65	2.83	2.94	0.48	0.65	0.08	0.01	0.98
K_2O	7.41	0.17	0.21	0.17	0.10	0.12	15.81	12.70	12.60	16.19	16.07	9.71	0.01	0.06
Total	97.60	99.46	98.01	98.37	97.54	97.59	98.86	97.84	97.42	98.59	98.91	93.64	98.96	100.01
Si		2.76	2.72	2.77	3.04	3.03	3.00	2.93	2.98	3.02	3.01			
Ti		b.d.l.	b.d.l.	b.d.l.	b.d.l.	b.d.l.	b.d.l.	b.d.l.	b.d.l.	b.d.l.	b.d.l.			
Al		1.26	1.26	1.23	0.98	0.98	1.00	1.02	1.00	0.97	0.96			
Cr		b.d.l.	b.d.l.	b.d.l.	b.d.l.	b.d.l.	b.d.l.	b.d.l.	b.d.l.	b.d.l.	b.d.l.			
Fe		0.01	b.d.l.	0.01	b.d.l.	b.d.l.	b.d.l.	b.d.l.	b.d.l.	b.d.l.	b.d.l.			
Mn		b.d.l.	b.d.l.	b.d.l.	b.d.l.	b.d.l.	b.d.l.	b.d.l.	b.d.l.	b.d.l.	b.d.l.			
Mg		b.d.l.	b.d.l.	b.d.l.	b.d.l.	b.d.l.	b.d.l.	b.d.l.	b.d.l.	b.d.l.	b.d.l.			
Ca		0.25	0.27	0.24	0.01	0.02	b.d.l.	0.03	0.01	b.d.l.	b.d.l.			
Na		0.71	0.73	0.73	0.96	0.96	0.06	0.26	0.27	0.04	0.06			
K		0.01	0.01	0.01	0.01	0.01	0.94	0.75	0.75	0.97	0.96			
An (%)		25.88	26.47	24.71	0.63	1.96	0.16	3.20	0.73	0.19	0.25			
Ab (%)		73.13	72.35	74.29	98.81	97.36	5.84	24.47	25.98	4.27	5.73			
Or (%)		0.97	1.16	0.98	0.56	0.68	93.98	72.31	73.29	95.54	94.02			

Table 1. Representative chemical analyses from mylonites of the Caruaru domain.

	Gravatá Domain												
	Bulk Composition (XRF)	Plagioclase					K-feldspar					Hematite	Epidote
		Porphyroclats	Recrystallized		Incracrystalline fractures		Porphyroclats	Recrystallized		Incracrystalline fractures		Recrystallized	Recrystallized
			Core	Rim	Core	Rim		Core	Rim	Core	Rim		
SiO_2	69.43	64.83	65.90	66.37	65.71	68.52	64.98	64.12	63.27	63.64	62.72	0.06	39.6
TiO_2	0.37	0.12	b.d.l.	0.15	0.09	0.16	b.d.l.	0.01	b.d.l.	0.04	0.05	0.25	0.02
Al_2O_3	13.31	20.99	19.13	18.94	20.89	18.81	17.56	18.13	17.60	18.35	17.77	0.03	21.01
$Cr2O3$	0.00	0.09	0.06	b.d.l.	0.05	b.d.l.	b.d.l.	b.d.l.	b.d.l.	b.d.l.	0.04	b.d.l.	0.01
FeO	2.84	b.d.l.	b.d.l.	0.20	0.05	b.d.l.	0.01	b.d.l.	b.d.l.	0.03	0.01	94.5	12.3
MnO	b.d.l.	0.04	b.d.l.	b.d.l.	b.d.l.	0.01	b.d.l.	b.d.l.	0.12	0.13	b.d.l.	0.02	0.34
MgO	0.29	b.d.l.	0.02	0.02	b.d.l.	b.d.l.	0.01	0.01	0.03	b.d.l.	b.d.l.	b.d.l.	0.04
CaO	1.54	3.49	0.80	1.02	1.95	1.47	0.05	b.d.l.	0.03	0.04	b.d.l.	b.d.l.	22.38
Na_2O	3.95	9.13	11.62	10.87	11.29	8.83	0.24	0.38	0.22	1.65	0.36	b.d.l.	0.01
K_2O	5.45	0.14	0.27	0.70	0.12	0.76	16.67	15.96	16.37	14.70	16.13	0.02	0.06
Total	97.18	98.82	97.79	98.26	100.16	98.56	99.51	98.61	97.63	98.58	97.08	94.88	95.77
Si		2.91	2.94	2.96	2.87	3.10	3.02	3.01	3.00	2.96	2.99		
Ti		b.d.l.	b.d.l.	b.d.l.	b.d.l.	0.01	b.d.l.	b.d.l.	b.d.l.	b.d.l.	b.d.l.		
Al		1.11	1.00	1.00	1.07	1.00	0.96	1.00	0.98	1.01	1.00		
Cr		b.d.l.	b.d.l.	b.d.l.	b.d.l.	b.d.l.	b.d.l.	b.d.l.	b.d.l.	b.d.l.	b.d.l.		
Fe		b.d.l.	b.d.l.	b.d.l.	b.d.l.	b.d.l.	b.d.l.	b.d.l.	b.d.l.	b.d.l.	b.d.l.		
Mn		b.d.l.	b.d.l.	b.d.l.	b.d.l.	b.d.l.	b.d.l.	b.d.l.	b.d.l.	0.01	b.d.l.		
Mg		b.d.l.	b.d.l.	b.d.l.	b.d.l.	b.d.l.	b.d.l.	b.d.l.	b.d.l.	b.d.l.	b.d.l.		
Ca		0.17	0.04	0.05	0.09	0.07	b.d.l.	b.d.l.	b.d.l.	b.d.l.	b.d.l.		
Na		0.79	1.00	0.94	0.95	0.77	0.02	0.03	0.02	0.15	0.03		
K		0.01	0.02	0.04	0.01	0.04	0.99	0.96	0.99	0.87	0.98		
An (%)		17.43	3.59	4.71	8.66	7.99	0.22	b.d.l.	0.13	0.20	b.d.l.		
Ab (%)		82.57	94.97	91.40	90.68	87.07	2.10	3.47	1.99	14.55	3.27		
Or (%)		b.d.l.	1.43	3.88	0.65	4.93	97.67	96.52	97.87	85.24	96.72		

Table 2. Representative chemical analyses from mylonites of the Gravatá domain

	Caruaru Domain		Gravatá Domain	
Mineral Phase	Estimated (%)	Modelled (%)	Estimated (%)	Modelled (%)
Quartz	20	19	28	24
K-feldspar	36	41	25	34
Plagioclase	21	22	22	32
Biotite	19	11	12	3
Epidote	0.5	0.3	7	2
Titanite	1	0.04	2	0.5
Ilmenite	0.2	2	-	-
Hematite	-	-	1	1
Garnet	-	-	2	2
Amphibole	0.4	0	-	-
Apatite	2	0	-	-
H_2O	-	5	1	1
Total	100	100	100	100

Table 3. Comparison between estimated and modelled composition for the pseudosection of the Caruaru and Gravatá domains.

4.4.6.1.   Caruaru domain

The stable mineral assemblage during the deformation peak is defined by K-feldspar + quartz + plagioclase + biotite + ilmenite + titanite + epidote (Fig. 9). This mineral assemblage is stable from 4.3 kbar at a temperature of 512 °C to 5 kbar with temperatures ranging from 530 to 661 °C (Fig. 9). The effective bulk-rock composition used for calculations was estimated by EDS analysis in a specific area that represents the stable mineral assemblage in the Caruaru domain, composed by: $SiO_2 = 64.05$, $TiO_2 = 0.9$, $Al_2O_3 = 15.08$, $FeO = 5.45$, $MgO = 1.85$, $CaO = 1.53$, $Na_2O = 2.32$, $K_2O = 7.49$, $O_2 = 0.3$, and $H_2O = 1$ (in wt.%). This composition represents a refinement from the XRF analysis (Table 1). Amphibole is not stable during the peak conditions, thus its breakdown and subsequent transformation to biotite (Fig. 4c) is explained by the following reaction (1a; Beach 1980):

$$2 \text{ hornblende} + 16H^+ = \text{biotite} + SiO_2 + 4.5 \, (Mg,Fe)^{2+} + 4 \, Ca^{2+} + Na^+ + 8 \, H_2O \quad (1a)$$
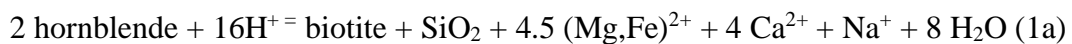
Mineral chemistry of recrystallized plagioclase from the matrix resulted in average 26% of anorthite which was used to constrain the stability field associated with ductile deformation. Two-feldspars geothermometry estimates were applied on the recrystallized grains that fill fractures. This microstructural domain was chosen because the grains within fractures are thought to be essentially derived from

recrystallization/nucleation processes, rather than dissolution-precipitation mechanisms that produced the polyphase matrix. In addition, the two-feldspar geothermometer yields conditions of 3.7 to 4.8 kbar and 483 ± 44 °C. The combination of the stable mineral assemblage, isopleths of anorthite contents in plagioclase and epidote modal volume constrain conditions of deformation of 4.75 ± 0.25 kbar and 526 ± 9°C (Fig. 9). The calculated temperature is within the error of the estimated values obtained with the two-feldspars geothermometer.
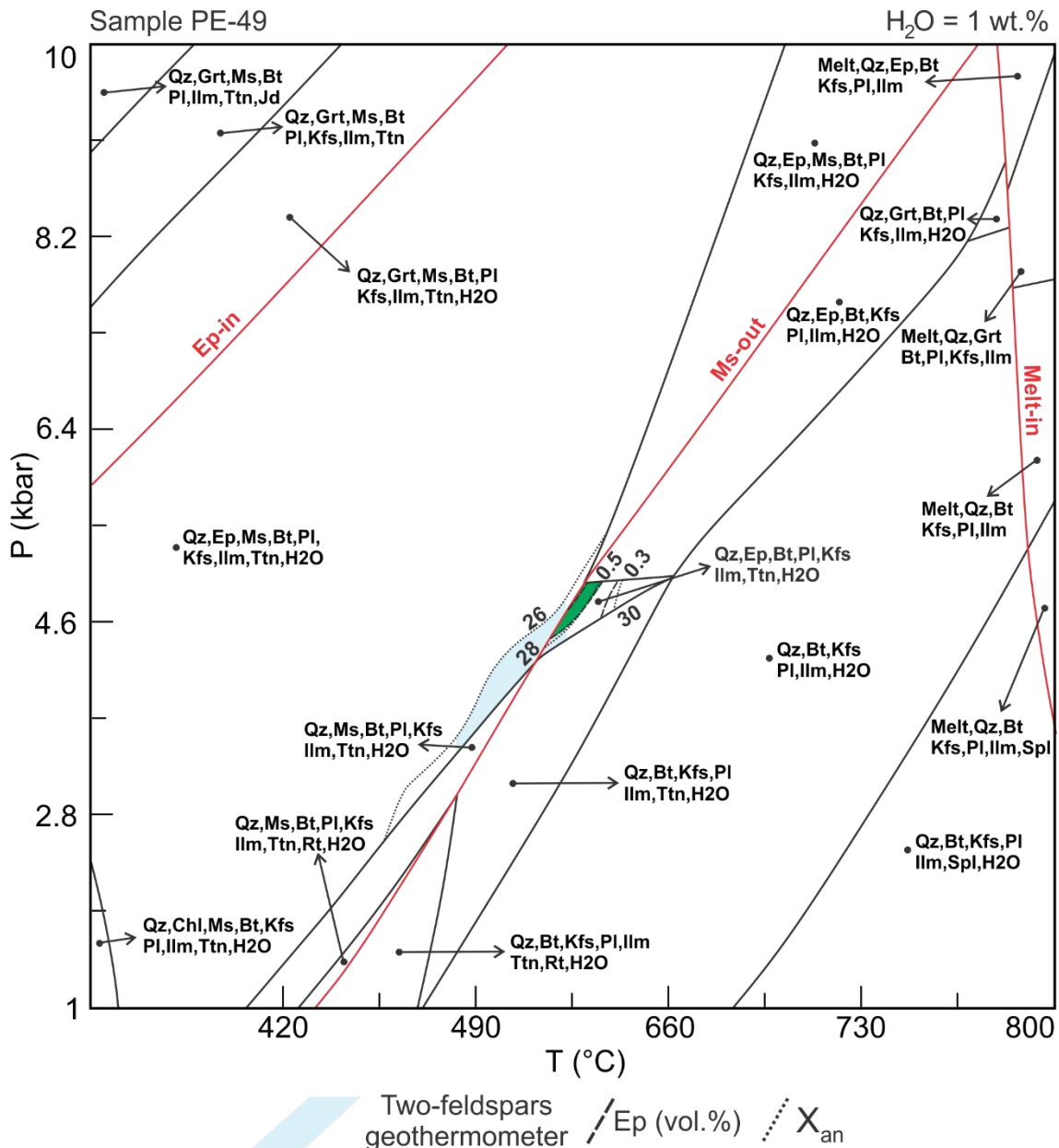
Fig. 9. P-T pseudosection in the NCKMASHTO system for the Caruaru domain. Red lines correspond to the limits of stability of minerals. Light-blue polygon corresponds to the upper limit of the two-feldspars geothermometer. Dash-lines correspond to isopleths of mineral chemistry and mineral modal composition. Estimated conditions of deformation are of 4.75 ± 0.25 kbar and 526 ± 9°C. See text for discussion.

4.4.6.2.   Gravatá domain

The mineral assemblage stable during the peak of deformation is defined by quartz + K-feldspar + plagioclase + epidote + biotite + hematite + titanite + garnet, which shows ranges of stability from 1 to 10 kbar, and 350-359°C and 525-542°C (Fig. 10). The modelled pseudosection used a bulk-rock composition that was determined by FRX analysis in: $SiO_2 = 70.91$, $TiO_2 = 0.38$, $Al_2O_3 = 13.59$, $FeO = 2.9$, $MgO = 0.3$, $CaO = 1.57$, $Na_2O = 4.03$, $K_2O = 5.56$, $O_2 = 0.26$, and $H_2O = 0.5$ (in wt.%) (Table 2).

Mineral chemistry of plagioclase in the recrystallized matrix yield anorthite contents between 4.5 and 5 mol.%. Contents of 1 vol.% of hematite and 2 vol. % of garnet were estimated for the mineral assemblage via modal estimates. Compositional and modal isopleths were used to constrain the peak conditions of deformation. Mineral chemistry of garnet was not possible to be determined because this mineral is weathered and appears locally as pseudomorphs in the rock (Fig. 5d).

Two-feldspars geothermometry was calculated based on recrystallized grains in the matrix and yields results of 412 ± 44 °C, which agrees within error with the temperature values estimated with mineral isopleth intersections (Fig. 10). The field in which the combined mineral assemblage, isopleths of mineral chemistry and modal compositions are stable yields conditions of 5.9 ± 1 kbar and 437 ± 17 °C (Fig. 10).
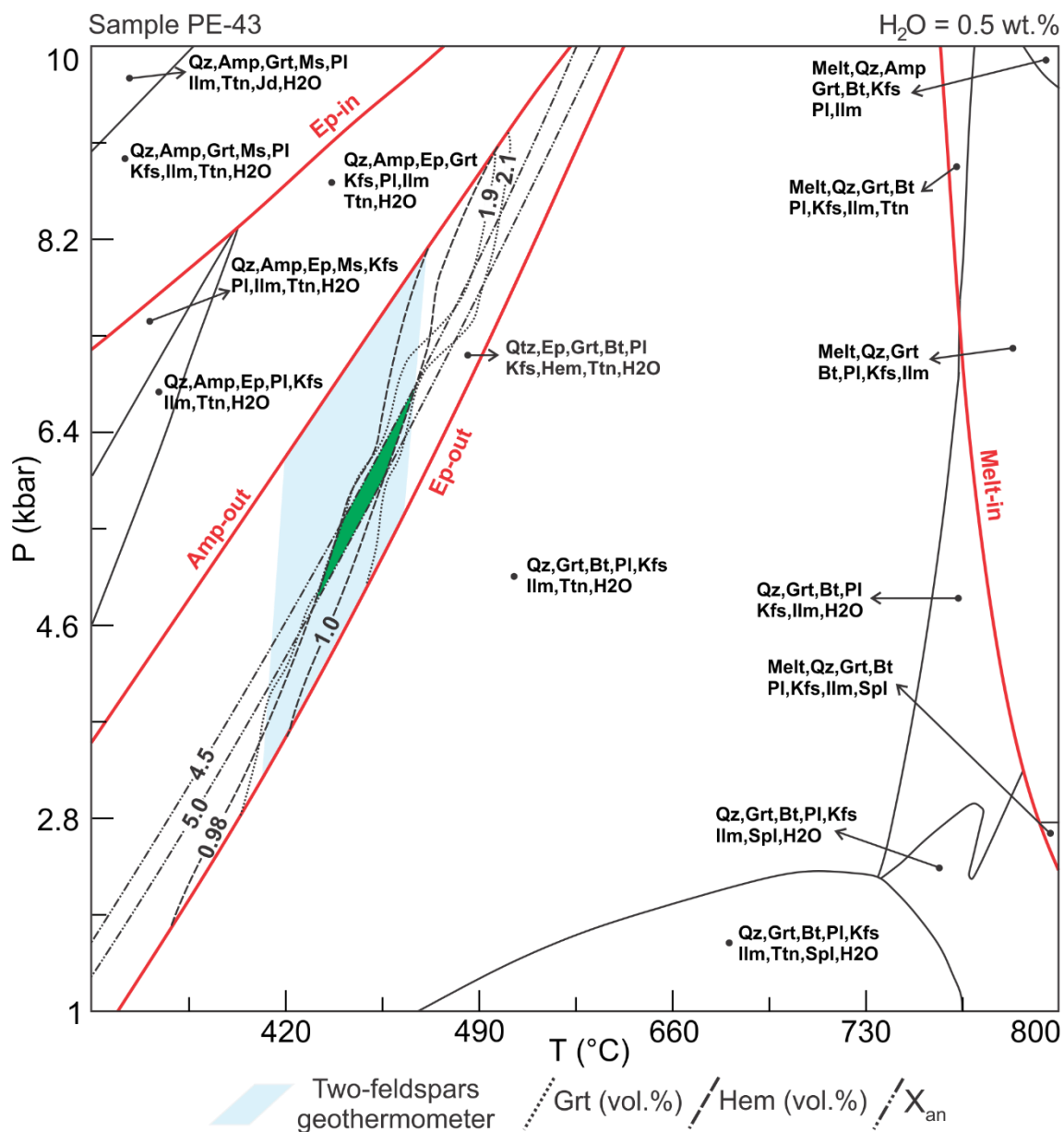
Fig. 10. P-T pseudosection in the NCKMASHTO system for the Gravatá domain. Red lines correspond to limit of stability of minerals. Light-blue polygon corresponds to the upper error of the two-feldspars geothermometer. Dash-lines correspond to isopleths of mineral chemistry and mineral modal composition. Estimated conditions of deformation are of 5.9 ± 1 kbar and 437 ± 17 °C. See text for discussion

4.5. Discussion

4.5.1 Pressure and temperature conditions of deformation

Quantitative and qualitative mineral and microstructural data indicate that the Caruaru domain was deformed at upper-amphibolite facies conditions, while the Gravatá domain evolved at mid-greenschist facies metamorphism.

49

Because the mylonitic granitoids of both domains have feldspars occurring both as porphyroclasts and recrystallized grains, the two-feldspar geothermometer was applied to constrain deformation temperatures (Barth 1951; Stormer 1975; Putirka 2008). Two important aspects are considered: (i) the nucleation of shear zones is associated with syn-kinematic metamorphic reactions that leads to re-equilibration of the metastable magmatic assemblage at the prevailing P-T conditions of deformation (Oliot *et al.* 2010), and; (ii) dynamic recrystallization is active during the evolution of the shear zone (Hirth & Tullis 1992).

The thermodynamic modelling was performed using both EDS and EPMA mineral chemistry data from representative mineral phases and textural domains of the deformed rocks. Effective bulk rock compositions of the Caruaru and Gravatá domains are similar to those reported for the Caruaru-Arcoverde batholith (Neves *et al.* 2000) and Encruzilhada de São João orthogneiss (França *et al.* 2019).

4.5.1.1. Caruaru domain

Mylonites from the Caruaru domain present the synkinematic mineral assemblage composed by K-feldspar + quartz + plagioclase + biotite + ilmenite + titanite + epidote. The combined data from pseudosection modeling and two-feldspar geothermometer approaches indicate deformational conditions of 480-570 °C and 3.2-5.1 kbar (Fig. 9). The anorthite content in recrystallized plagioclase in the matrix is 26 mol.%; however, the isopleths for this value cross a mineral stability field in the pseudosection where white mica is an additional stable phase, although very close to the white mica-out reaction (Fig. 9). Two possible explanations can be envisaged for this apparent inconsistency: (i) white mica should be considered as part of the stable mineral assemblage, or (ii) plagioclase equilibrated at a P-T condition where white mica was stable and a further temperature increase caused white mica consumption but plagioclase with An_{26} composition persisted as a metastable phase.

Available evidence points to the absence of white mica in the mineral assemblage. Thorough investigation of hand samples and thin sections revealed no grains – either magmatic and/or metamorphic – of white mica in the rock. The presence of thin needles of sericite along the cleavage planes of K-feldspar and plagioclase porphyroclasts could be taken as evidence for the local presence of white mica, but there is no microstructural

evidence that this white mica is synkinematic and was part of the stable mineral assemblage equilibrated during deformation. Such sericite needles are the product of late-stage alteration and, therefore, are not accounted for in the bulk chemical composition of the mylonites. Modal composition of minerals was obtained through conventional point counting (n = 1323) and no grain of white mica was observed. Additionally, there is no petrographical record of the presence of white mica in the mylonitized granitoids of the Caruaru domain (Neves & Mariano 1999; Neves *et al.* 2000; Mariano *et al.* 2007; Viegas *et al.* 2016; França *et al.* 2019).

Previous structural studies in the Caruaru domain highlighted the apparent fluid-deficient conditions in which strain was accommodated, resulting in the marked contribution of brittle deformation mechanisms to the overall mylonitization process (Neves & Mariano 1999; Viegas *et al.* 2016). Our data, on the other hand, present evidence that deformation in the Caruaru domain was at least locally assisted by fluids.

Amphibole is a recurrent phase in the Caruaru-Arcoverde batholith (Neves & Vauchez 1995) and its reaction to form biotite – the main mafic component observed in the Caruaru mylonites – releases H_2O (reaction 1a) that may be present during deformation in the shear zone. Myrmekite present at the edges of K-feldspar porphyroclasts is a result of exsolution reactions derived from local increase in stress at the tips of the clasts that faced the incremental shortening direction. Such incremental stress perturbations typically lead to a volume reduction of up to ~8%, subsequently resulting in local stress relaxation and local development of microporosity and micropermeability (Simpson & Witsch 1989).

The proposed reaction to form myrmekite inherently implies that white mica is also formed during the process (Phillips 1980), or that K^+ cations are dissolved, assimilated by a fluid phase and precipitated as fine-grained, K-feldspar grains elsewhere (Simpson & Witsch 1989). The present body of evidence based on i) the absence of white mica in the stable mineral assemblage; ii) the preservation of myrmekite in the Caruaru mylonites; and iii) the fact that the thermodynamic modelling estimates yield reasonable results when calculated at H_2O-saturated conditions, allow us to suggest that dissolution-precipitation creep mechanisms were active during mylonitization in the Caruaru domain, and that such processes occurred in the presence of fluids (e.g. Menegon *et al.* 2006).

Thermodynamic modelling for the Caruaru domain predicted a minimum content of 1% of water to reproduce measured mineral modes and compositions. Such conditions would be mainly observed in the development of the fine-grained matrix of feldspar and quartz, which may be partially derived from different deformation mechanisms (e.g., fracturing in feldspar, bulging recrystallization of quartz). Therefore, combining P-T estimates derived from thermodynamic modelling, two-feldspars geothermometry and microstructures, we conclude that P and T conditions of deformation in the Caruaru domain were in the range of 4.75 ± 0.25 kbar and 526 ± 9°C, which are consistent with upper greenschist-facies metamorphism locally assisted by fluids. Furthermore, these conditions also point out to an isobaric heating path, which is mainly evidenced by the preservation of metastable plagioclase followed by white mica consumption.

Thus, our results allow us to suggest that: 1) there is evidence that local fluid activity may have had a role in weakening and subsequent strain localization in the Caruaru domain mylonites; 2) the constrained P-T estimates for mylonitization in this domain are compatible with upper greenschist facies conditions. The local influence of fluids during shear deformation would contribute to further weakening of the mylonitic fabric and the development of fine-grained polyphase mixtures, which may be initially triggered by mechanical fragmentation at high-stress conditions (e.g. Viegas *et al.* 2016).

4.5.1.2.   Gravatá domain

The synkinematic mineral assemblage of this domain is defined by quartz + K-feldspar + plagioclase + epidote + biotite + hematite + titanite + garnet. Within this stability field in the modeled pseudosection, intersections of compositional and modal isopleths of plagioclase, garnet and hematite and results from the two-feldspars geothermometry indicate best-fit deformational conditions of 5.9 ± 1 kbar and 437 ± 17 ºC (Fig. 10).

Thermodynamic modelling of the Gravatá domain predicts that garnet is part of the stable mineral assemblage. The modelled ultramylonite sample shows garnet as a pseudomorph, which prevents the determination of its chemical composition.

The ultramylonite structure displays fine-grained quartz grains and elongated porphyroclasts with axial ratio up to 45:1. The fine-grained, recrystallized quartz grains are equant in size (± 10 µm) equant shapes (Fig. 5f), with elongated grains displaying

small bulges on their periphery. These microstructures suggest that quartz was recrystallized through transitional bulging recrystallization - subgrain rotation recrystallization (BLG-SGR) mechanisms (Stipp *et al.* 2002*a*; Passchier & Trouw 2005). Several works indicate that the temperature range for SGR recrystallization in quartz lies between 420 and ~510°C (Stipp *et al.* 2002*a, b*; Tullis 2002). Nevertheless, these estimates should be considered with caution in light of the coupled major dependence of strain rate (Stipp *et al.* 2002*b*) and water weakening.

Geothermometric calibrations (Faleiros *et al.* 2010; Law *et al.* 2010) propose that the temperature for the BLG-SGR transition is in the order of 390-420°C. Taking into consideration that SGR is the dominating mechanism of recrystallization and that BLG recrystallization is also important in the process, we expect the temperature of deformation to be close to that proposed for the BLG-SGR transition (390-420°C).

Thus, the combining evidence from microstructures, chemical analyses, thermodynamic modelling and geothermometry of synkinematic mineral phases indicate that the Gravatá domain was deformed at 437 ± 17°C and 5.9 ± 1 kbar. Such conditions are consistent with mid greenschist-facies metamorphism and indicate lower-grade mylonitization conditions in the Gravatá domain. It is worth pointing out that the slightly higher-T conditions for the BLG-SGR transition observed in the Gravatá domain may be a result of fast strain rates during shear zone deformation, as has been documented in both experimental and natural examples (e.g. Stipp *et al.* 2002*b*).

4.5.2 Deformation Mechanisms

4.5.2.1. Caruaru domain

EBSD results indicate the presence of small quartz grains (≤20 µm) without internal dislocations, while larger grains (≥ 40 µm) show some internal misorientation. CPO analysis indicates that quartz grains are deformed by dislocation creep with activation of prism<a> and minor, rhomb<a+c> slip systems (Fig. 6a). The observable microstructures of the recrystallized aggregates, mainly defined by rectilinear boundaries, subgrains with the same sizes of newly-formed grains with mean grain size of ~ 40 µm in aggregates point out to recrystallization mainly via rotational recrystallization (Fig. 4, 6a and 6b). Furthermore, low-angle boundaries identifiable in the misorientation

distribution (Fig. 6b) further suggest that recrystallization was accomodated by subgrain rotation recrystallization. Such slip system patterns are in agreement with previous works on the mylonites of the Caruaru region (Neves & Mariano 1999; Neves *et al.* 2000; Viegas *et al.* 2016), which mainly characterized solid-state flow conditions for these deformed granitoids.

When quartz grains are associated in type II matrix, they have rounded shape and occur as isolated single grains. These grains present no evidence of recrystallization or intracrystalline deformation and are interpreted as the remnant, reactant products of the consumption of feldspar porphyroclasts that took place during deformation. Such Si-material would form thin films that may precipitate within cavities along biotite-feldspar boundaries; their movement would be impeded by the pinning aspect of the polyphase matrix (e.g. Herwegh *et al.* 2011; Menegon *et al.* 2015).

Another possible explanation for strain-free isolated quartz grains is that myrmekite production continued until the late stages of mylonitization and the dissolved quartz would be precipitated as strain-free grains within the matrix (Tsurumi *et al.* 2003). However, given the limited occurrence of myrmekite in these mylonites and the typical presence of fine-grained, strain-free quartz grains within the recrystallized matrix, creep cavitation seems to be the most likely mechanism responsible for the nucleation of these fine-grained quartz aggregates. Such dissolution-precipitation processes have been commonly recognized in retrogressed mylonites (e.g. Hippertt 1994, Menegon *et al.* 2015).

Deformation of K-feldspar and plagioclase produced fragments of intermediate size between porphyroclasts and matrix that have the same chemical composition of porphyroclasts (Fig. 4a). These observations suggest that the smaller fragments were the product of mechanical fragmentation of larger clasts. On the other hand, plagioclase and locally K-feldspar show differences in chemical composition between porphyroclasts and the recrystallized matrix (Fig. 7a and 7b). This disparity indicates that grain size reduction in feldspars was the result of combined fracturing + nucleation/recrystallization, possibly enhanced by the presence of fluids (Fitz Gerald & Stünitz 1993).

The fact that fine-grained feldspar grains present no evidence for internal deformation and/or recrystallization features suggest that chemical differences between porphyroclasts and the recrystallized matrix are mainly due to the nucleation of new

grains during deformation. Fine-grained aggregates within the feldspathic mixture accommodate strain mainly via diffusion, while quartz aggregates deform via solid-state dislocation creep. Such patterns have been observed and recorded in medium- to high-grade deformation zones (e.g. Kilian *et al.* 2011; Menegon *et al.* 2013).

4.5.2.2. Gravatá domain

Microstructures, EBSD analysis and P-T conditions in this domain all point to deformation at mid greenschist-facies conditions. Recrystallized quartz grains show straight boundaries, average grain size of ~ 20 µm and are commonly segregated into shear bands that compose the layers of the ultramylonitic banding (Fig. 5). The spreading of the crystallographic preferred orientations, defining concentrations around Y and Z, indicates that ductile strain was mainly accommodated by slip on the basal<a> and rhomb<a+c> slip systems (Fig. 6c). Such CPO patterns are in agreement with the temperature estimates from the thermodynamic modelling (~ 430ºC), which point to deformation at the transitional boundary between bulging (BLG) and subgrain rotation recrystallization mechanisms (SGR; Stipp *et al.* 2002*a*; Faleiros *et al.* 2010, 2016).

The fine-grained, feldspathic-mafic layer exhibits plagioclase grains that display contrasting chemical compositions in relation to larger grains (i.e. Fig. 5a). Furthermore, the presence of a low-grade alteration assemblage of greenschist-facies minerals would indicate that plagioclase is kinematically replaced by epidote + chlorite, while K-feldspar deforms by fracturing and quartz bands undergo dynamic recrystallization.

These characteristics indicate that the Gravatá domain was subjected to lower metamorphic conditions than the Caruaru domain, and that fluid percolation had an influence on the development of ultramylonites in this domain, effectively facilitating the activity of diffusive mass transfer processes along compositionally heterogeneous layers (Fitz Gerald & Stünitz 1993; Fliervoet & White 1995). These interpretations are corroborated by the thermodynamic modelling results and the overall microstructural pattern of the Gravatá ultramylonites.

4.5.3 Tectonic implications

The tectonic significance of the East Pernambuco shear zone within the evolution of the Borborema Province has been widely debated (e.g. Neves *et al.* 2000 and references therein). The study of Neves & Mariano (1999) demonstrated the distinct metamorphic evolution of the structure, individualizing higher-T mylonites belts to the west of the EPSZ (in this study called the Caruaru domain), and lower-T mylonites in the eastern termination of the fault (equivalent to the Gravatá domain detailed in this study).

Through extensive fieldwork across the length of the shear zone, Neves & Mariano (1999) suggested that the EPSZ was developed in the late stages of the Neoproterozoic Brasiliano orogeny, being mainly classified as a second-order structure in the overall evolution of the Borborema Province.

More recently, França *et al.* (2019) constrained the age of the transcurrent motion across the EPSZ in ~ 591 Ma, via monazite U-Pb ages on mylonites from the Bezerros orthogneiss – located in the Gravatá domain. Based on similar geochronological ages in both the northern and southern parts of the fault, these authors favored the interpretation of the EPSZ as an intracontinental shear zone that developed in previous crustal discontinuities.

Our study presents quantitative data that draw on these interpretations and extend them, because: 1) there is evidence for deformation at decreasing metamorphic conditions from the Caruaru to the Gravatá domains, as constrained by robust thermodynamic modelling (Figs. 9 and 10); 2) quantitative microstructural and crystallographic fabric data document the activity of both higher- and lower-T slip systems in the Caruaru and Gravatá domains, respectively (Fig. 6a and 6c); 3) brittle-ductile deformation mechanisms are recorded across the entire length of the shear zone (Figs. 3, 4 and 5).

These observations suggest that: i) strain localization in the EPSZ was attained via brittle-ductile deformation mechanisms under both upper and mid greenschist-facies conditions; ii) Fluid activity, although heterogeneously distributed, was significant in localizing strain along the entire structure, as documented in dynamic recrystallization coupled with kinematically-induced, chemical replacement processes (e.g. sections 4.2, 5.1.1, 5.1.2); iii) deformation conditions show a combination of dynamic recrystallization and fracturing/dissolution-precipitation assisted by fluids in the both the Caruaru and

Gravatá domains, indicating that strain was heterogeneously accommodated due to distinct metamorphic conditions along the shear zone.

Hence, we postulate that the ESPZ is a discontinuous, dextral strike-slip shear zone that had history of deformation at crustal depths corresponding to the brittle-ductile transition. Such shear zones are mainly characterized by the interplay between frictional-viscous deformation mechanisms commonly recorded along retrograde metamorphic P-T paths (e.g. Handy *et al.* 2007) and are typically nucleated along pre-existing crustal discontinuities. In the case of the EPSZ, these characteristics are consistent with an heterogenous path of strain localization, which is possibly related to differences in exhumation rates along the length of the shear zone.

4.6. Conclusions

Based on meso- and microscale structures, bulk rock and mineral chemistry, thermodynamic modelling and constrained P-T conditions of deformation, the following conclusions can be drawn from this study:

1.   The EPSZ shows an interplay between brittle and ductile deformation mechanisms. Quartz is mainly recrystallized through solid-state, subgrain rotation recrystallization, while feldspar acts as a strong phase and is deformed by fracturing and heterogeneous, fluid-assisted dissolution-precipitation. Furthermore, crystallographic fabrics reveal the activation of slip systems compatible with the brittle-ductile transitional regime.

2.   Thermodynamic modelling constrained deformation conditions at 4.75 ± 0.25 kbar and $526 \pm 9°C$ for the Caruaru domain, and 5.9 ± 1 kbar and $437 \pm 17°C$ in the Gravatá domain. Such estimates are in agreement with those defined by Neves *et al.* (2000) and Viegas *et al.* (2016) for the Caruaru domain, and indicate the lower-temperature, mid greenschist-facies metamorphism observed in the Gravatá domain. Thermodynamic modelling combined with the microtextural characterization also indicates that fluid-assisted strain localization occurred along the entire length of the EPSZ.

3.   The brittle-ductile rheological behaviour of the EPSZ suggests that this structure had history of deformation at intermediate depths and subsequently

exhumed along an heterogenous path in the continental crust in the late stages of the Brasiliano-Pan-African tectonics that affected the South American Platform.

Acknowledgements

References

Barth, T.W. 1951. The feldspar geologic thermometers. *Neues Jahrbuch für Mineralogie*, **82**, 143-154.

Beach, A. 1980. Retrogressive metamorphic processes in shear zones with special reference to the Lewisian complex. *Journal of Structural Geology*, **2**, 257-263, https://doi.org/10.1016/0191-8141(80)90058-9

Brito Neves, B.B., Santos, E.J. & Van Schmus, W.R. 2000. Tectonic history of the Borborema Province, northeastern Brazil. *In*: Cordani, U.G., Milani, E.J., Thomaz Filho, A. & Campos, D.A. (eds) *Tectonic Evolution of South America*. 31st International Geological Congress, 151-182.

Bürgmann, R. & Dresen, G. 2008. Rheology of the lower crust and upper mantle: evidence from rock mechanics, geodesy and field observations. Annual review of Earth and Planetary Sciences, **36**, 531-567, https://doi.org/10.1146/annurev.earth.36.031207.124326

Connolly, J.A.D. 2005. Computation of phase equilibria by linear programming: A tool for geodynamic modeling and its application to subduction zone decarbonation. *Earth and Planetary Science Letters*, **236**, 524-541, https://doi.org/10.1016/j.epsl.2005.04.033

Davison, I. & Mccarthy, M. 1995. Laminar flow in shear zones: the Pernambuco Shear Zone, NE-Brazil. *Journal of Structural Geology*, **17**, 149-161, https://doi.org/10.1016/0191-8141(94)E0038-Z

Fagereng, A. & Toy, V.G. 2011. Geology of the earthquake source: an introduction. *Geological Society, London, Special Publications*, **359**, 1-16, http://dx.doi.org/10.1144/SP359.1

Faleiros, F.M., Campanha, G.A.C., Maria, R. & Fuzikawa, K. 2010. Quartz recrystallizations regimes, c-axis texture transition and fluid inclusion reequilibration in a prograde greenschist to amphibolite facies mylonite zone (Ribeira Shear Zone, SE Brazil). *Tectonophysics*, **485**, 193-214, https://doi.org/10.1016/j.tecto.2009.12.014

Faleiros, F.M., Moraes, R., Pavan, M. & Campanha, G.A.C. 2016. A new empirical calibration of the quartz c-axis fabric opening-angle deformation thermometer. *Tectonophysics*, **671**, 173-182, https://doi.org/10.1016/j.tecto.2016.01.014

Fitz Gerald, J.D. & Stünitz, H. 1993. Deformation of granitoids at low metamorphic grade. I: Reactions and grain size reduction. *Tectonophysics*, **221**, 269-297, https://doi.org/10.1016/0040-1951(93)90163-E

Fliervoet, T.F. & White, S.H. 1995. Quartz deformation in a very fine grained quartzo-feldspathic mylonite: a lack of evidence for dominant grain boundary sliding deformation. *Journal of Structural Geology*, **17**, 1095-1109, https://doi.org/10.1016/0191-8141(95)00007-Z

França, R.H.M., Neves, S.P., Bezerra, J.P.S. & Bruguier, O. 2019. Geochemistry and geochronology of orthogneisses across a major transcurrent shear zone (East Pernambuco shear zone, Borborema Province, Northeast Brazil): Tectonics implications. *Journal of South American Earth Sciences*, **91**, 285-301, https://doi.org/10.1016/j.jsames.2019.02.015

Fuhrman, M.L. & Lindsley, D.H. 1988. Ternary-feldspar modeling and thermometry. *American Mineralogist*, **73**, 201-215.

Green, E.C.R., White, R.W., Diener, J.F.A., Powell R., Holland, T.J.B. & Palin, R.M. 2016. Activity-composition relations for the calculation of partial melting equilibria in metabasic rocks. *Journal of Metamorphic Geology*, **34**, 845-869, https://doi.org/10.1111/jmg.12211

Guermani, A. & Pennacchioni, G. 1998. Brittle precursors of plastic deformation in a granite: an example from Mont Blanc massif (Helvetic, western Alps). *Journal of Structural Geology*, **20**, 135-148, https://doi.org/10.1016/S0191-8141(97)00080-1

Guimarães, I.P, Silva Filho, A.F., Silva Filho, Almeida, C.N., Van Schmus, W.R., Araújo, J.M.M., Melo, S.C. & Melo, E.B. 2004. Brasiliano (Pan-African) granitic magmatism in the Pajeú-Paraíba belt, Northeast Brazil: an isotopic and geochronological approach. *Precambrian Research*, **135**, 23-53, https://doi.org/10.1016/j.precamres.2004.07.004

Handy, M.R., Hirth, G. & Bürgmann, R. 2007. Continental fault structure and rheology from the frictional-to-viscous transition downward. *In*: Handy, M.R., Hirth, G. & Hovius, N. (eds) *Tectonics Faults: agents of change on dynamic earth*. Dahlem Workshop Reports, **1**, 139-181, https://doi.org/10.7551/mitpress/6703.001.0001

Herwegh, M., Linckens, J., Ebert, A., Berger, A. & Brodhag, S.H. 2011. The role of second phase for controlling microstructural evolution in polymineralic rocks: A review. *Journal of Structural Geology*, **33**, 1728-1750, https://doi.org/10.1016/j.jsg.2011.08.011

Hielscher, R. & Schaeben, H. 2008. A novel pole figure inversion method: specification on MTEX algorithm. *Journal of Applied Crystallography*, **41**, 1024-1037, https://doi.org/10.1107/S0021889808030112

Hippertt, J.F. 1994. Microstructures and *c*-axis fabrics indicative of quartz dissolution in sheared quartzites and phyllonites. *Tectonophysics*, **229**, 141-163, https://doi.org/10.1016/0040-1951(94)90026-4

Hirth, G. & Tullis, J. 1992. Dislocation creep regimes in quartz aggregates. *Journal of Structural Geology*, **14**, 145-159, https://doi.org/10.1016/0191-8141(92)90053-Y

Holland, T.J.B. & Powell, R. 1998. An internally consistent thermodynamic data set for phases of petrological interest. *Journal of Metamorphic Geology*, **16**, 309-343. https://doi.org/10.1111/j.1525-1314.1998.00140.x

Holland, T.J.B. & Powell, R. 2011. An improved and extended internally consistent thermodynamic dataset for phases of petrological interest, involving a new equation of state for solids. *Journal of Metamorphic Geology*, **29**, 333-383, doi:10.1111/j.1525-1314.2010.00923.x

Kilian, R., Heilbronner, R. & Stünitz, H. 2011. Quartz grain size reduction in a granitoid rock and the transition from dislocation to diffusion creep. *Journal of Structural Geology*, **33**, 1265-1284, https://doi.org/10.1016/j.jsg.2011.05.004

Law, R.D., Mainprice, D., Casey, M., Lloyd, G.E., Knipe, R.J., Cook, B. & Thigpen, J.R. 2010. Moine Thrust zone mylonites at the Stack of Glencoul: I – microstructures, strain and influence of recrystallization on quartz crystal fabric development. *Geological Society, London, Special Publications*, **335**, 543-577, https://doi.org/10.1144/SP335.23

Mariano, G., Silva, J.M.R., Correia, P.B., Neves, S.P., Cabral, A.F., Silva, F.M.J.V., Chagas, I.T., Miranda, T.S., Oliveira, S.F. & Freire, B.S. 2007. *Belo Jardim – SC.24-X-B-III, escala 1:100.000: nota explicativa*. Pernambuco: UFPE/CPRM.

Melo, E.Z.V. 1977. O sistema de falhas transcorrentes do nordeste brasileiro. *Boletim de Mineralogia*, **5**, 95-106.

Mancktelow, N.S. & Pennacchioni, G. 2005. The control of precursor brittle fracture and fluid-rock interaction on the development of single and paired ductile shear zones. *Journal of Structural Geology*, **27**, 645-661, https://doi.org/10.1016/j.jsg.2004.12.001

Menegon, L., Pennacchioni, G. & Stünitz, H. 2006. Nucleation and growth of myrmekite during ductile shear deformation in metagranites. *Journal of Metamorphic Geology*, **24**, 553-568, https://doi.org/10.1111/j.1525-1314.2006.00654.x

Menegon, L., Stünitz, H., Nasipuri, P., Heilbronner, R. & Svahnberg, H. 2013. Transition from fracturing to viscous flow in granulite facies perthitic feldspar (Lofoten, Norway). *Journal of Structural Geology*, **48**, 95-112, http://dx.doi.org/10.1016/j.jsg.2012.12.004

Menegon, L., Fusseis, F., Stünitz, H. & Xiao, X. 2015. Creep cavitation bands control porosity and fluid in lower crustal shear zones. *Geology*, **43**, 227-230. https://doi.org/10.1130/G36307.1

Neves, S.P. & Vauchez, A. 1995. Magma emplacement and shear zone nucleation and development in northeast Brazil (Fazenda Nova and Pernambuco shear zones; State of Pernambuco). *Journal of South American Earth Sciences,* **8**, 289-298. https://doi.org/10.1016/0895-9811(95)00014-7

Neves, S.P., Vauchez, A. & Archanjo, C.J. 1996. Shear zone-controlled magma emplacement or magma-assisted nucleation of shear zones? Insights from northeast Brazil. *Tectonophysics*, **262**, 349-364, https://doi.org/10.1016/0040-1951(96)00007-8

Neves, S.P. & Mariano, G. 1999. Assessing the tectonic significance of a large-scale transcurrent shear zone system: the Pernambuco lineament, northeastern Brazil. *Journal of Structural Geology*, **21**, 1369-1383, https://doi.org/10.1016/S0191-8141(99)00097-8

Neves, S.P., Vauchez, A. & Feraud, G. 2000. Tectono-thermal evolution, magma emplacement and shear zone development in the Caruaru area (Borborema Province, NE Brazil). *Precambrian Research*, **99**, 1-32, https://doi.org/10.1016/S0301-9268(99)00026-1

Neves., S.P. 2003. Proterozoic history of the Borborema Province (NE Brazil): correlations with neighboring cratons and Pan-African belts and implications for the evolution of western Gondwana. *Tectonics*, **22**, 1030, https://doi.org/10.1029/2001TC001352

Neves, S.P., Melo, S.C., Moura, C.A.V., Mariano, G. & Silva, J.M.R. 2004. Zircon Pb-Pb geochronology of the Caruaru Area, Northeastern Brazil: temporal constrains on the Proterozoic evolution of Borborema Province. *International Geology Review*, **46**, 52-63, https://doi.org/10.2747/0020-6814.46.1.52

Neves, S.P. 2011. Atlantica revisited: new data and thoughts on the formation and evolution of a long-lived continent. *International Geology Review*, **53**, 1377-1391, https://doi.org/10.1080/00206814.2010.527676

Neves, S.P., Bruguier, O., da Silva, J.M.R., Mariano, G., Silva Filho, A.F. & Teixeira, C.M.L. 2015. From extension to shortening: Dating the onset of the Brasiliano Orogeny in the Eastern Borborema Province. *Journal of South American Earth Sciences*, **58**, 238-256, http://dx.doi.org/10.1016/j.jsames.2014.06.004

Okudaira, T., Jeřábek, P., Stünitz, H. & Fusseis, F. 2015. High-temperature fracturing and subsequent grain-size-sensitive creep in lower crustal gabbros: Evidence for coseismic loading followed by creep during decay stress in the lower crust? *Journal of Geophysical Research: Solid Earth*, **120**, https://doi.org/10.1002/2014JB011708

Oliot, E., Goncalves, P. & Marquer, D. 2010. Role of plagioclase and reaction softening in a metagranite shear zone at mid-crustal conditions (Gotthard Massif, Swiss Central Alps). *Journal of Metamorphic Geology*, **28**, 849-871, https://doi.org/10.1111/j.1525-1314.2010.00897.x

Passchier, C.W. & Trouw, R.A.J. 2005. *Microtectonics*. 2nd edn. Springer, Berlin.

Phillips, E.R. 1980. On polygenetic myrmekite. *Geological Magazine*, **117**, 29-36, https://doi.org/10.1017/S0016756800033070

Platt., J.P. 2015. Rheology of two-phase systems: a microphysical and observational approach. *Journal of Structural Geology*, **77**, 213-227, http://dx.doi.org/10.1016/j.jsg.2015.05.003

Putirka, K.D. 2008. Thermometers and Barometers for Volcanic Systems. *Reviews in Mineralogy & Geochemistry*, **69**, 61-120, https://doi.org/10.2138/rmg.2008.69.1

Ribeiro, B.V., Faleiros, F.M., Campanha, G.A.C., Lagoeiro, L., Weinberg, R.F. & Hunter, N.J.R. 2019. Kinematics, nature of deformation and tectonic settings of the Taxaquara Shear Zone, a major transpressional zone of the Ribeira Belt (SE Brazil). *Tectonophysics*, **751**, 83-108, https://doi.org/10.1016/j.tecto.2018.12.025

Silva Filho, A.F., Guimarães, I.P. & Van Schmus, W.R. 2002. Crustal Evolution of the Pernambuco-Alagoas Complex, Borborema Province, NE Brazil: Nd. *Gondwana Research*, **5**, 409-422, https://doi.org/10.1016/S1342-937X(05)70732-2

Sibson, R.H. 1977. Fault rocks and fault mechanisms. *Journal of the Geological Society*, **133**, 191-213.

Simpson, C. & Wintsch, R.P. 1989. Evidence for deformation-induced K-feldspar replacement by myrmekite. *Journal of Metamorphic Geology*, **7**, 261-275, https://doi.org/10.1111/j.1525-1314.1989.tb00588.x

Stipp, M., Stünitz, H., Heilbronner, R. & Schmid, S.M. 2002*a*. The eastern Tonale fault zone: a 'natural laboratory' for crystal plastic deformation of quartz over a temperature range from 250 to 700°C. *Journal of Structural Geology*, **24**, 1861-1884, https://doi.org/10.1016/S0191-8141(02)00035-4

Stipp, M., Stünitz, H., Heilbronner, R. & Schmid, S.M. 2002*b*. Dynamic recrystallization of quartz: correlation between natural and experimental conditions. *Geological Society, London, Special Publications*, **200**, 171-190, https://doi.org/10.1144/GSL.SP.2001.200.01.11

Stipp, M. & Tullis, J. 2003. The recrystallized grain size piezometer for quartz. *Geophysical Research Letters*, **30**, 2088, https://doi.org/10.1029/2003GL018444

Stormer, J.C. 1975. A practical two-feldspar geothermometer. *American Mineralogist*, **60**, 667-674.

Tsurumi., J., Hosonuma, H. & Kanagawa, K. 2003. Strain localization due to a positive feedback of deformation and myrmekite-forming reaction in granite and aplite mylonite along the Hatagawa Shear Zone of NE Japan. *Journal of Structural Geology*, **25**, 557-574, https://doi.org/10.1016/S0191-8141(02)00048-2

Tullis, J. 2002. Deformation of granitic rocks: experimental studies and natural examples. In: Plastic deformation of minerals and rocks. *Review in Mineralogy and Geochemistry*, **51**, 51-95, https://doi.org/10.2138/gsrmg.51.1.51

Van Schmus, W.R., Oliveira, E.P. Silva Filho, A.F.D., Toteu, S.F., Penaye, J. & Guimarães, I.P. 2008. Proterozoic links between the Borborema Province, NE Brazil, and the Central African Fold Belt. *In*: Pankhurst, R.J., Trouw, R.A.J., Brito Neves, B.B., de Wit, M.J. (eds) *West Gondwana: Pre-Cenozoic Correlations Across the South Atlantic Region. Geological Society, London, Special Publications*, **294**, 69-99, http://dx.doi.org/10.1144/SP294.5

Vauchez, A. 1980. Ribbon texture and deformation mechanisms of quartz in a mylonitized granite of Great Kabylia (Algeria). *Tectonophysics*, **67**, 1-12, https://doi.org/10.1016/0040-1951(80)90160-2

Vauchez, A. & Egydio da Silva, M. 1992. Termination of a continental-scale strike-slip fault in partially melted crust: The West Pernambuco shear zone, northeast Brazil. *Geology,* **20**, 1007-1010, https://doi.org/10.1130/0091-7613(1992)020<1007:TOACSS>2.3.CO;2

Vauchez, A., Neves, S.P., Caby, R., Corsini, M., Egydio-Silva, M., Arthaud, M. & Amaro, V. 1995. The Borborema shear zone system, NE Brazil. *Journal of South American Earth Sciences*, **8**, 247-266, https://doi.org/10.1016/0895-9811(95)00012-5

Viegas, G., Menegon, L. & Archanjo, C. 2016. Brittle grain-size reduction of feldspar, phase mixing and strain localization in granitoids at mid-crustal conditions (Pernambuco shear zone, NE Brazil). *Solid Earth*, **7**, 375-396, https://doi.org/10.5194/se-7-375-2016

Weinberg, R.F., Sial, A.N. & Mariano, G. 2004. Close spatial relationship between plutons and shear zones. *Geology*, **32**, 377-380, https://doi.org/10.1130/0091-7613-33.1.e72

White, R.W., Powell, R., Holland, T.J.B. & Worley, B.A. 2000. The effect of TiO_2 and Fe_2O_3 on metapelitic assemblages at greenschist and amphibolite facies conditions: mineral equilibria calculations in the system K_2O-FeO-MgO-Al_2O_3-SiO_2-H_2O-TiO_2-Fe_2O_3. *Journal of Metamorphic Geology*, **18**, 497-511, https://doi.org/10.1046/j.1525-1314.2000.00269.x

White, R.W., Powell, R. & Holland, T.J.B. 2001. Calculation of partial melting equilibria in the system Na_2O-CaO-K_2O-FeO-MgO-Al_2O_3-SiO_2-H_2O (NCKFMASH). *Journal of Metamorphic Geology*, **19**, 139-153, https://doi.org/10.1046/j.0263-4929.2000.00303.x

White, R.W., Powell, R. & Clarke, G.L. 2002. The interpretation of reaction textures in Fe-rich metapelitic granulites of the Musgrave Block, central Australia: constraints from mineral equilibria

calculations in the system K$_2$O-FeO-MgO- Al$_2$O$_3$-SiO$_2$-H$_2$O-TiO$_2$-Fe$_2$O$_3$. *Journal of Metamorphic Geology, 20, 41-55,* https://doi.org/10.1046/j.0263-4929.2001.00349.x

White, R.W., Powell, R. & Johnson, T.E. 2014. The effect of Mn on mineral stability in metapelites revisited: new *a-x* relations for manganese-bearing minerals. *Journal of Metamorphic Petrology*, **32**, 809-822, https://doi.org/10.1111/jmg.12095

Yardley, B.W.D., Rhede, D. & Heinrich, W. 2014. Rates of retrograde metamorphism and their implications for the rheology of the crust: an experimental study. *Journal of Petrology*, **55**, 623-641, https://doi.org/10.1093/petrology/egu001

5.   CONCLUSÕES

Essa pesquisa teve como objetivo caracterizar os mecanismos de deformação e as condições metamórficas ativas durante a história deformacional da zona de cisalhamento Pernambuco Leste. Compondo o trabalho foi realizada cartografia de campo da ZCPE, caracterização microestrutural das estruturas deformacionais ao longo do espectro rúptil-dúctil, análises de orientação preferencial cristalográfica, determinação da composição química de rocha total e de química mineral, geotermometria de dois feldspatos e modelamento termodinâmico das condições de milonitização na presença de fluidos.

As principais conclusões podem ser sumarizadas nos tópicos a seguir.

5.1.   Caracterização estrutural

A combinação entre mapeamento estrutural e análise microestrutural quantitativa possibilitou a definição de dois domínios distintos em termos de evolução deformacional. Na porção oeste da ZCPE, o domínio Caruaru é caracterizado por granitos miloníticos grossos lateralmente homogêneos que apresentam porfiroclastos de feldspato invariavelmente fraturados dando origem a fragmentos, além de fitas de quartzo cercadas por uma matriz fina composta por feldspatos e biotita em proporções variadas. Adicionalmente, os grãos de K-feldspato exibem intercrescimentos mirmequíticos localizados em quadrantes compresionais. K-feldspato e plagioclásio apresentam grãos finos na matriz, possuindo teores de Or e An diferentes dos porfiroclastos, sugerindo processos de reequilíbrio químico na presença de fluidos. O quartzo é encontrado essencialmente em fitas onde grãos individuais são alongados e recristalizados por rotação de subgrãos.

A análise de OPCs em agregados recristalizados de quartzo indica a ativação de fluência de deslocações acomodada por deslizamento ao longo do plano prismático <a>, além de atividade localizada dos sistemas romboédricos <a+c>. Na matriz, os grãos de K-feldspato, plagioclásio e biotita (<20 µm) estão associados a raros grãos de quartzo e envolvem os porfiroclastos formando uma trama anastomosada.

A caracterização microestrutural do quartzo indica recristalização por rotação de subgrãos. Este mecanismo, combinado com a acomodação de fluência de deslocações

pelo sistema prismático <a>, implica em temperaturas deformacionais em torno de 390 e 530° (Stipp et al., 2002*a*).

O domínio Gravatá, localizado na porção oriental/leste da ZCPE, é composto por milonitos e ultramilonitos que registram transições abruptas entre as intensidades deformacionais. Os ultramilonitos apresentam segregação de bandas félsicas marcadas pela presença de porfiroclastos de K-feldspato e plagioclásio fraturados, imersos em uma matriz feldspática fina. As bandas máficas são dominadas por biotita + epidoto, além de alguns grãos de óxidos como titanita e hematita. O K-feldspato apresenta grão finos em forma de gotas caracterizando a ativação do mecanismo de dissolução-precipitação.

As fitas de quartzo se apresentam como bandas onde os grãos são equigranulares e recristalizados por rotação de subgrãos, com raros porfiroclastos alongados que apresentam protuberâncias em suas extremidades (*bulging*), indicando que a recristalização do quartzo ocorreu no limiar da transição entre *bulging* e rotação de subgrãos (~ 480-500ºC, Stipp et al. 2002*a*). A análise de OPCs em quartzo indica que a fluência de deslocações é acomodada por ativação do sistema basal <a> e rômbico <a+c>. As microestruturas do quartzo implicam em recristalização por rotação de subgrãos. A combinação deste mecanismo com o deslizamento intracristalino ao longo do sistema basal <a> implicam em temperaturas entre 390 e 530°C (Stipp et al., 2002*a*).

As características apresentadas em ambos os domínios da ZCPE revelam uma ativação combinada de mecanismos rúpteis e dúcteis durante a localização da deformação na ZCPE. Os processos de recristalização dinâmica são acomodados nos agregados recristalizados de quartzo, enquanto fraturamento e deformação rúptil ocorrem de forma heterogênea nos grãos de feldspato, os quais constituem a fase reologicamente mais resistente. Adicionalmente, a presença de fluidos favorece a localização da deformação por meio de reações de desequilíbrio metamórfico, as quais resultam na formação de misturas poliminerálicas finas derivadas de mecanismos de dissolução-precipitação assistidos por fluidos.

Estas evidências indicam que a ZCPE teve sua história de deformação em condições típicas da transição rúptil-dúctil, em profundidades equivalentes à crosta intermediária-superior (~ 12-15 km).

5.2. Condições de pressão e temperatura durante a deformação

As estimativas geotermobarométricas prévias (Neves e Mariano, 1999; Neves et al., 2000; Viegas et al., 2016) indicam que a ZCPE foi deformada em temperaturas de 500-550°C no domínio Caruaru e em temperaturas entre 400 e 480°C no domínio Gravatá (Neves e Mariano, 1999). O presente estudo apresenta um refinamento das condições de P-T usando como base o modelamento termodinâmico das condições de equilíbrio das assembleias minerais durante milonitização.

No domínio Caruaru, a geotermometria de dois feldspatos realizada na matriz recristalizada fornece temperaturas de 483 ± 44°C. A pseudoseção do domínio Caruaru considerou a assembleia mineral estável composta por: Kfs + Qz + Pl + Bi + Ilm + Sph + Ep para definir o campo de estabilidade nas condições de P-T. Maiores restrições no campo de estabilidade da assembleia foram obtidas por meio das isopletas de teor de anortita em plagioclásio e composição modal de ilmenita e epidoto. Logo, as condições de P-T durante a deformação registradas para o domínio Caruaru foram limitadas a 526 ± 9°C e 4,75 ± 0,25 kbar.

No domínio Gravatá, o geotermômetro de dois feldspatos foi aplicado em grãos recristalizados no interior das fraturas intracristalinas, fornecendo estimativas em torno de 416 ± 44°C. A pseudoseção do domínio Gravatá considerou a assembleia mineral estável composta por Qz + Kfs + Pl + Bi + Ep + Hem + Ttn + Grt, para definir o campo de estabilidade nas condições de P-T. O aprimoramento desse resultado se deu por meio de isopletas do teor de anortita em plagioclásio e da composição modal de titanita e granada. Assim, o domínio Gravatá registrou condições de P-T durante a deformação limita a 437 ± 17°C e 5,9 ± 1 kbar.

O banco de dados obtido nessa pesquisa permite concluir que a ZCPE possui distintos picos metamórficos ao longo de sua extensão. Foram atingidas condições de P-T equivalentes à fácies xisto verde superior e inferior, sendo ambas características de deformação ao longo da transição rúptil-dúctil. Ademais, não foi encontrado nenhuma evidência de retrometamorfismo ao longo de toda a estrutura; a variação metamórfica do espectro da fácies xisto verde superior e média/inferior se dá de forma descontínua ao longo da continuidade lateral da estrutura. Estas evidências indicam que os diferentes picos deformacionais observados nos domínios Caruaru e Gravatá resultam de níveis de

exposição distintos da estrutura, os quais estão possivelmente associados à uma trajetória de exumação heterogênea da ZCPE ao longo de sua história evolutiva.

5.3. Implicações Tectônicas

A estruturação geotectônica da Província Borborema é idealizada com base em distintos modelos evolutivos. No modelo de evolução alóctone, existe uma aglutinação entre terrenos de origem diferenciada (Coney, et al.,1980). Esse processo teria ocorrido durante o evento Cariris Velhos (Santos, et al., 2010) e a orogênese brasiliana (Brito Neves, et al., 2000; Santos, 2018). No modelo intracontinental (Neves, 2003; 2011), um único bloco permaneceu relativamente estável desde o paleoproterozoico (2,2 – 2,0 Ga) sendo afetado por processos de rifteamento e magmatismo intracontinental com formação de bacias e proto-oceanos ao longo da sua evolução proterozoica (Neves, 2015).

A ZCPE é uma estrutura de importante relevância no debate da evolução geotectônica da Província Borborema (Brito Neves, 2000; Neves, 2003, 2011). Sua posição geográfica separando domínios de supostas evoluções tectonoestratigráficas distintas e sua continuidade no continente africano (Caxito et al., 2020) são fatores regionais de importante relevância. Nesse trabalho, a caracterização da ZCPE contribui para os modelos de evolução com a identificação de distintos domínios e suas respectivas condições de pressão e temperatura.

O domínio Caruaru é caracterizado por deformação em fácies xisto verde superior composto por granitos miloníticos de trama anastomosada. O domínio Gravatá foi deformado em condições de fácies xisto verde inferior, caracterizado pela localização da deformação em bandas ultramiloníticas que transitam abruptamente para rochas não deformadas. Essas características deformacionais da ZCPE indicam uma história deformacional em profundidades equivalente à transição rúptil-dúctil, as quais são tipicamente marcadas pela coatividade de mecanismos rúpteis e dúcteis ao longo do referido nível crustal (e.g. Handy et al., 2007).

No contexto da orogênese brasiliana, o batólito Caruaru-Arcoverde (591-583 Ma; Guimarães et al., 2004) e a suíte intrusiva Itaporanga (584 ± 2 Ma; Brito Neves et al., 2003) são classificados como granitos pós-colisionais que acomodaram a deformação imposta pela ZCPE no estado sólido (Neves et al., 1996; Van Schmus et al., 2011).

Adicionalmente, a idade do início da deformação na ZCPE foi datada em 591 ± 4 Ma a partir do método U-Pb em grãos de monazita (França et al., 2019).

Os resultados obtidos nessa pesquisa permitem concluir que a ZCPE é uma estrutura deformada condições rúpteis-dúcteis em profundidades equivalentes à crosta intermediária - superior, onde existe a atuação combinada de mecanismos de deformação rúpteis e dúcteis promovendo uma localização heterogênea da deformação. Adicionalmente, a variação lateral do gradiente metamórfico ao longo da estrutura e a heterogeneidade dos processos de localização da deformação, resultando em marcadas variações no tamanho do grão deformado/recristalizado nos granitos miloníticos estudados, indicam que a acomodação da deformação ao longo da ZCPE se deu de forma descontínua, possivelmente associada com os processos de exumação da estrutura durante o neoproterozoico.

6.   REFERÊNCIAS

Almeida, F.F.M., Hasui, Y., Brito Neves, B.B., Fuck, R.A. **1981**. Brazilian structural provinces: an introduction. Earth-Science Reviews 17, 1-29.

Alsop, G.I. e Holdsworth, R.E. 2004. Shear zones – an introduction and overview. Em: Alsop, G.I., Holdsworth, R.E., Mccaffrey, K.J.W., Hand, M. (eds.). Flow Processes in Faults and Shear Zones. Geological Society of London Special Publications 224, 1-9. https://doi.org/10.1144/GSL.SP.2004.224.01.01

Brito Neves, B.B., Passarelli, C.R., Basei, M.A.S., Santos, E.J. 2003. Idades U-Pb em zircão de alguns granitos clássicos da Província Borborema. Geologia USP Série Científica 3, 25-38.

Buhrke, V.E., Jenkins, R., Smith, D.K. 1997. A practical guide for the preparation of specimens for X-ray Fluorescence and X-ray diffraction analysis. New York, Wiley-VCH, 360 p.

Caxito, F.A., Santos, L.C.M.L., Ganade, C.E., Bendaoud, A., Fettous, E., Bouyo, M.H. 2020. Toward an integrated model of geological Evolution for NE Brazil-NW Africa: the Borborema Province and its connections to the Trans-Saharan (Benino-Nigerian and Tuareg shields) and Central African orogens. Brazilian Journal of Geology 50, e20190122. https://doi.org/10.1590/2317-4889202020190122

Ebert, H. 1964. Tectônica e metamorfismo regional do Escudo Brasileiro. SUDENE, Divisão de Geologia.

Goldstein, J.I., Newburry, D.E., Joy, D.C., Lyman, C.E., Echlin, P., Lifshin, E., Sawyer, L., Michael, J.R. 2003. Scanning Electron Microscopy and X-Ray Microanalysis. New York, Kluwer Academic/Plenum Publisher, 689 p.

Jardim de Sá, E.F., Medeiros, V.C., Amaro, V.E. 1995. Os cisalhamentos brasilianos na Zona Transversal, NE do Brasil: uma mega-estrutura em dominó. Atas do 168° Simpósio de Geologia do Nordeste, 134–138.

Jenkins, R. 1999. X-ray Fluorescence Spectrometry. New York, John Wiley & Sons, 207 p.

Karato S. 2008. Deformation of Earth Materials. New York, Cambridge University Press, 463 p.

Melo, E.Z.V. 1977. O sistema de falhas transcorrentes do nordeste brasileiro. Boletim de Mineralogia 5, 95-106.

Mitra G. 1979. Ductile deformation zones in Blue Ridge basement rocks and estimation of finite strains. Geological Society of America Bulletin 90, 935-951. https://doi.org/10.1130/0016-7606(1979)90<935:DDZIBR>2.0.CO;2

Morales, L.F.G., Hinrichs, R., Fernandes, L.A.D. 2007. A técnica de Difração de Elétrons Retro-Espalhados (EBSD) em Microscópio Eletrônico de Varredura (MEV) e sua aplicação no estudo de rochas deformadas. Revista Pesquisas em Geociências 34, 19-34.

Neves, S.P. **2015**. Constraints from zircon geochronology on the tectonic evolution of the Borborema Province (NE Brazil): Widespread intracontinental Neoproterozoic reworking of a Paleoproterozoic

accretionary orogen. Journal of South American Earth Sciences 58, 150-164. https://doi.org/10.1016/j.jsames.2014.08.004

Prior, D.J., Boyle, A.P., Brenker, F., Cheadle, M.C., Day, A., Lopez, G., Peruzzo, L., Potts, G.J., Reddy, S., Spiess, R., Timms, N.E., Trimby, P., Wheeler, J., Zetterstromüm, L. 1999. The application of electron backscatter diffraction and orientation contrast imaging in the SEM to textural problems in rocks. American Mineralogist 84, 1741-1759.

Randle, V. e Caul, M. 1996. Representation of electron backscatter diffraction data. Materials Science and Technology 12, 844-850. https://doi.org/10.1179/mst.1996.12.10.844

Santos, E.J., Van Schmus, W.R., Kozuch, M., Brito Neves, B.B. 2010. The Cariris Velhos tectonic event in northeast Brazil. Journal of South American Earth Sciences 29, 61-76. https://doi.org/10.1016/j.jsames.2009.07.003

Santos, L.C.M.L., Dantas, E.L., Cawood, P.A., Lages, G., Lima, H.M., Santos, E.J. 2018. Accretion tectonics in the Borborema Province, NE Brazil. Tectonics 37, 2727-2743. https://doi.org/10.1029/2018TC005130

Scholz, C.H. 2002. The Mechanics of Earthquakes and Faulting. New York, Cambridge University Press, 467 p.

Van Schmus, W.R., Kozuch, M., Brito Neves, B.B. **2011**. Precambrian history of the Zona Transversal of the Borborema Province, NE Brazil: insights from Sm-Nd and U-Pb geochronology. Journal of South American Earth Science 31, 227–252. https://doi.org/10.1016/j.jsames.2011.02.010

Wenk, H.R. e Christie, J.M. 1991. Comments on the interpretation of deformation textures in rocks. Journal of Structural Geology 13, 1091-1110. https://doi.org/10.1016/0191-8141(91)90071-P

7.   ANEXOS

Anexo I

Análises geoquímicas de K-feldspato e plagioclásio no domínio Caruaru.

Matrix - Plagioclase	1		2		3		4		5		6		7		8		9		10	
	Core	Rim	Core	Rim	Core	Rim	Core	Rim	Core	Rim	Core	Rim	Core	Rim	Core	Rim	Core	Rim	Core	Rim
SiO2	59.95	60.90	60.04	59.66	68.20	57.10	56.97	57.37	57.49	56.88	55.91	56.40	60.54	62.43	60.06	61.29	60.62	62.94	63.99	60.33
TiO2	0.09	0.00	0.02	0.03	0.02	0.00	0.00	0.00	0.04	0.00	0.09	0.00	0.00	0.14	0.00	0.00	0.00	0.00	0.09	0.00
Al2O3	22.27	22.86	21.79	22.36	13.01	19.18	19.43	19.32	19.55	19.26	19.29	19.29	22.42	21.52	23.63	23.18	22.86	21.85	20.47	23.03
Cr2O3	0.07	0.02	0.00	0.01	0.00	0.00	0.09	0.00	0.00	0.00	0.13	0.00	0.00	0.00	0.00	0.07	0.04	0.07	0.00	0.00
FeO$_{Tot}$	0.03	0.04	0.08	0.07	0.03	0.05	0.08	0.03	0.00	0.09	0.06	0.05	0.03	0.51	0.23	0.23	0.08	0.00	0.09	0.03
MnO	0.00	0.02	0.00	0.00	0.02	0.00	0.00	0.08	0.07	0.03	0.11	0.02	0.02	0.02	0.00	0.05	0.01	0.07	0.02	0.01
MgO	0.00	0.00	0.01	0.00	0.01	0.00	0.00	0.00	0.00	0.00	0.00	0.00	0.00	0.04	0.00	0.03	0.00	0.02	0.02	0.00
CaO	4.75	4.64	4.30	4.68	3.30	4.54	4.78	4.65	5.05	4.81	4.80	4.85	4.37	3.89	5.53	5.02	4.70	3.98	3.78	5.03
Na2O	8.34	8.68	8.05	8.57	6.37	9.41	9.43	9.53	9.03	9.21	9.48	8.28	8.76	8.54	8.35	8.33	8.66	8.48	8.15	8.30
K2O	0.18	0.15	1.54	0.44	0.18	0.39	0.18	0.15	0.69	0.32	0.28	1.31	0.14	0.34	0.21	0.17	0.10	0.44	0.24	0.10
Total	95.72	97.36	95.84	95.84	91.12	90.72	91.03	91.19	91.96	90.59	90.23	90.24	96.27	97.44	98.01	98.37	97.07	97.88	96.91	96.85
Si	2.78	2.77	2.78	2.76	3.42	2.76	2.75	2.76	2.75	2.76	2.72	2.76	2.78	2.85	2.72	2.77	2.77	2.86	2.95	2.76
Ti	0.00	0.00	0.00	0.00	0.00	0.00	0.00	0.00	0.00	0.00	0.00	0.00	0.00	0.00	0.00	0.00	0.00	0.00	0.00	0.00
Al	1.22	1.23	1.19	1.22	0.77	1.09	1.10	1.10	1.10	1.10	1.11	1.11	1.21	1.16	1.26	1.23	1.23	1.17	1.11	1.24
Cr	0.00	0.00	0.00	0.00	0.00	0.00	0.00	0.00	0.00	0.00	0.01	0.00	0.00	0.00	0.00	0.00	0.00	0.00	0.00	0.00
Fe2	0.00	0.00	0.00	0.00	0.00	0.00	0.00	0.00	0.00	0.00	0.00	0.00	0.00	0.02	0.00	0.01	0.00	0.00	0.00	0.00
Mn	0.00	0.00	0.00	0.00	0.00	0.00	0.00	0.00	0.00	0.00	0.00	0.00	0.00	0.00	0.00	0.00	0.00	0.00	0.00	0.00
Mg	0.00	0.00	0.00	0.00	0.00	0.00	0.00	0.00	0.00	0.00	0.00	0.00	0.00	0.00	0.00	0.00	0.00	0.00	0.00	0.00
Ca	0.24	0.23	0.21	0.23	0.18	0.24	0.25	0.24	0.26	0.25	0.25	0.25	0.22	0.19	0.27	0.24	0.23	0.19	0.19	0.25
Na	0.75	0.77	0.72	0.77	0.62	0.88	0.88	0.89	0.84	0.87	0.89	0.79	0.78	0.76	0.73	0.73	0.77	0.75	0.73	0.74
K	0.01	0.01	0.09	0.03	0.01	0.02	0.01	0.01	0.04	0.02	0.02	0.08	0.01	0.02	0.01	0.01	0.01	0.03	0.01	0.01
An	23.66	22.61	20.78	22.61	22.03	20.62	21.64	21.06	22.73	21.99	21.53	22.66	21.45	19.67	26.47	24.71	22.94	20.03	20.09	24.95
Ab	75.25	76.52	70.33	74.88	76.87	77.27	77.37	78.14	73.56	76.27	76.98	70.04	77.72	78.29	72.35	74.29	76.48	77.30	78.38	74.45
Or	1.08	0.85	8.87	2.50	1.08	2.09	0.97	0.78	3.69	1.72	1.48	7.28	0.82	2.03	1.16	0.98	0.56	2.65	1.52	0.58

Matrix - K-feldspar	1		2		3		4		5		6		7		8		9		10		11	
	Core	Rim	Core	Rim	Core	Rim	Core	Rim	Core	Rim	Core	Rim	Core	Rim	Core	Rim	Core	Rim	Core	Rim	Core	Rim
SiO2	61.41	63.57	62.44	61.25	61.88	60.55	61.27	61.94	60.40	58.30	59.55	58.78	62.88	65.97	58.94	57.82	57.43	56.73	48.17	42.62	62.81	62.83
TiO2	0.00	0.00	0.13	0.08	0.00	0.05	0.00	0.00	0.09	0.11	0.13	0.00	0.00	0.00	0.05	0.00	0.00	0.00	0.19	0.53	0.21	0.00
Al2O3	18.53	18.10	18.30	17.93	17.48	18.33	17.29	19.19	16.26	16.68	15.48	15.60	18.67	12.51	15.17	16.09	16.54	18.00	17.62	17.97	18.55	18.59
Cr2O3	0.01	0.00	0.06	0.09	0.00	0.05	0.00	0.00	0.00	0.00	0.00	0.00	0.07	0.00	0.10	0.00	0.00	0.00	0.00	0.00	0.07	0.01
FeO$_{Tot}$	0.03	0.00	0.06	0.06	0.03	0.02	0.01	0.02	0.11	0.12	0.01	0.02	0.00	0.00	0.00	0.05	0.04	0.07	10.74	15.30	0.06	0.00
MnO	0.06	0.01	0.03	0.04	0.00	0.03	0.00	0.05	0.01	0.00	0.00	0.03	0.00	0.00	0.01	0.00	0.00	0.01	0.12	0.16	0.00	0.00
MgO	0.00	0.00	0.02	0.00	0.00	0.00	0.00	0.00	0.01	0.00	0.02	0.00	0.00	0.00	0.01	0.00	0.00	0.00	4.42	6.37	0.00	0.00
CaO	0.09	0.15	0.18	0.03	0.07	0.62	0.00	1.32	0.64	1.85	0.24	0.53	0.67	0.19	0.15	1.07	1.88	3.46	0.07	0.14	1.33	1.18
Na2O	0.67	2.94	1.55	0.59	1.04	2.02	0.76	5.20	2.82	3.69	4.52	2.28	2.83	2.37	1.94	3.51	3.73	6.34	0.70	0.41	2.59	3.20
K2O	15.16	12.60	13.92	15.41	14.71	11.47	15.23	8.25	12.37	9.68	10.66	12.82	12.70	10.05	13.45	11.10	10.36	5.53	12.24	10.48	11.25	8.99
Total	95.95	97.42	96.78	95.46	95.20	93.22	94.57	96.05	92.76	90.44	90.71	90.09	97.84	91.17	89.88	89.73	90.01	90.15	94.66	94.47	96.87	94.85
Si	2.95	2.98	2.97	2.96	2.99	2.98	2.99	2.90	2.97	2.93	2.96	2.98	2.93	3.35	3.01	2.92	2.89	2.81	2.37	2.11	2.97	3.03
Ti	0.00	0.00	0.00	0.00	0.00	0.00	0.00	0.00	0.00	0.00	0.00	0.00	0.00	0.00	0.00	0.00	0.00	0.00	0.01	0.02	0.01	0.00
Al	1.05	1.00	1.03	1.02	1.00	1.06	0.99	1.06	0.94	0.99	0.91	0.93	1.02	0.75	0.91	0.96	0.98	1.05	1.02	1.05	1.03	1.06
Cr	0.00	0.00	0.00	0.00	0.00	0.00	0.00	0.00	0.00	0.00	0.00	0.00	0.00	0.00	0.00	0.00	0.00	0.00	0.00	0.00	0.00	0.00
Fe2	0.00	0.00	0.00	0.00	0.00	0.00	0.00	0.00	0.00	0.00	0.00	0.00	0.00	0.00	0.00	0.00	0.00	0.00	0.00	0.00	0.00	0.00
Mn	0.00	0.00	0.00	0.00	0.00	0.00	0.00	0.00	0.00	0.00	0.00	0.00	0.00	0.00	0.00	0.00	0.00	0.00	0.01	0.01	0.00	0.00
Mg	0.00	0.00	0.00	0.00	0.00	0.00	0.00	0.00	0.00	0.00	0.00	0.00	0.00	0.00	0.00	0.00	0.00	0.00	0.32	0.47	0.00	0.00
Ca	0.00	0.01	0.01	0.00	0.00	0.03	0.00	0.07	0.03	0.10	0.01	0.03	0.03	0.01	0.01	0.06	0.10	0.18	0.00	0.01	0.07	0.06
Na	0.06	0.27	0.14	0.06	0.10	0.19	0.07	0.47	0.27	0.36	0.44	0.22	0.26	0.23	0.19	0.34	0.36	0.61	0.07	0.04	0.24	0.30
K	0.93	0.75	0.84	0.95	0.91	0.72	0.95	0.49	0.78	0.62	0.68	0.83	0.75	0.65	0.88	0.72	0.66	0.35	0.77	0.66	0.66	0.59
An	0.45	0.71	0.89	0.17	0.35	3.45	0.00	6.42	3.12	9.21	1.11	2.67	3.20	1.16	0.77	5.16	10.07	8.98	0.45	1.04	6.83	6.66
Ab	6.22	25.98	14.33	5.47	9.65	20.41	7.02	45.76	24.89	33.29	38.73	20.71	24.47	26.05	17.82	30.75	39.49	32.21	7.98	5.50	24.14	32.74
Or	93.32	73.29	84.76	94.35	89.98	76.13	92.97	47.80	71.98	57.48	60.15	76.60	72.31	72.78	81.39	64.07	50.48	58.80	91.56	93.45	69.01	60.59

Clast - Plagioclase	1	2	3	4	5	6
SiO_2	62.40	61.73	61.26	60.89	61.18	61.38
TiO_2	0.03	0.05	0.05	0.00	0.21	0.09
Al_2O_3	23.84	23.90	23.63	23.78	23.71	23.50
Cr_2O_3	0.00	0.00	0.00	0.00	0.00	0.01
FeO_{Tot}	0.23	0.20	0.22	0.09	0.13	0.17
MnO	0.00	0.02	0.04	0.04	0.01	0.07
MgO	0.00	0.00	0.00	0.00	0.00	0.00
CaO	5.16	5.23	5.28	5.36	5.32	5.24
Na_2O	8.53	8.16	8.36	8.14	8.23	8.26
K_2O	0.19	0.17	0.18	0.23	0.10	0.11
Total	100.41	99.46	99.09	98.60	98.94	98.89
Si	2.76	2.76	2.75	2.75	2.75	2.76
Ti	0.00	0.00	0.00	0.00	0.01	0.00
Al	1.24	1.26	1.25	1.26	1.26	1.25
Cr	0.00	0.00	0.00	0.00	0.00	0.00
Fe2	0.01	0.01	0.01	0.00	0.00	0.01
Mn	0.00	0.00	0.00	0.00	0.00	0.00
Mg	0.00	0.00	0.00	0.00	0.00	0.00
Ca	0.24	0.25	0.25	0.26	0.26	0.25
Na	0.73	0.71	0.73	0.71	0.72	0.72
K	0.01	0.01	0.01	0.01	0.01	0.01
An	24.79	25.88	25.61	26.33	26.16	25.75
Ab	74.11	73.13	73.37	72.35	73.25	73.58
Or	1.09	0.97	1.01	1.31	0.57	0.66

Clast - K-feldspar	1	2	3	4	5	6	7	8	9	10
SiO_2	63.62	63.40	63.50	63.76	63.75	64.17	63.44	63.04	62.86	63.83
TiO_2	0.00	0.05	0.00	0.01	0.00	0.06	0.12	0.02	0.18	0.00
Al_2O_3	18.09	18.27	18.24	17.96	18.19	18.08	18.11	18.17	18.19	18.45
Cr_2O_3	0.00	0.10	0.10	0.06	0.00	0.00	0.00	0.04	0.02	0.00
FeO_{Tot}	0.00	0.04	0.07	0.00	0.09	0.05	0.05	0.06	0.03	0.04
MnO	0.01	0.00	0.03	0.00	0.17	0.00	0.12	0.02	0.00	0.00
MgO	0.00	0.01	0.00	0.00	0.03	0.00	0.00	0.00	0.00	0.01
CaO	0.02	0.00	0.03	0.03	0.01	0.03	0.00	0.05	0.02	0.03
Na_2O	0.58	0.59	0.99	0.45	0.42	0.65	0.43	0.63	1.03	0.98
K_2O	15.46	15.27	14.96	15.68	15.49	15.81	15.89	15.41	14.50	14.91
Total	97.76	97.72	97.92	97.95	98.14	98.86	98.16	97.42	96.82	98.25
Si	3.01	3.00	2.99	3.01	3.01	3.00	2.99	2.99	2.99	2.99
Ti	0.00	0.00	0.00	0.00	0.00	0.00	0.00	0.00	0.01	0.00
Al	1.01	1.02	1.01	1.00	1.01	1.00	1.01	1.01	1.02	1.02
Cr	0.00	0.00	0.00	0.00	0.00	0.00	0.00	0.00	0.00	0.00
Mn	0.00	0.00	0.00	0.00	0.01	0.00	0.00	0.00	0.00	0.00
Mg	0.00	0.00	0.00	0.00	0.00	0.00	0.00	0.00	0.00	0.00
Ca	0.00	0.00	0.00	0.00	0.00	0.00	0.00	0.00	0.00	0.00
Na	0.05	0.05	0.09	0.04	0.04	0.06	0.04	0.06	0.09	0.09
An	0.08	0.00	0.14	0.16	0.03	0.16	0.00	0.23	0.08	0.13
Ab	5.35	5.53	9.15	4.14	3.96	5.84	3.93	5.79	9.72	9.02
Or	94.55	94.46	90.70	95.68	95.99	93.98	96.06	93.79	90.19	90.84

Fracture - Plagioclase	1		2		3		4		5		6		7		8		9		10	
	Core	Rim	Core	Rim	Core	Rim	Core	Rim	Core	Rim	Core	Rim	Core	Rim	Core	Rim	Core	Rim	Core	Rim
SiO2	67.77	67.80	67.62	67.37	67.66	67.41	67.56	67.46	66.37	67.08	67.29	67.88	67.42	67.65	67.10	67.15	67.28	67.44	67.06	67.86
TiO2	0.18	0.00	0.05	0.01	0.00	0.00	0.00	0.40	0.05	0.00	0.00	0.01	0.00	0.00	0.00	0.00	0.04	0.00	0.00	0.04
Al2O3	18.55	18.52	18.58	18.32	18.19	18.56	18.56	18.11	18.39	18.33	17.99	18.13	18.18	18.20	17.94	18.04	18.26	17.99	18.01	18.07
Cr2O3	0.00	0.00	0.00	0.03	0.03	0.02	0.04	0.00	0.00	0.01	0.00	0.00	0.00	0.00	0.00	0.04	0.02	0.02	0.00	0.00
FeO$_{Tot}$	0.03	0.00	0.01	0.07	0.02	0.08	0.04	0.04	0.06	0.03	0.05	0.03	0.02	0.13	0.05	0.00	0.00	0.00	0.05	0.03
MnO	0.00	0.07	0.00	0.00	0.03	0.00	0.02	0.03	0.02	0.05	0.00	0.02	0.01	0.04	0.00	0.00	0.00	0.00	0.00	0.00
MgO	0.00	0.00	0.00	0.00	0.00	0.00	0.00	0.00	0.00	0.00	0.00	0.00	0.00	0.00	0.00	0.00	0.00	0.00	0.00	0.00
CaO	0.24	0.16	0.13	0.21	0.32	0.40	0.22	0.34	0.58	0.42	0.32	0.32	0.34	0.30	0.34	0.46	0.23	0.18	0.26	0.28
Na2O	10.72	10.89	11.02	10.78	10.74	10.99	11.19	9.81	11.00	10.54	11.12	11.04	10.86	10.82	10.62	11.16	10.76	10.93	10.64	10.53
K2O	0.29	0.17	0.10	0.15	0.10	0.12	0.13	0.62	0.14	0.51	0.10	0.11	0.16	0.09	0.10	0.07	0.09	0.09	0.06	0.07
Total	97.82	97.68	97.54	96.99	97.19	97.59	97.77	96.90	96.65	97.09	96.89	97.57	97.05	97.24	96.15	96.95	96.71	96.74	96.10	96.91
Ti	0.01	0.00	0.00	0.00	0.00	0.00	0.00	0.01	0.00	0.00	0.00	0.00	0.00	0.00	0.00	0.00	0.00	0.00	0.00	0.00
Al	0.98	0.98	0.98	0.98	0.97	0.98	0.98	0.98	0.98	0.98	0.96	0.96	0.97	0.97	0.97	0.96	0.98	0.96	0.97	0.97
Cr	0.00	0.00	0.00	0.00	0.00	0.00	0.00	0.00	0.00	0.00	0.00	0.00	0.00	0.00	0.00	0.00	0.00	0.00	0.00	0.00
Fe2	0.00	0.00	0.00	0.00	0.00	0.00	0.00	0.00	0.00	0.00	0.00	0.00	0.00	0.00	0.00	0.00	0.00	0.00	0.00	0.00
Mn	0.00	0.00	0.00	0.00	0.00	0.00	0.00	0.00	0.00	0.00	0.00	0.00	0.00	0.00	0.00	0.00	0.00	0.00	0.00	0.00
Mg	0.00	0.00	0.00	0.00	0.00	0.00	0.00	0.00	0.00	0.00	0.00	0.00	0.00	0.00	0.00	0.00	0.00	0.00	0.00	0.00
Ca	0.01	0.01	0.01	0.01	0.02	0.02	0.01	0.02	0.03	0.02	0.02	0.02	0.02	0.01	0.02	0.02	0.01	0.01	0.01	0.01
Na	0.93	0.95	0.96	0.95	0.94	0.96	0.97	0.87	0.97	0.93	0.97	0.96	0.95	0.95	0.94	0.98	0.95	0.96	0.94	0.93
K	0.02	0.01	0.01	0.01	0.01	0.01	0.01	0.04	0.01	0.03	0.01	0.01	0.01	0.01	0.01	0.00	0.01	0.00	0.00	0.00
An	1.22	0.78	0.63	1.04	1.62	1.96	1.05	1.80	2.79	2.08	1.57	1.56	1.69	1.48	1.74	2.21	1.14	0.88	1.30	1.46
Ab	97.04	98.20	98.81	98.10	97.75	97.36	98.18	94.31	96.43	94.88	97.86	97.82	97.40	97.97	97.66	97.42	98.29	98.62	98.31	98.14
Or	1.73	1.01	0.56	0.87	0.62	0.68	0.76	3.90	0.78	3.04	0.57	0.62	0.91	0.55	0.60	0.37	0.56	0.50	0.39	0.40

Fracture - K-feldspar	1		2		3		4		5		6		7		8		9		10	
	Core	Rim	Core	Rim	Core	Rim	Core	Rim	Core	Rim	Core	Rim	Core	Rim	Core	Rim	Core	Rim	Core	Rim
SiO2	64.24	63.87	63.81	64.41	63.62	63.88	63.73	64.80	64.37	66.85	64.18	63.79	63.75	64.26	63.99	64.44	64.74	65.50	63.68	63.96
TiO2	0.00	0.31	0.10	0.00	0.00	0.00	0.00	0.00	0.00	0.00	0.00	0.53	0.00	0.00	0.00	0.43	0.22	0.00	0.03	0.00
Al2O3	17.48	17.31	17.23	17.45	17.49	17.20	17.37	17.51	17.46	15.75	17.08	16.92	16.97	17.29	16.67	16.62	16.83	17.30	17.07	16.78
Cr2O3	0.00	0.00	0.03	0.04	0.00	0.06	0.00	0.00	0.00	0.00	0.44	0.00	0.37	0.00	0.00	0.08	0.24	0.00	0.00	0.00
FeO$_{Tot}$	0.03	0.23	0.00	0.11	0.10	0.03	0.02	0.05	0.01	0.03	0.00	0.02	0.12	0.07	0.03	0.03	0.02	0.03	0.02	0.02
MnO	0.02	0.00	0.00	0.07	0.08	0.05	0.00	0.04	0.00	0.00	0.00	0.05	0.00	0.00	0.00	0.00	0.07	0.03	0.00	0.03
MgO	0.00	0.03	0.00	0.00	0.01	0.01	0.00	0.00	0.02	0.01	0.01	0.00	0.01	0.00	0.00	0.00	0.00	0.02	0.03	0.02
CaO	0.04	0.09	0.01	0.05	0.05	0.07	0.02	0.04	0.01	0.00	0.04	0.04	0.09	0.08	0.02	0.01	0.07	0.18	0.03	0.01
Na2O	0.48	0.80	0.17	0.65	1.00	0.75	1.40	2.84	3.17	0.32	0.75	0.50	1.17	2.25	0.31	0.18	1.78	3.56	0.48	0.45
K2O	16.19	16.04	16.53	16.07	14.41	15.77	15.20	13.63	11.62	15.31	15.57	16.00	14.86	12.97	16.61	16.85	13.71	10.62	16.45	16.04
Total	98.59	98.73	97.88	98.91	96.81	97.90	97.75	99.27	96.34	98.36	98.08	97.85	97.36	97.01	97.64	98.65	97.68	97.24	97.79	97.37
Si	3.02	2.99	3.02	3.01	3.04	3.02	3.00	2.97	3.06	3.17	3.03	3.02	3.02	3.04	3.03	3.03	3.05	3.07	3.01	3.04
Ti	0.00	0.01	0.00	0.00	0.00	0.00	0.00	0.00	0.00	0.00	0.00	0.02	0.00	0.00	0.00	0.02	0.01	0.00	0.00	0.00
Al	0.97	0.95	0.96	0.96	0.98	0.96	0.96	0.95	0.98	0.88	0.95	0.94	0.95	0.96	0.93	0.92	0.94	0.96	0.95	0.94
Cr	0.00	0.00	0.00	0.00	0.00	0.00	0.00	0.00	0.00	0.00	0.02	0.00	0.01	0.00	0.00	0.00	0.01	0.00	0.00	0.00
Fe2	0.00	0.00	0.00	0.00	0.00	0.00	0.00	0.00	0.00	0.00	0.00	0.00	0.00	0.00	0.00	0.00	0.00	0.00	0.00	0.00
Mn	0.00	0.00	0.00	0.00	0.00	0.00	0.00	0.00	0.00	0.00	0.00	0.00	0.00	0.00	0.00	0.00	0.00	0.00	0.00	0.00
Mg	0.00	0.00	0.00	0.00	0.00	0.00	0.00	0.00	0.00	0.00	0.00	0.00	0.00	0.00	0.00	0.00	0.00	0.00	0.00	0.00
Ca	0.00	0.00	0.00	0.00	0.00	0.00	0.00	0.00	0.00	0.00	0.00	0.00	0.00	0.00	0.00	0.00	0.00	0.01	0.00	0.00
Na	0.04	0.07	0.02	0.06	0.09	0.07	0.13	0.28	0.26	0.03	0.07	0.05	0.11	0.21	0.03	0.02	0.16	0.32	0.04	0.04
K	0.97	0.96	1.00	0.96	0.88	0.95	0.91	0.80	0.70	0.92	0.94	0.97	0.90	0.78	1.00	1.01	0.82	0.64	0.99	0.97
An	0.19	0.42	0.06	0.25	0.25	0.37	0.11	0.20	0.04	0.02	0.21	0.20	0.45	0.39	0.12	0.05	0.36	0.91	0.15	0.06
Ab	4.27	7.01	1.57	5.73	9.50	6.72	12.29	26.05	27.05	3.03	6.81	4.48	10.61	20.80	2.75	1.56	16.43	33.45	4.27	4.04
Or	95.54	92.57	98.36	94.02	90.25	92.92	87.60	73.76	72.91	96.95	92.98	95.32	88.94	78.80	97.14	98.39	83.21	65.63	95.59	95.90

Anexo II
Análises geoquímicas de K-feldspato e plagioclásio no domínio Gravatá.

Matrix - Plagioclase	1 Core	1 Rim	2 Core	2 Rim	3 Core	3 Rim	4 Core	4 Rim	5 Core	5 Rim
SiO_2	65.25	65.64	64.56	64.48	66.69	65.46	66.42	66.37	65.90	66.24
TiO_2	0.11	0.00	0.10	0.00	0.00	0.02	0.28	0.15	0.00	0.05
Al_2O_3	19.69	18.89	18.63	19.58	18.63	19.06	19.12	18.94	19.13	18.90
Cr_2O_3	0.00	0.00	0.00	0.00	0.00	0.00	0.00	0.00	0.06	0.05
FeO_{Tot}	0.00	0.07	0.02	0.02	0.04	0.04	0.07	0.20	0.00	0.14
MnO	0.00	0.00	0.00	0.00	0.00	0.00	0.00	0.00	0.00	0.10
MgO	0.00	0.00	0.00	0.02	0.02	0.00	0.00	0.02	0.02	0.00
CaO	1.68	0.86	1.11	1.95	0.34	0.88	0.92	1.02	0.80	0.49
Na_2O	10.58	10.35	9.88	10.09	11.03	10.62	11.11	10.87	11.62	11.08
K_2O	0.25	0.88	1.45	0.64	0.39	0.69	0.19	0.70	0.27	0.91
Total	97.56	96.68	95.75	96.76	97.14	96.77	98.11	98.26	97.79	97.94
Si	2.93	2.98	2.97	2.93	3.01	2.97	2.97	2.96	2.94	2.96
Ti	0.00	0.00	0.00	0.00	0.00	0.00	0.01	0.00	0.00	0.00
Al	1.04	1.01	1.01	1.05	0.99	1.02	1.01	1.00	1.00	0.99
Cr	0.00	0.00	0.00	0.00	0.00	0.00	0.00	0.00	0.00	0.00
Fe2	0.00	0.00	0.00	0.00	0.00	0.00	0.00	0.00	0.00	0.00
Mn	0.00	0.00	0.00	0.00	0.00	0.00	0.00	0.00	0.00	0.00
Mg	0.00	0.00	0.00	0.00	0.00	0.00	0.00	0.00	0.00	0.00
Ca	0.08	0.04	0.05	0.09	0.02	0.04	0.04	0.05	0.04	0.02
Na	0.92	0.91	0.88	0.89	0.96	0.93	0.96	0.94	1.00	0.96
K	0.01	0.05	0.08	0.04	0.02	0.04	0.01	0.04	0.02	0.05
An	7.95	4.14	5.34	9.29	1.65	4.20	4.34	4.71	3.59	2.25
Ab	90.65	90.75	86.32	87.07	96.09	91.87	94.59	91.40	94.97	92.74
Or	1.38	5.10	8.33	3.62	2.25	3.91	1.05	3.88	1.43	4.99

Matrix - K-feldspar	1 Core	1 Rim	2 Core	2 Rim	3 Core	3 Rim	4 Core	4 Rim	5 Core	5 Rim	6 Core	6 Rim	7 Core	7 Rim	8 Core	8 Rim	9 Core	9 Rim	10 Core	10 Rim	11 Core	11 Rim
SiO_2	64.12	62.94	63.00	62.85	63.48	62.76	62.60	63.27	62.63	62.89	62.66	62.57	61.03	61.85	62.33	62.41	61.92	61.75	62.59	62.88	62.85	62.58
TiO_2	0.01	0.04	0.00	0.00	0.10	0.24	0.08	0.00	0.00	0.00	0.18	0.10	0.11	0.00	0.00	0.00	0.04	0.17	0.00	0.00	0.05	0.00
Al_2O_3	18.13	17.26	17.67	17.17	17.69	17.52	17.48	17.60	17.46	17.69	17.36	17.29	17.25	17.29	17.21	17.08	17.28	17.50	17.28	17.19	17.42	17.29
Cr_2O_3	0.00	0.04	0.00	0.00	0.00	0.00	0.01	0.00	0.00	0.00	0.00	0.00	0.00	0.00	0.01	0.00	0.04	0.05	0.01	0.02	0.00	0.00
FeO_{Tot}	0.00	0.00	0.01	0.01	0.00	0.03	0.03	0.00	0.01	0.00	0.05	0.06	0.00	0.01	0.17	0.00	0.03	0.00	0.05	0.03	0.04	0.02
MnO	0.00	0.06	0.03	0.08	0.00	0.11	0.00	0.12	0.01	0.00	0.03	0.00	0.00	0.00	0.03	0.06	0.00	0.08	0.00	0.00	0.00	0.00
MgO	0.01	0.01	0.00	0.00	0.00	0.00	0.02	0.03	0.02	0.01	0.00	0.01	0.01	0.00	0.00	0.00	0.00	0.00	0.00	0.00	0.00	0.00
CaO	0.00	0.09	0.02	0.04	0.05	0.00	0.01	0.03	0.00	0.01	0.00	0.02	0.01	0.00	0.00	0.01	0.01	0.00	0.02	0.07	0.06	0.01
Na_2O	0.38	0.95	0.55	0.47	0.73	0.23	0.40	0.22	0.32	0.24	0.29	0.42	0.37	0.31	0.25	0.21	0.29	0.39	0.20	0.98	0.85	0.33
K_2O	15.96	15.94	15.93	15.28	15.02	16.06	16.01	16.37	16.03	16.37	16.30	15.72	15.66	16.11	16.31	16.40	15.84	15.80	16.01	15.24	15.21	16.15
Total	98.61	97.32	97.21	95.89	97.08	96.95	96.65	97.63	96.47	97.21	96.87	96.19	94.42	95.58	96.31	96.18	95.44	95.75	96.16	96.41	96.48	96.39
Si	3.01	2.98	2.99	3.03	3.02	3.00	62.60	3.00	3.00	2.99	2.99	3.01	2.99	2.99	2.99	3.00	3.00	2.98	3.01	3.01	3.01	3.00
Ti	0.00	0.00	0.00	0.00	0.00	0.01	0.08	0.00	0.00	0.00	0.01	0.00	0.00	0.00	0.00	0.00	0.00	0.01	0.00	0.00	0.00	0.00
Al	1.00	0.96	0.99	0.98	0.99	0.99	17.48	0.98	0.99	0.99	0.98	0.98	0.99	0.99	0.97	0.97	0.99	1.00	0.98	0.97	0.98	0.98
Cr	0.00	0.00	0.00	0.00	0.00	0.00	0.01	0.00	0.00	0.00	0.00	0.00	0.00	0.00	0.00	0.00	0.00	0.00	0.00	0.00	0.00	0.00
Fe2	0.00	0.00	0.00	0.00	0.00	0.00	0.03	0.00	0.00	0.00	0.00	0.00	0.00	0.00	0.00	0.00	0.00	0.00	0.00	0.00	0.00	0.00
Mn	0.00	0.00	0.00	0.00	0.00	0.00	0.00	0.00	0.00	0.00	0.00	0.00	0.00	0.00	0.00	0.00	0.00	0.00	0.00	0.00	0.00	0.00
Mg	0.00	0.00	0.00	0.00	0.00	0.00	0.02	0.00	0.00	0.00	0.00	0.00	0.00	0.00	0.00	0.00	0.00	0.00	0.00	0.00	0.00	0.00
Ca	0.00	0.00	0.00	0.00	0.00	0.00	0.01	0.00	0.00	0.00	0.00	0.00	0.00	0.00	0.00	0.00	0.00	0.00	0.00	0.00	0.00	0.00
Na	0.03	0.09	0.05	0.04	0.07	0.02	0.40	0.02	0.03	0.02	0.03	0.04	0.03	0.03	0.02	0.02	0.03	0.04	0.02	0.09	0.08	0.03
K	0.96	0.96	0.97	0.94	0.91	0.98	16.01	0.99	0.98	0.99	0.99	0.96	0.98	0.99	1.00	1.01	0.98	0.97	0.98	0.93	0.93	0.99
An	0.00	0.41	0.10	0.22	0.26	0.01	0.06	0.13	0.00	0.03	0.00	0.10	0.03	0.00	0.01	0.05	0.07	0.00	0.10	0.36	0.30	0.05
Ab	3.47	8.26	5.00	4.42	6.87	2.12	3.63	1.99	2.96	2.15	2.60	3.88	3.42	2.83	2.24	1.93	2.66	3.65	1.88	8.82	7.80	2.99
Or	96.52	91.31	94.89	95.34	92.85	97.86	96.29	97.87	97.03	97.81	97.39	96.00	96.53	97.16	97.74	98.01	97.25	96.34	98.00	90.81	91.89	96.95

Clast - Plagioclase

	1	2	3	4	5	6	7	8	9	10	11	12	13	14	15	16	17	18	19	20	21	22	23	24
SiO_2	63.78	64.05	64.30	64.48	64.83	64.27	58.08	64.68	65.14	64.16	64.50	63.66	63.03	68.92	64.64	64.58	67.02	68.67	66.94	66.50	66.50	65.94	64.58	65.55
TiO_2	0.12	0.00	0.01	0.04	0.12	0.10	0.00	0.00	0.06	0.00	0.05	0.00	0.49	0.01	0.00	0.00	0.00	0.00	0.00	0.01	0.00	0.05	0.25	0.00
Al_2O_3	20.41	21.13	20.98	21.14	20.99	21.31	19.24	20.84	21.31	21.32	21.72	21.64	17.86	19.48	21.35	20.88	18.29	18.07	16.53	20.34	18.04	17.39	18.09	21.20
Cr_2O_3	0.01	0.00	0.01	0.05	0.09	0.00	0.06	0.00	0.00	0.00	0.00	0.00	0.00	0.00	0.04	0.01	0.01	0.04	0.01	0.00	0.19	0.05	0.00	0.00
FeO_{Tot}	0.12	0.11	0.08	0.03	0.00	0.08	0.10	0.08	0.07	0.08	0.03	0.01	0.01	0.01	0.06	0.08	0.04	0.01	0.01	0.00	0.00	0.00	0.02	0.07
MnO	0.00	0.00	0.00	0.04	0.04	0.00	0.00	0.00	0.00	0.00	0.00	0.03	0.01	0.00	0.00	0.03	0.00	0.01	0.01	0.00	0.00	0.01	0.00	0.00
MgO	0.01	0.00	0.02	0.01	0.00	0.02	0.00	0.03	0.00	0.00	0.00	0.04	0.01	0.01	0.00	0.00	0.00	0.01	0.01	0.01	0.01	0.00	0.02	0.02
CaO	3.75	3.74	3.60	3.87	3.49	3.80	7.08	3.43	3.38	3.86	4.33	4.23	0.84	1.17	3.53	3.59	2.21	0.35	0.03	2.46	0.43	0.06	0.49	4.23
Na_2O	9.04	8.81	9.14	9.16	9.13	8.90	8.22	9.10	9.31	8.95	8.72	8.88	4.04	10.31	9.30	9.00	10.14	10.29	0.54	9.65	4.10	0.56	3.46	9.27
K_2O	0.07	0.07	0.11	0.08	0.14	0.06	0.14	0.27	0.08	0.10	0.16	0.16	11.69	0.08	0.09	0.09	0.50	0.37	15.92	0.12	10.37	16.14	11.22	0.11
Total	97.32	97.91	98.25	98.90	98.82	98.53	92.95	98.27	99.36	98.47	99.51	98.61	97.97	99.98	99.00	98.28	97.77	97.94	99.98	99.08	99.63	100.22	98.15	100.45
Si	2.91	2.91	2.90	2.89	2.92	2.90	2.78	2.92	2.91	2.89	2.89	2.87	3.38	3.05	2.89	2.92	3.03	3.11	3.82	2.97	3.45	3.76	3.46	2.90
Ti	0.00	0.00	0.00	0.00	0.00	0.00	0.00	0.00	0.00	0.00	0.00	0.00	0.02	0.00	0.00	0.00	0.00	0.00	0.00	0.00	0.00	0.00	0.01	0.00
Al	1.10	1.13	1.12	1.12	1.11	1.13	1.09	1.11	1.12	1.13	1.15	1.15	1.13	1.01	1.13	1.11	0.97	0.97	1.11	1.07	1.10	1.17	1.14	1.10
Cr	0.00	0.00	0.00	0.00	0.00	0.00	0.00	0.00	0.00	0.00	0.00	0.00	0.00	0.00	0.00	0.00	0.00	0.00	0.00	0.00	0.00	0.00	0.00	0.00
Fe2	0.00	0.00	0.00	0.00	0.00	0.00	0.00	0.00	0.00	0.00	0.00	0.00	0.00	0.00	0.00	0.00	0.00	0.00	0.00	0.00	0.00	0.00	0.00	0.00
Mn	0.00	0.00	0.00	0.00	0.00	0.00	0.00	0.00	0.00	0.00	0.00	0.00	0.00	0.00	0.00	0.00	0.00	0.00	0.00	0.00	0.00	0.00	0.00	0.00
Mg	0.00	0.00	0.00	0.00	0.00	0.00	0.00	0.00	0.00	0.00	0.00	0.00	0.00	0.00	0.00	0.00	0.00	0.00	0.00	0.00	0.00	0.00	0.00	0.00
Ca	0.18	0.18	0.17	0.19	0.17	0.18	0.36	0.17	0.16	0.19	0.21	0.20	0.05	0.06	0.17	0.17	0.11	0.02	0.00	0.12	0.02	0.00	0.03	0.20
Na	0.80	0.78	0.80	0.80	0.80	0.78	0.76	0.80	0.81	0.78	0.76	0.78	0.42	0.88	0.81	0.79	0.89	0.90	0.06	0.84	0.41	0.06	0.36	0.79
K	0.00	0.00	0.01	0.00	0.00	0.00	0.01	0.02	0.00	0.00	0.01	0.01	0.78	0.00	0.00	0.00	0.02	0.02	0.90	0.01	0.79	0.79	0.00	0.00
An	18.65	19.00	17.85	18.91	17.43	19.07	32.23	17.22	16.71	19.25	21.54	20.84	10.26	5.88	17.36	0.00	10.76	1.86	2.85	12.32	5.41	5.54	7.21	20.14
Ab	81.32	80.97	82.12	81.08	82.57	80.93	67.69	82.71	83.29	80.74	78.46	79.16	89.71	94.09	82.64	96.99	89.24	98.14	96.57	87.65	94.59	93.25	92.63	79.83
Or	0.03	0.04	0.02	0.01	0.00	0.00	0.08	0.07	0.00	0.01	0.00	0.00	0.03	0.03	0.00	3.01	0.00	0.00	0.59	0.02	0.00	1.21	0.16	0.03

Clast - K-feldspar

	1	2	3	4	5	6	7	8	9	10	11	12	13	14	15	16	17	18	19	20	21	22	23	24	25	26	27	28	29	30	31	32	33	34	35
SiO_2	64.89	64.87	64.83	64.60	64.29	64.98	64.47	65.34	63.65	63.63	64.53	63.94	64.10	64.03	64.28	64.47	63.91	63.38	63.67	64.28	63.59	64.43	63.80	63.66	63.88	63.68	63.47	61.27	64.73	64.28	64.25	63.87	60.93	65.60	56.68
TiO_2	0.00	0.00	0.10	0.01	0.00	0.00	0.00	0.04	0.00	0.00	0.01	0.12	0.00	0.00	0.21	0.00	0.08	0.06	0.00	0.00	0.22	0.00	0.00	0.00	0.12	0.07	0.00	0.00	0.12	0.00	0.00	0.04	0.17	0.00	0.09
Al_2O_3	17.78	18.05	18.02	17.88	17.63	17.56	17.63	17.88	18.00	18.01	18.57	17.94	17.94	18.22	18.23	18.26	18.35	18.06	18.31	18.31	17.90	18.29	18.21	18.23	18.06	18.21	18.35	17.36	18.19	18.31	18.32	18.24	17.15	18.83	15.63
Cr_2O_3	0.00	0.01	0.00	0.00	0.00	0.00	0.06	0.06	0.04	0.00	0.00	0.00	0.03	0.00	0.00	0.00	0.00	0.02	0.00	0.01	0.00	0.00	0.00	0.00	0.04	0.04	0.00	0.03	0.11	0.01	0.00	0.08	0.00	0.02	0.00
FeO_{Tot}	0.04	0.00	0.05	0.09	0.05	0.01	0.05	0.04	0.04	0.00	0.19	0.03	0.02	0.05	0.00	0.02	0.04	0.08	0.04	0.00	0.05	0.04	0.12	0.07	0.02	0.07	0.02	0.03	0.03	0.01	0.00	0.01	0.00	0.00	0.07
MnO	0.01	0.00	0.00	0.06	0.11	0.00	0.09	0.01	0.11	0.00	0.00	0.04	0.00	0.07	0.05	0.00	0.08	0.00	0.05	0.01	0.01	0.04	0.00	0.03	0.04	0.00	0.02	0.03	0.00	0.00	0.02	0.01	0.00	0.00	0.07
MgO	0.00	0.01	0.01	0.00	0.01	0.00	0.03	0.02	0.00	0.01	0.00	0.01	0.01	0.10	0.10	0.03	0.02	0.02	0.04	0.00	0.00	0.00	0.01	0.03	0.00	0.00	0.00	0.00	0.00	0.00	0.00	0.00	0.00	0.00	0.01
CaO	0.05	0.04	0.01	0.00	0.00	0.05	0.00	0.00	0.00	0.04	0.00	0.02	0.06	0.00	0.03	0.00	0.03	0.04	0.04	0.02	0.00	0.00	0.03	0.03	0.01	0.01	0.02	0.02	0.00	0.02	0.00	0.03	0.04	0.06	0.00
Na_2O	1.07	2.24	0.92	0.34	0.24	0.24	0.34	0.28	0.41	0.10	0.41	1.91	0.61	0.75	1.57	0.27	0.38	0.31	0.48	0.45	0.48	0.45	1.25	0.49	0.59	0.59	0.46	0.36	0.43	0.51	0.47	1.64	0.38	0.62	0.24
K_2O	14.93	12.74	15.35	16.01	16.19	16.67	16.27	15.12	16.04	14.46	9.74	14.08	15.35	15.46	14.19	16.13	16.37	16.31	15.88	15.95	15.67	14.71	15.44	15.93	15.68	15.68	15.92	15.76	15.86	15.81	16.13	14.23	14.81	15.79	15.27
Total	98.77	97.96	99.28	98.98	98.52	99.51	98.98	98.78	98.18	97.44	97.70	98.48	98.06	98.52	98.71	99.15	98.58	97.93	98.45	98.60	97.92	97.98	98.85	98.40	98.62	98.34	98.23	94.84	99.47	98.95	98.18	98.16	93.44	100.89	88.06
Si	3.03	3.04	3.01	3.02	3.02	3.02	3.01	3.07	3.00	3.01	2.99	2.98	3.02	3.00	3.00	3.00	3.00	2.99	2.99	3.01	3.00	3.05	2.97	2.99	3.00	2.99	2.98	2.99	3.01	3.00	2.99	2.99	3.02	3.00	2.98
Ti	0.00	0.00	0.00	0.00	0.00	0.00	0.00	0.00	0.00	0.00	0.00	0.00	0.00	0.00	0.01	0.00	0.00	0.00	0.00	0.00	0.01	0.00	0.00	0.00	0.00	0.00	0.00	0.00	0.00	0.00	0.00	0.00	0.01	0.00	0.00
Al	0.98	1.00	0.99	0.99	0.98	0.96	0.97	0.99	1.00	1.00	1.01	1.00	1.00	1.01	1.00	1.00	0.99	1.01	1.01	0.99	1.00	1.02	1.00	1.01	1.00	1.01	1.02	1.00	1.00	1.01	1.01	1.01	1.00	1.02	0.97
Cr	0.00	0.00	0.00	0.00	0.00	0.00	0.00	0.00	0.00	0.00	0.00	0.00	0.00	0.00	0.00	0.00	0.00	0.00	0.00	0.00	0.00	0.00	0.00	0.00	0.00	0.00	0.00	0.00	0.00	0.00	0.00	0.00	0.00	0.00	0.00
Fe2	0.00	0.00	0.00	0.00	0.00	0.00	0.00	0.00	0.00	0.00	0.01	0.00	0.00	0.00	0.00	0.00	0.00	0.00	0.00	0.00	0.00	0.00	0.00	0.00	0.00	0.00	0.00	0.00	0.00	0.00	0.00	0.00	0.00	0.00	0.00
Mn	0.00	0.00	0.00	0.00	0.00	0.00	0.00	0.00	0.00	0.00	0.00	0.00	0.00	0.00	0.00	0.00	0.00	0.00	0.00	0.00	0.00	0.00	0.00	0.00	0.00	0.00	0.00	0.00	0.00	0.00	0.00	0.00	0.00	0.00	0.00
Mg	0.00	0.00	0.00	0.00	0.00	0.00	0.00	0.00	0.00	0.00	0.00	0.00	0.00	0.01	0.01	0.00	0.00	0.00	0.00	0.00	0.00	0.00	0.00	0.00	0.00	0.00	0.00	0.00	0.00	0.00	0.00	0.00	0.00	0.00	0.00
Ca	0.00	0.00	0.00	0.00	0.00	0.00	0.00	0.00	0.00	0.00	0.01	0.00	0.00	0.00	0.00	0.00	0.00	0.00	0.00	0.00	0.00	0.00	0.00	0.00	0.05	0.05	0.04	0.03	0.04	0.05	0.04	0.15	0.04	0.06	0.02
Na	0.10	0.20	0.08	0.03	0.02	0.02	0.03	0.03	0.04	0.01	0.04	0.17	0.06	0.07	0.14	0.02	0.03	0.03	0.04	0.04	0.04	0.04	0.11	0.04	0.94	0.94	0.96	0.98	0.96	0.94	0.96	0.85	0.94	0.92	1.02
K	0.89	0.76	0.91	0.96	0.97	0.99	0.97	0.91	0.96	0.87	0.58	0.84	0.92	0.92	0.84	0.96	0.98	0.98	0.95	0.94	0.94	0.89	0.92	0.95	0.00	0.03	0.12	0.14	0.00	0.00	0.00	0.15	0.00	0.09	0.00
An	0.26	0.20	0.03	0.00	0.02	0.22	0.00	0.12	0.03	0.20	0.50	0.10	0.30	0.13	0.50	0.00	0.08	0.08	0.18	0.00	0.05	0.04	0.12	0.16	0.00	0.03	0.12	0.14	0.00	0.00	0.00	0.15	0.00	0.09	0.00
Ab	9.78	21.03	8.30	3.10	2.22	2.10	3.05	2.72	3.72	11.84	41.35	17.05	5.64	6.86	14.34	2.45	3.38	2.81	4.41	4.11	4.47	4.47	10.92	4.42	3.62	5.41	4.19	3.37	3.99	4.70	4.19	14.84	3.78	5.65	2.30
Or	89.95	78.76	91.64	96.89	97.75	97.67	96.74	97.15	96.24	87.95	58.13	82.83	94.30	92.83	85.14	97.41	96.61	97.09	95.39	95.88	95.52	95.47	88.95	95.41	96.37	94.55	95.68	96.47	96.00	95.21	95.79	85.00	96.21	94.24	97.69

75

Fracture - Plagioclase	1		2		3		4		5		6		7		8	
	Core	Rim	Core	Rim	Core	Rim	Core	Rim	Core	Rim	Core	Rim	Core	Rim	Core	Rim
SiO2	66.13	64.01	63.85	65.58	65.71	64.11	63.72	64.52	64.84	64.57	64.97	66.17	65.73	64.97	64.20	68.52
TiO2	0.00	0.00	0.06	0.00	0.09	0.00	0.00	0.00	0.03	0.04	0.02	0.03	0.05	0.00	0.23	0.16
Al2O3	19.64	20.03	20.17	19.35	20.89	20.15	20.22	20.48	20.63	20.26	19.96	19.73	19.67	19.94	20.47	18.81
Cr2O3	0.00	0.04	0.04	0.00	0.05	0.00	0.01	0.05	0.12	0.00	0.02	0.04	0.00	0.00	0.01	0.00
FeO$_{Tot}$	0.01	0.03	0.04	0.00	0.05	0.04	0.00	0.07	0.00	0.08	0.00	0.01	0.04	0.03	0.06	0.00
MnO	0.00	0.00	0.10	0.00	0.00	0.04	0.00	0.00	0.01	0.00	0.03	0.00	0.00	0.00	0.00	0.01
MgO	0.02	0.02	0.00	0.02	0.02	0.02	0.00	0.00	0.00	0.00	0.02	0.00	0.01	0.00	0.01	0.00
CaO	1.01	1.51	1.42	1.15	1.95	1.36	1.70	1.84	1.56	1.45	1.24	1.42	0.58	1.14	1.83	1.47
Na2O	10.30	11.03	10.67	10.30	11.29	11.04	9.92	10.07	10.62	10.65	11.08	10.13	11.11	10.25	10.53	8.83
K2O	0.14	0.08	0.36	1.37	0.12	0.10	1.00	0.56	0.06	0.06	0.09	0.13	0.10	0.91	0.09	0.76
Total	97.24	96.75	96.70	97.75	100.16	96.87	96.58	97.59	97.87	97.11	97.42	97.66	97.30	97.24	97.42	98.56
Si	2.99	2.89	2.89	2.94	2.87	2.89	2.90	2.91	2.90	2.91	2.91	2.99	2.99	2.93	2.89	3.10
Ti	0.00	0.00	0.00	0.00	0.00	0.00	0.00	0.00	0.00	0.00	0.00	0.00	0.00	0.00	0.01	0.01
Al	1.05	1.07	1.08	1.02	1.07	1.07	1.08	1.09	1.09	1.08	1.06	1.05	1.05	1.06	1.09	1.00
Cr	0.00	0.00	0.00	0.00	0.00	0.00	0.00	0.00	0.00	0.00	0.00	0.00	0.00	0.00	0.00	0.00
Fe2	0.00	0.00	0.00	0.00	0.00	0.00	0.00	0.00	0.00	0.00	0.00	0.00	0.00	0.00	0.00	0.00
Mn	0.00	0.00	0.00	0.00	0.00	0.00	0.00	0.00	0.00	0.00	0.00	0.00	0.00	0.00	0.00	0.00
Mg	0.00	0.00	0.00	0.00	0.00	0.00	0.00	0.00	0.00	0.00	0.00	0.00	0.00	0.00	0.00	0.00
Ca	0.05	0.07	0.07	0.06	0.09	0.07	0.08	0.09	0.07	0.07	0.06	0.07	0.07	0.06	0.09	0.07
Na	0.90	0.96	0.94	0.90	0.95	0.96	0.88	0.88	0.92	0.93	0.96	0.89	0.89	0.90	0.92	0.77
K	0.01	0.00	0.02	0.08	0.01	0.01	0.06	0.03	0.00	0.00	0.00	0.01	0.01	0.05	0.01	0.04
An	5.10	6.99	6.70	5.35	8.66	6.34	8.15	8.89	7.46	6.97	5.78	7.11	2.76	5.50	8.72	7.99
Ab	94.07	92.56	91.26	87.04	90.68	93.11	86.11	87.86	92.21	92.69	93.73	92.08	96.65	89.28	90.75	87.07
Or	0.81	0.44	2.02	7.59	0.65	0.54	5.73	3.23	0.32	0.33	0.48	0.80	0.57	5.20	0.51	4.93

Fracture - K-Feldspar	1		2		3		4		5		6		7		8		9		10	
	Core	Rim	Core	Rim	Core	Rim	Core	Rim	Core	Rim	Core	Rim	Core	Rim	Core	Rim	Core	Rim	Core	Rim
SiO2	61.21	66.92	59.73	62.48	62.94	61.95	62.28	63.33	63.45	62.64	63.14	61.85	62.86	62.54	62.57	62.07	62.54	62.72	63.64	63.30
TiO2	0.00	0.09	0.04	0.16	0.00	0.23	0.30	0.00	0.00	0.00	0.00	0.21	0.07	0.00	0.02	0.09	0.06	0.05	0.04	0.00
Al2O3	17.87	16.34	18.01	18.06	17.97	17.94	18.06	18.42	18.59	17.99	18.30	18.14	17.93	17.96	17.88	17.76	18.26	17.77	18.35	18.28
Cr2O3	0.00	0.03	0.04	0.01	0.00	0.00	0.00	0.00	0.00	0.01	0.00	0.00	0.08	0.00	0.00	0.00	0.07	0.04	0.00	0.00
FeO$_{Tot}$	0.01	0.00	0.00	0.06	0.03	0.04	0.02	0.10	0.06	0.07	0.00	0.03	0.01	0.00	0.02	0.06	0.00	0.01	0.03	0.04
MnO	0.00	0.00	0.00	0.15	0.00	0.06	0.06	0.00	0.01	0.05	0.00	0.00	0.00	0.00	0.00	0.02	0.06	0.00	0.13	0.00
MgO	0.00	0.01	0.00	0.02	0.00	0.01	0.00	0.02	0.02	0.00	0.00	0.00	0.00	0.00	0.00	0.00	0.01	0.00	0.00	0.00
CaO	0.09	0.25	0.03	0.26	0.05	0.02	0.01	0.07	0.31	0.19	0.12	0.09	0.00	0.00	0.11	0.00	0.06	0.00	0.04	0.14
Na2O	1.00	2.87	0.45	2.10	0.80	0.61	0.55	1.56	3.54	1.49	2.68	2.13	0.34	0.54	1.46	0.33	1.03	0.36	1.65	1.29
K2O	15.03	10.22	15.73	12.97	15.50	15.71	15.95	14.12	10.98	14.11	14.81	13.62	16.35	15.73	14.40	15.90	13.64	16.13	14.70	14.50
Total	95.21	96.73	94.03	96.26	97.28	96.57	97.24	97.62	96.97	96.53	99.05	96.06	97.64	96.78	96.46	96.22	95.72	97.08	98.58	97.55
Si	2.96	3.18	2.93	2.98	2.98	2.96	2.96	2.98	2.97	2.98	2.90	2.94	2.98	2.98	2.98	2.98	3.02	2.99	2.96	2.99
Ti	0.00	0.00	0.00	0.01	0.00	0.01	0.01	0.00	0.00	0.00	0.00	0.01	0.00	0.00	0.00	0.00	0.00	0.00	0.00	0.00
Al	1.02	0.92	1.04	1.01	1.00	1.01	1.01	1.02	1.03	1.01	0.99	1.02	1.00	1.01	1.00	1.01	1.04	1.00	1.01	1.02
Cr	0.00	0.00	0.00	0.00	0.00	0.00	0.00	0.00	0.00	0.00	0.00	0.00	0.00	0.00	0.00	0.00	0.00	0.00	0.00	0.00
Fe2	0.00	0.00	0.00	0.00	0.00	0.00	0.00	0.00	0.00	0.00	0.00	0.00	0.00	0.00	0.00	0.00	0.00	0.00	0.00	0.00
Mn	0.00	0.00	0.00	0.01	0.00	0.00	0.00	0.00	0.00	0.00	0.00	0.00	0.00	0.00	0.00	0.00	0.00	0.00	0.01	0.00
Mg	0.00	0.00	0.00	0.00	0.00	0.00	0.00	0.00	0.00	0.00	0.00	0.00	0.00	0.00	0.00	0.00	0.00	0.00	0.00	0.00
Ca	0.00	0.01	0.00	0.01	0.00	0.00	0.00	0.00	0.02	0.01	0.01	0.00	0.00	0.00	0.01	0.00	0.00	0.00	0.00	0.01
Na	0.09	0.26	0.04	0.19	0.07	0.06	0.05	0.14	0.32	0.14	0.24	0.20	0.03	0.05	0.13	0.03	0.10	0.03	0.15	0.12
K	0.93	0.62	0.98	0.79	0.94	0.96	0.97	0.85	0.66	0.86	0.87	0.83	0.99	0.96	0.87	0.97	0.84	0.98	0.87	0.87
An	0.43	1.41	0.15	1.33	0.23	0.11	0.06	0.37	1.57	0.94	0.54	0.46	0.00	0.00	0.56	0.00	0.30	0.00	0.20	0.70
Ab	9.10	29.47	4.14	19.45	7.24	5.53	5.00	14.33	32.37	13.65	21.43	19.11	3.09	4.99	13.24	3.03	10.23	3.27	14.55	11.78
Or	90.45	69.10	95.69	79.20	92.52	94.35	94.93	85.29	66.05	85.39	78.01	80.41	96.90	95.00	86.18	96.96	89.45	96.72	85.24	87.51

Anexo III
Geoposicionamento dos afloramentos.

Afloramento	Coordenada E-W	Coordenada N-S	Rocha
PE01	-35.948847	-8.344253	Granito milonítico médio a fino
PE02	-35.948847	-8.344252	Granito milonítico fino
PE03	-35.948847	-8.344252	Granito milonítico bandado
PE04	-35.948847	-8.344253	Granito milonítico fino
PE05	-35.948847	-8.344253	Granito milonítico
PE06	-36.051929	-8.316220	Granito milonítico médio a grosso
PE07	-35.948847	-8.344253	Granito milonítico fino
PE08	-35.948847	-8.344253	Granito milonítico fino
PE09	-35.948847	-8.344253	Granito milonítico fino
PE10	-35.948847	-8.344253	Granito milonítico fino a médio
PE11	-35.948847	-8.344253	Granito milonítico fino
PE12	-35.948847	-8.344253	Granito milonítico fino
PE13	-35.948847	-8.344253	Granito milonítico fino
PE14	-35.948847	-8.344253	Granito milonítico bandado
PE15	-35.948847	-8.344253	Ultramilonítico félsicos e máficos
PE16	-35.948847	-8.344253	Ultramilonito bandado
PE17	-36.759590	-8.441584	Granito milonítico fino
PE18	-36.759590	-8.441584	Granito milonítico fino
PE19	-36.759590	-8.441584	Granito milonítico médio
PE20	-36.759590	-8.441584	Granito milonítico
PE21	-36.759590	-8.441584	Granito milonítico fino
PE22	-36.759590	-8.441584	Granito milonítico grosso
PE23	-36.759590	-8.441584	Granito milonítico grosso
PE24	-36.759590	-8.441584	Granito milonítico médio a grosso
PE25	-36.759590	-8.441584	Granito milonítico
PE26	-36.759590	-8.441584	Granito milonítico grosso
PE27	-36.759590	-8.441584	Granito milonítico fino
PE28	-36.759590	-8.441584	Granito milonítico fino
PE29	-36.759590	-8.441584	Granito milonítico fino
PE30	-36.753790	-8.421478	Ortognaisse milonitizado
PE31	-36.159148	-8.327987	Granito milonítico fino
PE32	-35.755178	-8.331338	Granito grosso
PE33	-35.755306	-8.233619	Granito milonítico
PE34	-35.785038	-8.237839	Granito milonítico grosso
PE35	-35.772034	-8.237088	Granito milonítico a ultramilonítico
PE36	-35.461315	-8.193400	Granito milonítico
PE37	-35.460506	-8.192216	Granito milonítico
PE37B	-35.457611	-8.189651	Granito milonítico
PE38	-35.439491	-8.178735	Granito milonítico bandado
PE39	-35.439766	-8.188560	Granito milonítico
PE40	-35.429340	-8.182794	Granito milonítico
PE41	-35.413429	-8.147888	Xisto milonítico
PE42	-35.423832	-8.153564	Ultramilonito bandado
PE43	-35.422691	-8.155436	Ultramilonito bandado
PE44	-35.457569	-8.159386	Granito milonítico grosso
PE45	-37.015526	-8.410551	Granito milonítico grosso
PE46	-35.751255	-8.272941	Granito milonítico grosso
PE47	-35.789185	-8.259341	Migmatito estromático milonitizado
PE48	-35.848366	-8.298358	Gnaisse milonitizado
PE49	-36.627628	-8.351962	Granito milonítico
PE49B	-36.630360	-8.348154	Granito milonítico
PE50	-36.382786	-8.283185	Granito milonítico grosso
PE51	-36.374207	-8.293204	Granito milonítico grosso
PE52	-36.363991	-8.284976	Granito milonítico médio a grosso
PE53	-36.317791	-8.285752	Granito milonítico médio a grosso
PE54	-36.317799	-8.314506	Granito milonítico
PE55	-35.772884	-8.235218	Ortognaisse milonitizado
PE56	-36.953421	-8.411580	Granito milonítico
PE57	-36.952694	-8.413650	Granito protomilonítico
PE58	-36.086735	-8.306108	Granito milonítico
PE59	-36.907623	-8.402469	Granito milonítico
PE60	-35.052193	-8.097137	Granito milonítico alterado
PE61	-35.100025	-8.096116	Granito milonítico grosso
PE62	-35.156548	-8.107586	Granito milonítico grosso
PE63	-35.195419	-8.104652	Granito milonítico fino
PE64	-35.283031	-8.113069	Granito milonítico
PE65	-35.374634	-8.138507	Migmatito estromático milonitizado
PE66	-35.348763	-8.147838	Xisto milonítico
PE67	-35.363354	-8.155212	Granito ultramilonítico
PE68	-35.354176	-8.162438	Granito milonítico grosso
PE69	-35.328228	-8.158428	Granito milonítico grosso
PE70	-35.281845	-8.132297	Granito milonítico a ultramilonítico
PE71	-36.798649	-8.408580	Granito milonítico fino a grosso
PE72	-34.974304	-8.041071	Granito milonítico

Anexo IV

Composição modal das amostras utilizadas no modelamento termodinâmico

PE-43	Textura	Pontos	%	% Total
Quartzo	Porfiroclasto	17	2	**28**
	Recristalizado	235	26	
K-feldspato	Porfiroclasto	82	9	**25**
	Recristalizado/Fragmento	137	15	
Plagioclasio	Porfiroclasto	58	7	**22**
	Recristalizado/Fragmento	136	15	
Biotita	Recristalizado	113	13	**13**
Granada	Porfiroclasto	16	2	**2**
Titanita	recristalizado	16	2	**2**
Magnetita	Recristalizado	16	2	**2**
Epidoto	Recristalizado	62	7	**7**
Total		888	100	**100**

PE-49B	Textura	Pontos	%	% Total	Modelado
Quartzo	Porfiroclasto	5	0.38	**19.8**	**18.7**
	Recristalizado	255	19.44		
K-feldspato	Porfiroclasto	346	26.37	**36.1**	**41.1**
	Recristalizado/Fragmento	127	9.68		
Plagioclasio	Porfiroclasto	154	11.74	**21.3**	**22.2**
	Recristalizado/Fragmento	126	9.60		
Biotita	Recristalizado	249	18.98	**19.0**	**11.0**
Titanita	Porfiroclasto	6	0.46	**0.5**	**0.04**
Epidoto	Recristalizado	7	0.53	**0.5**	**0.3**
Anfibólio	Primário	5	0.38	**0.4**	
Apatita	Primário	30	2.29	**2.3**	
Ilmenita	Porfiroclasto	2	0.15	**0.2**	**2.0**
Total		1312	100.00	**100.00**	**95.3**

Anexo V

Pseudoseções T-X(O_2) – domínio Caruaru

Sample PE-49 P= 4.75 kbar, H_2O = 1 wt%

Melt-in

Melt,Qz,Bt
Pl,Kfs,Hem,Ilm

Melt,Qz,Bt,Pl
Kfs,Spl,Ilm

Qz,Bt,Pl,Kfs
Spl,Ilm,H_2O

Melt,Qz,Bt
Pl,Kfs,Ilm

Spl-in

Qz,Bt,Pl,Kfs
Ttn,H_2O

Qz,Bt,Pl,Kfs
Ilm,H_2O

Qz,Bt,Pl,Kfs
Ilm,Hem,Ttn,H_2O

Qz,Bt,Pl,Kfs
Ttn,H_2O

Qz,Ep,Bt,Pl
Kfs,Ilm,H_2O

Qz,Ms,Bt,Pl
Kfs,Ilm,H_2O

Qz,Bt,Pl,Kfs
Ilm,Ttn,Ru,H_2O

Qz,Bt,Pl,Kfs,Ilm
Hem,Ttn,Ru,H_2O

Ms-out

Qz,Ms,Bt,Pl,Kfs
Ilm,Ttn,H_2O

Qz,Ep,Bt,Pl,Kfs
Ilm,Ttn,H_2O

Qz,Ms,Bt,Pl,Kfs
Ilm,Ttn,Ru,H_2O

Qz,Ep,Bt,Pl
Kfs,Ilm,H_2O

Qz,Ep,Ms,Bt,Pl
Kfs,Ilm,Ttn,H_2O

Qz,Ep,Ms,Bt,Pl
Kfs,Ttn,H_2O

Amp-out

Qz,Amp,Ep,Ms,Bt
Pl,Kfs,Ttn,H_2O

Qz,Amp,Ep,Ms
Pl,Kfs,Ttn,H_2O

Qz,Amp,Ep,Ms,Pl
Kfs,Ttn,Ilm,H_2O

T (°C)

X(O_2)

Pseudoseções T-X(O_2) – domínio Gravatá

Sample PE-43 P= 5.5 kbar, H_2O = 0.5 wt%

Melt,Qz,Gt,Bt
Pl,Kfs,Ttn,Fact

Melt,Qz,Gt,Bt,Pl
Kfs,Spl,Ttn

Melt,Qz,Gt,Bt
Pl,Kfs,Spl,Ilm

Melt,Qz,Gt,Bt
Pl,Kfs,Ilm

Melt,Qz,Gt,Bt,Pl
Kfs,Ilm,Ttn,O_2

Melt,Qz,Gt,Bt
Pl,Kfs,Ttn

Melt-in

Qz,Gt,Bt,Pl,Kfs
Ttn,Wo,H_2O

Melt,Qz,Gt,Bt,Pl
Kfs,Spl,Ilm,Ttn

Melt,Qz,Gt,Bt,Pl
Kfs,Ilm,Ttn

Qz,Gt,Bt,Pl,Kfs
Ilm,H_2O

Qz,Gt,Bt,Pl,Kfs
Spl,Ttn,H_2O

Qz,Gt,Bt,Pl
Kfs,Ttn,H_2O

Qz,Gt,Bt,Pl,Kfs
Spl,Ilm,Ttn,H_2O

O_2 saturation line

Qz,Gt,Bt,Pl,Kfs,Ilm
Ttn,H_2O,O_2

Qz,Gt,Bt,Pl,Kfs
Ilm,Ttn,H_2O

Ep-in

Qz,Gt,Ep,Bt,Pl
Kfs,Ilm,Ttn,H_2O

Qz,Ep,Bt,Pl,Kfs
Ilm,Ttn,H_2O,O_2

Qz,Amp,Ep,Bt,Pl
Kfs,Ttn,Ilm,H_2O

Amp-in

Qz,Ep,Bt,Gt,Pl
Kfs,Amp,Ttn,H_2O

Qz,Amp,Ep,Bt,Pl
Kfs,Ttn,Ilm,H_2O

Qz,Ep,Bt,Pl,Kfs
Amp,Ilm,Ttn,H_2O

Qz,Ep,Pl,Kfs,Amp
Ilm,Ttn,H_2O

Qz,Ep,Bt,Pl,Kfs,Amp
Ilm,Ttn,H_2O,O_2

Qz,Ep,Amp,Ms,Bt,Pl
Kfs,Ttn,H_2O

Qz,Ep,Ms,Pl,Kfs,Amp
Ilm,Ttn,H_2O

Qz,Ep,Ms,Pl,Amp
Kfs,Ttn,H_2O

T (°C)

X(O_2)

79